Effect of interlaminar defects on the mechanical behaviour of carbon fibre reinforced silicon carbide

A thesis accepted by the Faculty of Aerospace Engineering and Geodesy of the Universität Stuttgart in partial fulfilment of the requirements for the degree of Doctor of Engineering Sciences (Dr.-Ing.)

by
Severin Hofmann
born in Straubing

main referee:	Prof. Dr.-Ing. Heinz Voggenreiter
co-referee:	Prof. Dr. rer. nat. Siegfried Schmauder
Date of defence:	28th of June 2013

Institute of Aircraft Design
University of Stuttgart
2013

Danksagung

Mein Dank geht an Herrn Prof. Heinz Voggenreiter für die Betreuung der Arbeit sowie an Herrn Prof. Siegfried Schmauder für die Übernahme des Mitberichts. Ich danke Herrn Prof. Voggenreiter und Herrn Prof. Schmauder für Ihre wissenschaftliche und persönliche Förderung während meiner Promotionszeit.

Weiter möchte ich mich bei allen Mitarbeitern des Instituts für Bauweisen- und Konstruktionsforschung des DLR in Stuttgart und besonders bei den Kollegen der Abteilung Keramische Verbundstrukturen für die Unterstützung der Arbeit bedanken. Insbesondere danke ich Herrn Bernhard Heidenreich und Herrn Dr. Dietmar Koch, die diese Arbeit ermöglicht haben.

Bei Dr. Dietmar Koch möchte ich mich darüber hinaus für den wissenschaftlichen Diskurs und für alle Kritik und Verbesserungsvorschläge bedanken.

Herrn Harald Kraft gilt mein Dank, da er mir bei allen Fragen der mechanischen Prüfung weitergeholfen hat.

Bei Berkan Öztürk, Paulin Tchewebey und Sven Weisenberger bedanke ich mich für den vollen Einsatz bei der Erstellung Ihrer Studien- und Diplomarbeiten. Ihr Engagement hat wesentlich zum Gelingen dieser Arbeit beigetragen.

Meinen Eltern, Irmengard und Franz Hofmann, will ich unbedingt für ihren andauernden Rückhalt danken.

Nur wer sich hohe Hürden setzt,
weiß wie hoch er springen kann.

Table of Content

Nomenclature

Abbreviations:

AITM	Airbus Industry Test Method
ASTM	American Society for Testing and Materials
C/C	Carbon fibre reinforced Carbon
C/C-SiC	Carbon fibre reinforced Silicon Carbide by LSI
CFRP	Carbon Fibre Reinforced Polymer
CMC	Ceramic-Matrix Composite
C/SiC	Carbon fibre reinforced Silicon Carbide
CT	Computer Tomography
CTS	Compact Tension Shear
CVI	Chemical Vapor Infiltration
CZE	Cohesive Zone Element
DCB	Double Cantilever Beam
DLR	German Aerospace Centre
ENF	End-Notched Flexure
FE	Finite Element
FhG	Fraunhofer-Gesellschaft e.V.
LEFM	Linear Elastic Fracture Mechanics
LSI	Liquid Silicon Infiltration
MBT	Modified Beam Theory
MTA	MT Aerospace AG
NDT	Non-Destructive Testing
OXIPOL	Oxide CMC based on Polymers
PIP	Polymer Infiltration and Pyrolysis
Pritzkow	Walter E.C. Pritzkow Spezialkeramik
RT	Room Temperature
RTM	Resin Transfer Molding
SBB	Short-Beam Bending

US	Ultrasonic
WHIPOX	Wound Highly Porous Oxide Ceramic
WIC	Weak Interface Composite
WMC	Weak Matrix Composite

Symbols:

Γ_i/Γ_f	Relative fracture energy of fibre and interface
G_{Ic}, G_{IIc}	Critical energy release rate in mode I and II
a	Crack length
K_{Ic}	Critical stress intensity factor
F	Load
L	Support distance
b	Sample width
τ	Shear stress
u_{total}	Total deflection
u_M	Deflection due to bending moment
u_s	Deflection due to shear deformation
E	Young's modulus
G	Shear modulus
σ_b	Theoretical bending stress
I	Geometrical moment of inertia
C	Compliance
S	Stiffness
Δ	Additional effective crack length
N	Loading block correction factor for DCB-test
L', t	Geometrical details for DCB-test
A	Integrated area
a_p	Propagated crack length
$\sigma_t^{max}, \sigma_c^{max}$	Ultimate tensile and compression strength
τ_{xy}^{max}	Shear strength
$\sigma_{45°}$	Tensile strength in 45°-orientation

σ_{eff}	Effective stress
σ_0	Reference stress
F, G, H, N	Hill factors
R_{xx}, R_{yy}...	Hill stress ratios
H_1, H_2...	Tsai-Wu parameters
σ_{+j}, σ_{-j}	Tensile and compressive yield strength
E_{Tj}	Tangent modulus
M_{jj}	Yield stress ratios for generalized Hill criterion
{L}	Strength differential vector
W_j^P	Total plastic work
E_{pj}	Plastic modulus
ε_j^P	Plastic strain
u_c	Separation at completion of debonding
K_n	Initial contact stiffness
d_n	Debonding parameter
σ_{max}	Maximum stress, inititation of debonding
u_s	Separation at maximum stress
u_{nc}	Displacement without crack opening
u_c	Displacement due to crack opening
S_{nc}	Stiffness without pre-crack
μ	Coefficient of friction

Kurzfassung

Faserverstärkte Keramiken zeichnen sich durch ihre Hochtemperaturbeständigkeit und hohe Schadenstoleranz aus. Im Gegensatz zu monolithischen Keramiken können aus CMC (Ceramic-Matrix Composite)-Werkstoffen großflächige Bauteile mit geringen Wandstärken konstruiert werden. Diese Eigenschaft macht faserverstärkte Keramiken zu einer einzigartigen Werkstoffgruppe für Hochtemperaturleichtbau-Anwendungen.

Der kohlefaserverstärkte SiC-Werkstoff, C/C-SiC, der am Institut für Bauweisen- und Konstruktionsforschung des Deutschen Zentrums für Luft- und Raumfahrt entwickelt wurde, findet derzeit Anwendung z.B. als Wiedereintritts-Hitzeschutz oder als Tragstruktur für Satellitenkommunikationsoptik in der Raumfahrt sowie als Bremsscheibe im Automobilbau. Im Bereich Luftfahrt zeigen die Keramiken mit SiC- und oxidischer Faserverstärkung ein hohes Potential für den Einsatz in der Fluggasturbine. Durch den Einsatz von CMC-Werkstoffen, z.B. als Brennkammerauskleidung, sollen die Verbrennungs-temperaturen erhöht bzw. der Kühlluftverbrauch verringert werden. Die erzielte Steigerung der Verbrennungseffizienz führt zu geringerem Treibstoffverbrauch und reduziertem CO_2- Ausstoß.

Ein wesentlicher Faktor, der derzeit die Verbreitung von CMCs in industriellen Anwendungen limitiert, ist die mangelnde Berechenbarkeit von CMC-Strukturen. Zum Einen fehlt es noch an zuverlässigen Versagensmodellen für die Auslegung von CMCs unter statischen und dynamischen Lasten. Zum Anderen fehlt es an Berechnungsmethoden, die bei der Auslegung von CMC-Bauteilen auch fertigungsbedingte Defekte berücksichtigen.

Aufgrund der Hochtemperatur-Prozessierung und der daraus resultierenden Interaktion von Fasern und Matrix ist die Reduzierung von Fertigungsfehlern wesentlich schwieriger als bei metallischen oder polymeren Werkstoffen. Die meisten Defekte können mit Hilfe moderner zerstörungsfreier Prüfverfahren, wie z.B. der Mikro-Computertomographie, aufgezeigt werden. Der Einfluss der Defekte auf die Bauteilfunktion ist aber meist nicht bekannt.

Um hohe Ausschussquoten und eine Überdimensionierung von CMC-Bauteilen zu verhindern, müssen deshalb bei komplexen CMC-Strukturbauteilen fertigungs-bedingte Fehlstellen bei der Auslegung und Berechnung berücksichtigt werden. Entscheidend ist dabei, zwischen bauteilkritischen und unkritischen Fehlern unterscheiden zu können.

Im Folgenden soll demonstriert werden, wie der CMC-Werkstoff, C/C-SiC, mit fertigungsbedingten interlaminaren Defekten berechnet werden kann. Der Fokus liegt hierbei auf Delaminationen, die prozessbedingt im untersuchten C/C-SiC-Werkstoff

auftreten können. Die Entstehung von Delaminationen während des Herstellungsprozesses nach dem Liquid Silicon Infiltration-Verfahren wird aufgezeigt und erläutert.

Um die auf finiten Elementen basierenden Berechnungsverfahren zu validieren, wird der 3-Punkt-Biegeversuch verwendet. Dieser Versuch wurde gewählt, da die Defektgröße und Lage sich deutlich auf Steifigkeit, Versagenslast und Versagensart, im Wesentlichen Zug oder Schubversagen, auswirkt. Aufgrund der relativ einfachen Randbedingungen können Einflüsse durch die Einspannung, im Gegensatz zum Zug- oder Druckversuch, vernachlässigt werden.

Zur Berechnung von C/C-SiC mit interlaminaren Defekten wird ein anwendungsorientierter, mit dem kommerziellen FE-Code ANSYS durchgeführter, Berechnungsansatz aufgezeigt. Das Standard-Material ohne Defekte wird als homogenisierter orthotroper Werkstoff berechnet. Mit Hilfe eines anisotropen Fließgesetzes und einem bilinearem Verfestigungsmodell wird das pseudo-plastische, nicht-lineare Verhalten in der Ebene der Gewebelagen abgebildet. Zunächst wird mit Hilfe des nicht-linearen Werkstoffmodells der Biegeversuch ohne Delaminationen berechnet. Das translaminare Zugversagen wird mit Kohäsiv-Zonen-Elementen beschrieben. Die für die Rissausbreitung notwendige Brucharbeit, Work of Fracture, wird mittels SENB-Versuchen bestimmt und in den Kohäsiv-Zonen-Modellen berücksichtigt.

Im nächsten Schritt wird das Verhalten von C/C-SiC mit künstlichen interlaminaren Defekten untersucht. Unter Mode I und II Last werden die interlaminaren Energiefreisetzungsraten anhand künstlicher Anrisse bestimmt. Die ermittelten G_{Ic}- und G_{IIc}-Werte werden für die FE-Modellierung der interlaminaren Rissausbreitung verwendet. Die interlaminare Rissausbreitung wird, wie die translaminare Rissausabreitung, durch Kohäsiv-Zonen-Modelle beschrieben. Die FE-Modelle werden im Abgleich mit den experimentellen Double Cantilever Beam, DCB- und End Notched Flexure, ENF-Versuchen validiert.

Weiter werden die Lage, Form und Größe fertigungsbedingter Delaminationen in FE-Modelle implementiert. Dabei werden zwei Ansätze aufgezeigt: Erstens werden 3D-Realstrukturmodelle direkt aus 3D-Computertomographie-Grauwertdatensätzen generiert und zum Zweiten werden anhand der CT-Daten vereinfachte 2D-Biegemodelle mit Defekten konstruiert. Aufgrund des wesentlich geringeren Vernetzungsaufwands wird der zweite Ansatz gewählt um mit der Hilfe von trans- und interlaminaren Kohäsiv-Zonen-Elementen die Rissausbreitung zu beschreiben. Die FE-Modelle werden schließlich mit den Biegeversuchen an den entsprechenden Proben verglichen. Mit den vereinfachten 2D-Biegemodellen wurden mit relativ geringen Elementanzahlen und kurzen Rechenzeiten gute Übereinstimmungen bezüglich Steifigkeit und Versagenslast erzielt. Somit sollte der gezeigte Berechnungsansatz für C/C-SiC-Bauteile mit Defekten relativ schnell übertragbar sein.

Abstract

Ceramic-Matrix Composites (CMCs) are highly interesting candidates for light-weight structures in high temperature applications. CMCs show high temperature resistance like monolithic ceramics. But in contrast to monolithic ceramics CMCs do also show a high damage tolerance which makes the design of large light-weight CMC structures possible.

The investigated CMC, carbon fibre reinforced silicon carbide, C/C-SiC, was developed at the German Aerospace Centre, DLR, by using the Liquid Silicon Infiltration (LSI) process. C/C-SiC is used e.g. for thermal protection systems on re-entry capsules or as break disk in car-industry.

A limiting factor for CMC components in industrial application still is the precise design for static and fatigue loads, especially if manufacturing defects appear.

Due to the high temperatures and complex interactions of fibres and matrix during processing, defects like pores and delaminations cannot be completely prevented during the manufacturing of advanced CMC structures. With the help of modern micro-Computer Tomography (CT) most of the macroscopic defects can be detected with high resolution and detection reliability.

The impact of defects on the functionality of CMC components is usually not predictable. Therefore, manufacturing defects are leading to high rejection rates, high component costs and an oversizing of CMC components. Critical and non-critical defects for the structural properties have to be distinguished by extensive and costly structural testing or by computational modelling.

A modelling approach based on Cohesive Zone Elements is presented for the computation of C/C-SiC with interlaminar defects in the following. The investigation of defects is focusing on delaminations which are the most common manufacturing defects in C/C-SiC structures. The FE-analyses are performed within the commercial code ANSYS.

The formation of delaminations during LSI-processing is presented.

The Finite Element approach is validated by comparing the numerical results with 3-point bending tests of partially delaminated C/C-SiC samples. The 3-point bending test was selected, since the test results have a high sensitivity to the defect size and location. Furthermore, the actual failure mode, mainly tensile or shear failure, depends strongly on defect size and location. In contrast to tensile and compression testing the bending test is insensitive to clamping effects, which is another advantage for the evaluation of the effect of defects.

The modelling approach is rather straight forward: the material without defects is modelled as a homogenized orthotropic continuum. An anisotropic yield criterion and

a bilinear hardening rule are used to model the directional non-linear behaviour of C/C-SiC. The behaviour at the delamination or crack front is modelled by Cohesive Zone Elements accounting for the translaminar and interlaminar energy release rates, which were determined by mechanical testing.

In the first step the bending test of standard material without defects was modelled by using the mentioned yield model and Cohesive Zone Elements for modelling the translaminar tensile failure. The respective critical energy release rate takes the Work of Fracture, as determined by Single Edge Notched Bending-test, into account.

In the next step, the mechanical behaviour of C/C-SiC with artificial interlaminar pre-cracks was investigated. The critical energy release rates were determined under mode I and II loading by Double Cantilever Beam- and End Notched Flexure-testing. The interlaminar failure was modelled also by Cohesive Zone Elements accounting for the respective energy release rates. The FE-models were validated by comparing the experimental and numerical load-deflection data with analytical solutions from Linear Elastic Fracture Mechanics, LEFM.

Finally, the behaviour of C/C-SiC with interlaminar manufacturing defects was modelled by using the translaminar failure models validated on standard material and the interlaminar failure models validated on artificial pre-cracks.

The detailed defect information, i.e. the geometry, size and location, was taken from micro-CT-images. Two approaches are presented. The first one is using grey scale data for the generation of 3D FE-meshes directly. The second one is using the defect information for the design of equivalent 2D-Cohesive Zone models. Because of the complex meshing routines for grey scale data, the cohesive zone failure models were applied for the reduced 2D-models only. The grey scale models were computed linear elastically without failure modelling.

Although, the defect geometries were strongly simplified for the 2D bending models a good agreement of experimental and numerical strength and stiffness of partially delaminated C/C-SiC samples was reached. Due to the simplified 2D-models low element numbers and a reduced computational effort was gained, in contrast to the real structure models from grey scale data. That makes the simplified cohesive zone approach applicable for the computation of C/C-SiC components with interlaminar manufacturing defects.

1. Introduction

Ceramic-Matrix Composites (CMCs) are high-potential materials for light-weight structures in high temperature applications. CMCs show high temperature resistance like monolithic ceramics. But in contrast to monolithic ceramics CMCs do also show a high damage tolerance which makes the design of large light-weight CMC-structures possible.

One limiting factor for CMCs in industrial application is the precise design of CMC components. Due to the complex, high temperature manufacturing of CMC components it is not always possible to prevent the formation of processing defects completely.

Therefore, manufacturing defects are leading to high rejection rates, costs and to an oversizing of CMC components. In this way the full light-weight potential is not tapped and new fields of application are lost.

With the help of modern non-destructive testing methods, like micro-Computer Tomography (CT), most of the macroscopic defects can be detected with high resolution and detection reliability.

Nevertheless, the impact of defects on stiffness and strength of CMC materials and structures is still not clear. Thus the effect of interlaminar defects is approached by integrating the defect information from micro-CT into Finite Element (FE) models. With the help of the adequate material and fracture mechanical models, it should be possible to predict the stiffness and strength of samples and structures with manufacturing defects. The ability to assess the impact of defects on the performance of CMC structures can help to minimize rejection rates and accelerate material and process optimization by focusing on design critical defects only.

2. Specification of investigated topic

The mechanical behaviour of C/C-SiC with and without interlaminar defects is investigated and modelled with FEM (Finite Element Method) at room temperature (RT).

First the behaviour of standard C/C-SiC without manufacturing defects is modelled by a macroscopic approach taking the non-linear behaviour and failure of the material into account. The necessary parameters and their determination by mechanical testing are described. Further it is demonstrated that the same modelling approach is also valid for desiliconized C/C-SiC.

In the next step, artificial interlaminar cracks were introduced into standard desiliconized C/C-SiC material. Therewith the crucial fracture mechanical parameters, i.e. the critical energy release rates under mode I and II loading, were determined. The critical energy release rates were then used in Finite Element Analyses (FEA) and validated by comparing numerical results with the fracture mechanical tests.

Finally, the modelling approach was transferred on samples with manufacturing defects. For this reason 3-point bending samples from reject plates were taken and investigated by micro-CT. Two approaches were used to model the behaviour of C/C-SiC with delaminations: First, FE-meshes were generated directly from 3D-grey scale data. Because of the complex meshing, based on micro-CT-data, advanced material models could not be readily included in the FEA. Only linear elastic analyses were performed. Therefore a second approach was used. Geometrical defect information was evaluated from 3D-CT-data and therewith equivalent 2D-FE-models were designed. The 3-point bending models were validated by comparing the load-deflection data from experiment and FEA. The FEA of delaminated samples included the geometrical information, i.e. defect shape, size and location, from CT-evaluations and the material models validated on standard material. The 3-point bending test was used for the evaluation of the modelling approach for the following reasons:

- The bending test is rather simple considering the load introduction. Distortions due to clamping, like in tensile or compression testing, can be excluded.
- Three clearly differentiated failure modes may occur in bending test: compression, tensile and interlaminar shear failure.
- Interlaminar failure is caused by pure mode II loading.
- The stiffness, failure load and failure mode of bending samples strongly depend on the size, shape and location of defects. Those points are also decisive for modelling a structural part with defects. The bending test is therefore rather close to a component test.

For those reasons the 3-point bending test was considered to be an advantageous test giving detailed information in what extend the modelling was successful or not.

3. State-of-the-art in CMC technologies

3.1 Processing and microstructure of C/C-SiC

The C/C-SiC material was developed at the DLR Institute of Structures and Design in Stuttgart. It is produced by the Liquid Silicon Infiltration process (LSI) [1]-[7]. The corresponding microstructures for the subsequent processing steps are shown in Figure 1. First a Carbon Fibre Reinforced Polymer (CFRP) body is produced by autoclave technique, warm pressing or Resin Transfer Molding (RTM). This CFRP body is then pyrolyzed under nitrogen atmosphere. Thereby the polymer matrix is converted into pyrolytic carbon. Finally, the porous C/C-green body is infiltrated with molten silicon. The silicon is distributed in the C/C-body by capillary force only. The liquid silicon reacts with the C-matrix and part of the C-fibres to SiC. Because of the strong block-wise segmentation of fibre bundles in C/C state most of the C-fibres remain unaltered. Figure 1 c shows the SiC-matrix (light grey) surrounding the C-fibre bundles (dark colour).

If C/C-SiC is produced for application temperatures above 1400°C, e.g. for re-entry applications, the residual free silicon (white colour in Figure 1 c) will be removed by a final desiliconization step. Graphite granulate is applied on the C/C-SiC surface to absorb the residual silicon at temperatures of about 1500°C.

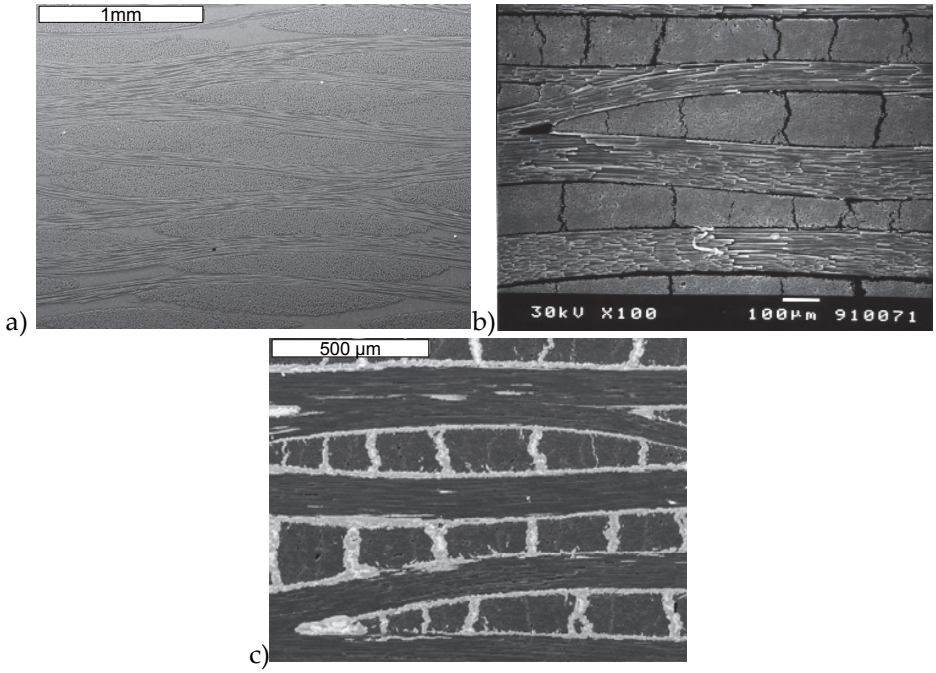

Figure 1: Microstructures of LSI-processing steps: CFRP (a), C/C state (b), C/C-SiC state (c).

3.2 State-of-the-Art in mechanics of CMCs

3.2.1 *Differentiation between WIC and WMC materials*

CMCs are usually divided into two groups, namely Weak Interface Composites (WICs) and Weak Matrix Composites (WMCs).

WIC materials typically have a weak interface in order to allow debonding between fibres and matrix. In that way the fracture toughness of the composite is increased [8]-[10]. In contrast, WMCs show a weak and soft matrix which allows multiple microcracking. The fibres provide strength and fracture toughness. Figure 2, the He-Hutchinson plot [11], shows the dependency of failure mode on the relative fracture energy of interface and fibre (Γ_i/Γ_f) as well as the stiffness ratio of fibre and matrix. The graph is demonstrating: if the Young's modulus of matrix and fibre are similar then the fracture energy of the interface relative to the fibres must be rather low ($\Gamma_i/\Gamma_f < 0.25$) to provide non-brittle failure (WIC). If the stiffness of the matrix is much lower compared to the fibres (WMC), the plot shows that interface properties will play a minor role. The C/C-SiC material is showing typically, compare Figure 1 c, a dense SiC matrix with microcracks from LSI processing. Further the microstructure shows a block by block build-up. Within the rectangular C/C-bundles residual pyrolytic C-matrix is contained. The stiffness of the SiC-matrix is rather high. In contrast the stiffness of the porous C-matrix is rather low. A defined interface between fibres and matrix, e.g. due to fibre coating, does not exist for C/C-SiC materials. Therefore C/C-SiC may not be classified as a typical WIC or WMC material from a microstructural point of view.

The stress-strain behaviour of typical WIC and WMC materials in Figure 3 shows that the classification due to the macroscopic behaviour is also not clear for C/C-SiC. The WIC materials show similar behavior in 0/90° and 45° direction. In contrast, the WMC material shows strong differences. In 0/90° direction the behaviour is almost linear elastic. In 45° direction it is strongly non-linear. The stress-strain behaviour of the investigated C/C-SiC material is similar to WMCs. On the other hand the strengths of the C/C-SiC material in 0/90° and 45° direction are almost on the same level, see Figure 19, which makes it comparable to WICs. Koch et al [10] showed for C/C, a typical WMC, that macroscopic modelling of its mechanical behaviour is possible. In contrast Lamon et al. [12] showed that for WICs, like Chemical Vapour Infiltrated (CVI) SiC/SiC, a micromechanical approach is useful. Because of its microstructure and related mechanical behaviour C/C-SiC is neither a typical WMC nor a WIC material. Nevertheless Weigel et al. [13] suggested a micromechanically based continuum damage approach for C/C-SiC. In the following, however, it will be shown that the stress-strain behaviour and failure of C/C-SiC can be modelled by

homogenized constitutive equations with the use of only a few experimentally determined parameters. The approach is therefore similar to the macroscopic yield and failure model by Fink [14].

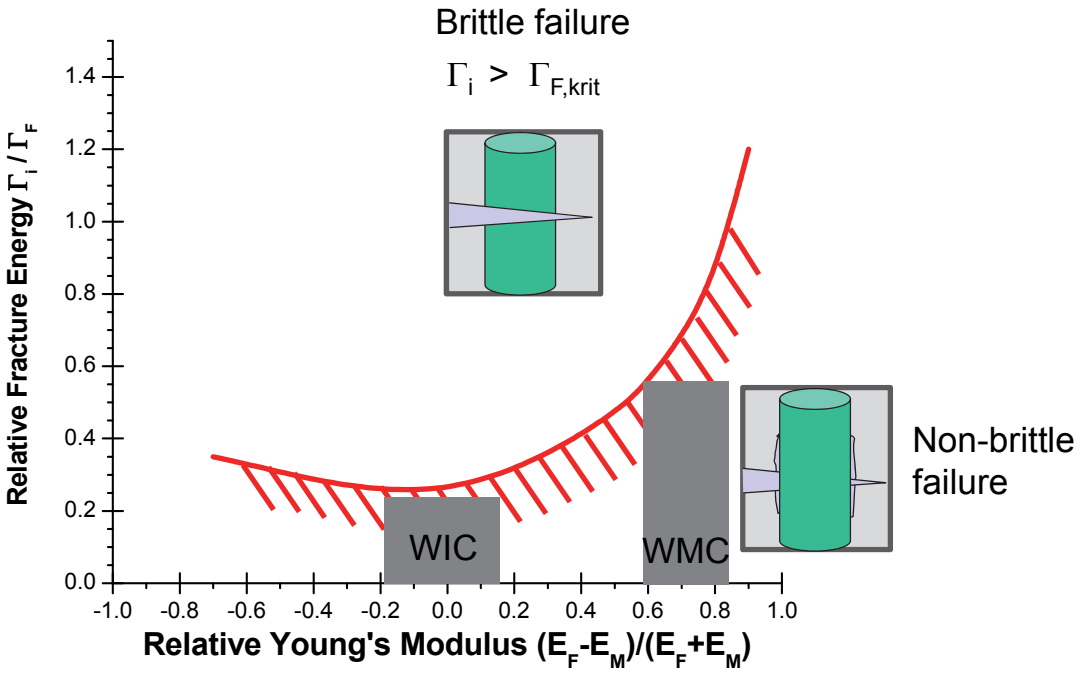

Figure 2: Explanation of brittle and non-brittle CMC behaviour according to He and Hutchinson [10] [11] (adapted with kind permission from Elsevier).

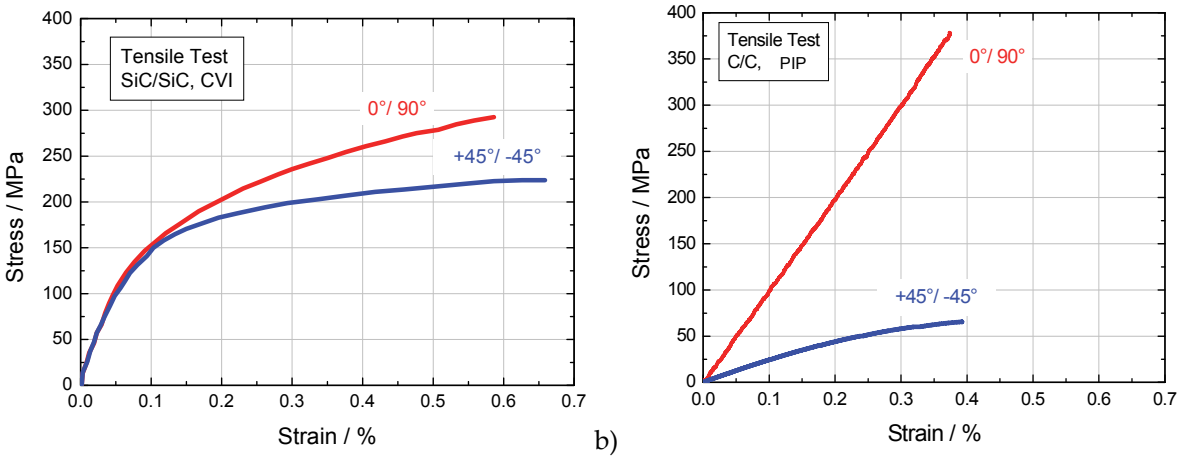

Figure 3: Representative stress-strain curves of a WIC (SiC/SiC by CVI) (a) and a WMC (C/C by Polymer Infiltration and Pyrolysis, PIP) (b) from axial and diagonal loaded tensile test [10] (adapted with kind permission from Elsevier).

3.2.2 *Bending and tensile strength ratio*

It is a common observation, that the bending strength of CMC materials is usually much higher than the strength under tensile loading. Since the 3-point bending test is used in the present work for evaluating the impact of defects on the mechanical behaviour, this fact had to be considered in more detail. The difference between tensile and bending strength was shown experimentally in a number of publications for various CMCs [15]-[18] and is going to be investigated in detail for the C/C-SiC material in the following. In the past, different explanations were found. Marshall and Evans [16] showed for an unidirectional SiC-fibre glass-ceramic composite that fracture mechanical analysis is not appropriate to explain the elevated bending strength because failure did not occur as one single planar crack but mainly shear failure was observed in Single Edge Notched Bending, SENB, test. Therefore Marshall and Evans [16] proposed that micromechanical properties like interface strength and statistical strength of fibres have to be considered. Hild et al. [19] followed the idea from Marshall and Evans and considered additionally the theory of global load sharing. In that way Hild et al. [19] showed that two factors are influencing the ratio of bending to tensile strength. Those are the ratio of tensile-to-compressive secant modulus caused by matrix cracking, leading to a shift of the neutral plane, and further the Weibull modulus of fibre strength. The tensile and bending strength for three different Nicalon fibre reinforced CMCs were closely predicted following this approach. For the prediction of tensile and bending strength the micromechanical properties fibre strength, its Weibull modulus and the interfacial sliding stress were necessary. In contrast Steif and Trojnacki [20] demonstrated that the ratio of bending to tensile strength depends mostly on the stress-strain behaviour after reaching ultimate tensile strength. Especially composites, failing non-brittle in tensile testing, show a comparatively high bending strength. For materials behaving linear elastic-ideal plastic in tension and linear elastic in compression a ratio of 3 can be reached. The factor of 3 was demonstrated earlier also by the theoretical work of Laws and Ali [21]. Steif and Trojnacki [20] investigated the influence of the behaviour after peak tensile stress and the influence of slope change reaching proportional limit under tensile loading. The effect of the slope change caused by matrix cracking under tensile load was shown to have only modest influence on the bending-tensile strength ratio. Mainly the stress-strain behaviour beyond ultimate tensile stress was influencing the bending-tensile strength ratio. The main drawback of the work from Steif and Trojnacki [20] is that the slope after reaching ultimate tensile strength cannot be determined for most CMC materials since they fail rather brittle under tensile load. The herein investigated C/C-SiC is also failing brittle under tensile load.

In contrast to Marshall and Evans [16], Fink [14] was using a fracture mechanical approach to explain the difference between bending and tensile strength of CMCs. Fink [14] demonstrated that the bending strength of C/C-SiC could be much higher than the tensile strength if the fracture toughness of the material was considered. Fink

[14] was using a smeared softening rule to model the behaviour after ultimate tensile strength with fictitious energy release rates, since experimental values were not available.

In the present work the bending behaviour of C/C-SiC under varying loading directions is going to be modelled considering the differing stress-strain behaviour under tensile and compression load as proposed by Hild et al. [19]. Failure is modelled by a fracture mechanical cohesive zone approach accounting for the directional ultimate tensile strength values and the critical energy release rates [22]. The critical energy release rate, or respectively the WOF, is determined by SENB testing.

It will be shown that the ratio of bending to tensile strength can only be partially explained by the differing stress-strain behaviour under tensile and compression load but taking additionally the fracture toughness of the CMC material into account the bending strength can be modelled in good agreement with the experimental results.

3.2.3 *Interlaminar fracture mechanics*

In contrast to the in-plane mechanical properties, less literature is found considering the interlaminar properties of CMCs. Nevertheless testing methods used for Carbon Fibre Reinforced Polymers (CFRPs) could be adapted for CMC materials. Kuntz [23] e.g. investigated fibre reinforced glass with End-Notched Flexure (ENF) testing and determined the critical energy release rates following beam theory. Although the results showed strong variations, an average critical energy release rate in mode II, G_{IIc}, of 0.229 N/mm was determined for SiC-Nicalon fibre reinforced Duran-glass. The G_{IIc} for carbon fibre reinforced Duran-glass was determined to be 0.049 N/mm. Krombholz and Goldstein [24] investigated the interlaminar fracture toughness of C/SiC by compact tension shear (CTS) testing [25] in combination with the mounting device presented by Richard and Benitz [26]. The main problems of interlaminar testing of CMCs, as described by Krombholz and Goldstein, are:

- The insertion of interlaminar cracks into defined interfaces is difficult because of the waviness of laminate layers. The creation of interlaminar defects by insertion of foils was not possible because of the material processing.
- The determination of crack length and crack front geometry was not possible during testing.

That is why the experimental results of Krombholz and Goldstein [24] had to be correlated with FE-results to determine the critical energy release rates under varying mode I and II ratios. The average G_{Ic} for C/SiC was determined to be 0.002+/-0.001 N/mm. A G_{IIC} value under pure mode II loading was not determined.

Similar problems appeared during interlaminar testing of C/C-SiC with DCB (Double Cantilever Beam) and ENF set-up for the present work. The insertion of foils was problematic due to the high temperatures and the infiltration with liquid silicon during the LSI process. Nevertheless, a starter crack could be inserted by abrasive cutting. The crack length could be estimated only due to contrast enhancement by painting of the C/C-SiC surfaces.

3.3 Defects in CMC samples and structures

The impact of interlaminar defects, i.e. mainly delaminations, is investigated in detail because delaminations are the typical macroscopic defects observed in C/C-SiC samples and structures. Figure 4 shows exemplarily some C/C-SiC structures with delaminations. Delaminations occur mainly during the pyrolysis of curved structures but they can also occur in plate material, as will be shown in chapter 5.2. The main reason for the delamination during pyrolysis is the strong shrinkage of the polymer matrix. The strong shrinkage of the polymer matrix relatively to the fibre reinforcement is leading to a higher shrinkage in thickness direction than in fibre-direction. In that way high internal stresses are created, especially in curved structures like tubes e.g., Figure 4 a.

Similar defects were also documented by Schmidt et al. [27][28] for carbon fibre reinforced silicon carbide, C/SiC, structures, produced by PIP (Polymer Infiltration and Pyrolysis) technique.

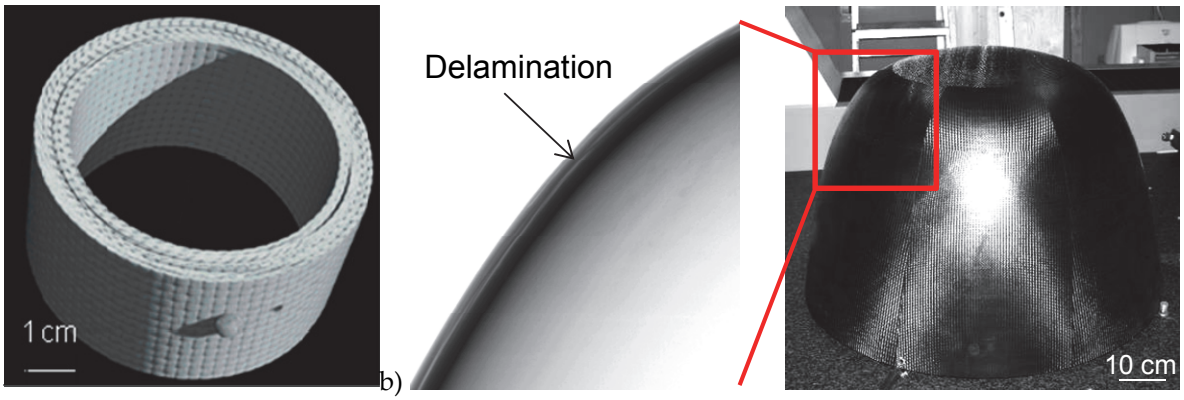

Figure 4: Exemplary defects in LSI materials and structures: tube (a) and thermal protection system with delaminations in x-ray radiography (b) [29].

Figure 5 shows another kind of typical interlaminar defect in C/C-SiC structures: pores in joining areas. The cross-section from micro-CT analysis reveals pores in the joining area of a rejected load introduction for the re-entry experiment EXPERT [29].

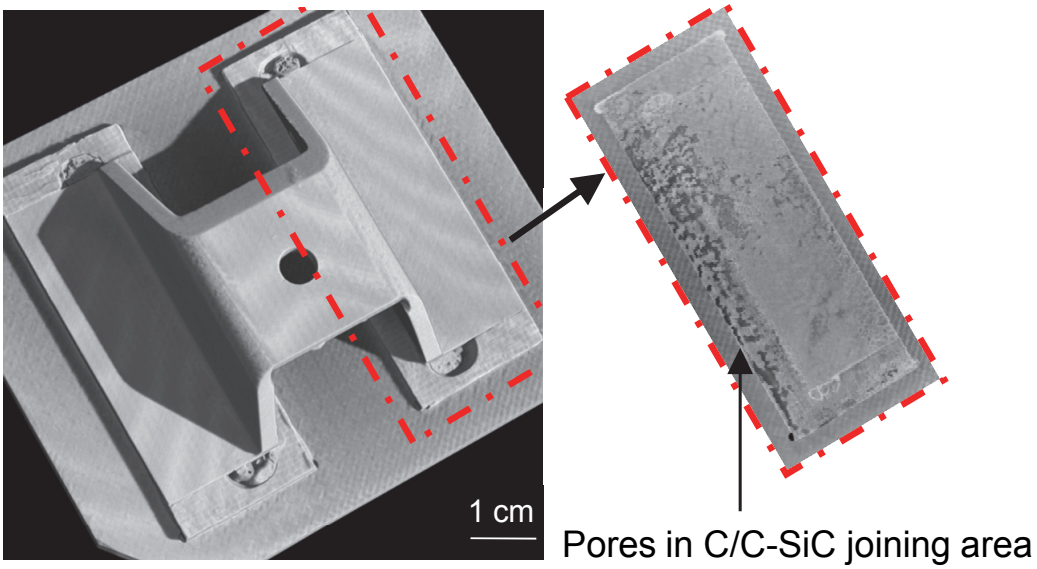

Figure 5: 3D visualisation of a C/C-SiC load introduction and 2D cross-section through the porous joining area from micro-CT analysis [29].

Different kinds of defects are observed in CMC materials depending on the processing and fibre architecture. The various manufacturing defects are still limiting the use of CMC materials for industrial applications. Therefore methods are needed which are able to predict the impact of defects on the integrity of CMC structures. Abdul-Aziz et al. e.g. [30][31] investigated the impact of matrix porosity on the stress distribution in liquid silicon infiltrated SiC/SiC tensile samples by linear elastic FEA. The approach from Abdul-Aziz et al. was based on generating FE-models directly from grey scale CT-data sets. This approach is also going to be used and investigated in chapter 7.2 in order to predict the impact of interlaminar defects on the stiffness of C/C-SiC bending samples. In chapter 7.3 the defect information from CT-data is further used to create simplified 2D-FE-models, including a fracture mechanical approach, which makes it possible to predict the stiffness and failure load of C/C-SiC with delaminations in detail.

3.4 Motivation

In order to describe the effect of interlaminar manufacturing defects on the mechanical behaviour of C/C-SiC the following subgoals had to be reached: first the difference between tensile and bending strength of C/C-SiC without manufacturing defects had to be explained and modelled by FEM. Since C/C-SiC is not a volume-dependent Weibull material, as it will be shown in chapter 6.1.1, statistical analysis were not performed as suggested by Hild et al. [19]. In contrast, a fracture mechanical

explanation of bending strength was chosen similar to the work of Fink [14]. Instead of using a smeared softening law as implemented by Fink [14] the goal was to use CZEs, representing the macroscopic crack path. CZEs are closer to the reality where single macroscopic cracks are observed, as will be shown in chapter 7.3.1.2., Figure 75.

All necessary input parameters were determined by mechanical testing.

In contrast to the results from Marshall and Evans [16] SENB testing was successful for the investigated C/C-SiC material: failure occurred by one single, rather planar crack [22]. Shear failure was not observed because the interlaminar shear strength of 0/90°-reinforced C/C-SiC is relatively high compared to the unidirectional composite investigated by Marshall and Evans [16].

Therefore, the Work of Fracture (WOF) could be determined from SENB tests and was used to model the behaviour beyond ultimate tensile strength as linear stress-separation curve with CZEs. The softening law as introduced by Alfano and Crisfield [32] for interlaminar crack propagation in CFRPs was adapted for the translaminar failure of C/C-SiC.

The second subgoal was to determine the interlaminar energy release rates under mode I and II loading and to reproduce the experimental results with adequate interlaminar cohesive zone models. The energy release rates were determined from artificially pre-cracked samples following ASTM (American Society for Testing and Materials) and Airbus Industry Test Methods (AITM) [33]-[35], which were developed for fibre reinforced polymers. The test methods were adapted for the C/C-SiC material. The results were then compared with fracture mechanical solutions which were also introduced for fibre reinforced polymers by Szekrenyes [36] and Allix et al. [37].

Finally the cohesive zone approach, which was based on results from artificially pre-cracked samples, had to be evaluated for samples taken from delaminated reject plates containing true manufacturing defects.

In addition to the work from Abdul-Aziz et al. [29][31] the goal was not only to predict critical stress concentrations but further the stiffness and maximum load of CMC samples with manufacturing defects.

After all, a new classification for CMC materials had to be introduced because C/C-SiC may neither be classified as WIC nor as WMC material following the definition by Koch et al.[10], see chapter 3.2.1.

4. Experimental Set-up

4.1 NDI Set-up

Air-coupled ultrasonic (US) testing and micro-Computer Tomography (CT) were used to investigate plate and sample materials.

4.1.1 *Ultrasonic testing*

Air-coupled ultrasonic testing was performed in transmission mode with a device from Second Wave Systems Corp., see Figure 6. The step motor is driving the transducer and detector altogether over the sample surface. The transducer is emitting an ultrasonic signal with a frequency of 100 kHz. The attenuation of the signal is measured with the detector at the lower side of the sample. Since any interface is causing a scattering of the ultrasonic signal, US-testing is especially sensitive to detect pores and delaminations. The in-plane resolution is related to the step size which was set to 2 mm.

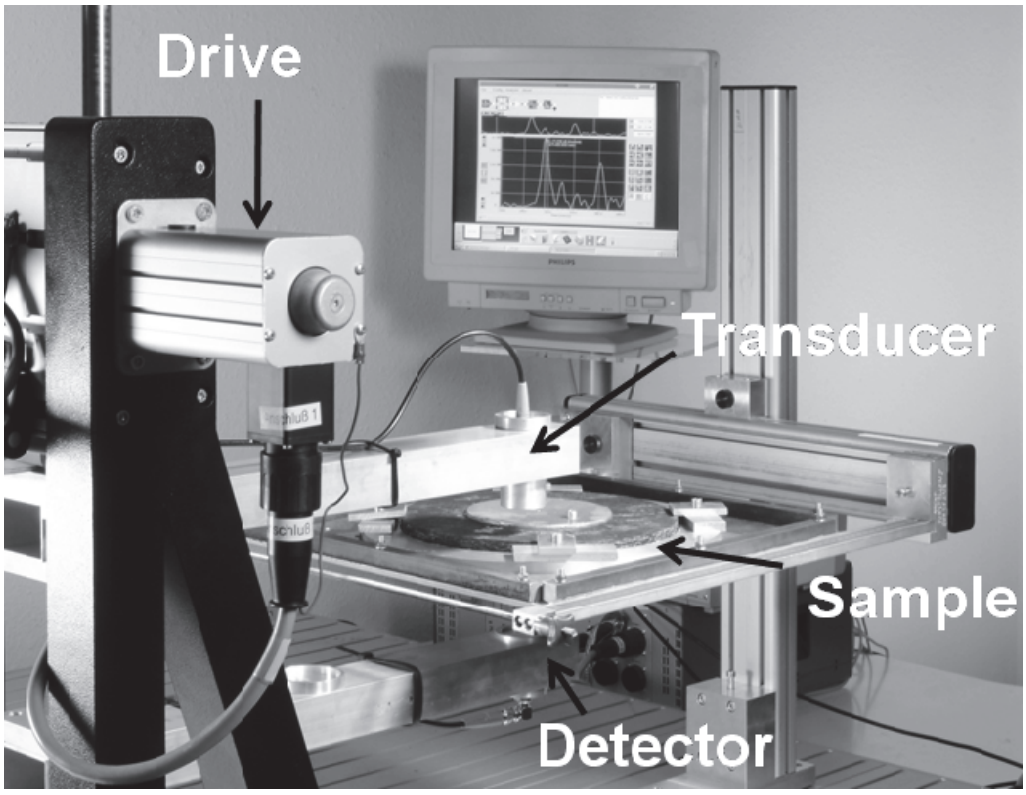

Figure 6: Set-up for ultrasonic testing.

4.1.2 *Micro-Computer Tomography*

All CT-scans were performed using the vtomex L450 x-ray device from Phoenix X-ray/GE. Figure 7 shows the fundamental set-up: 240 kV x-ray tube, sample on rotating fastener and x-ray detector.

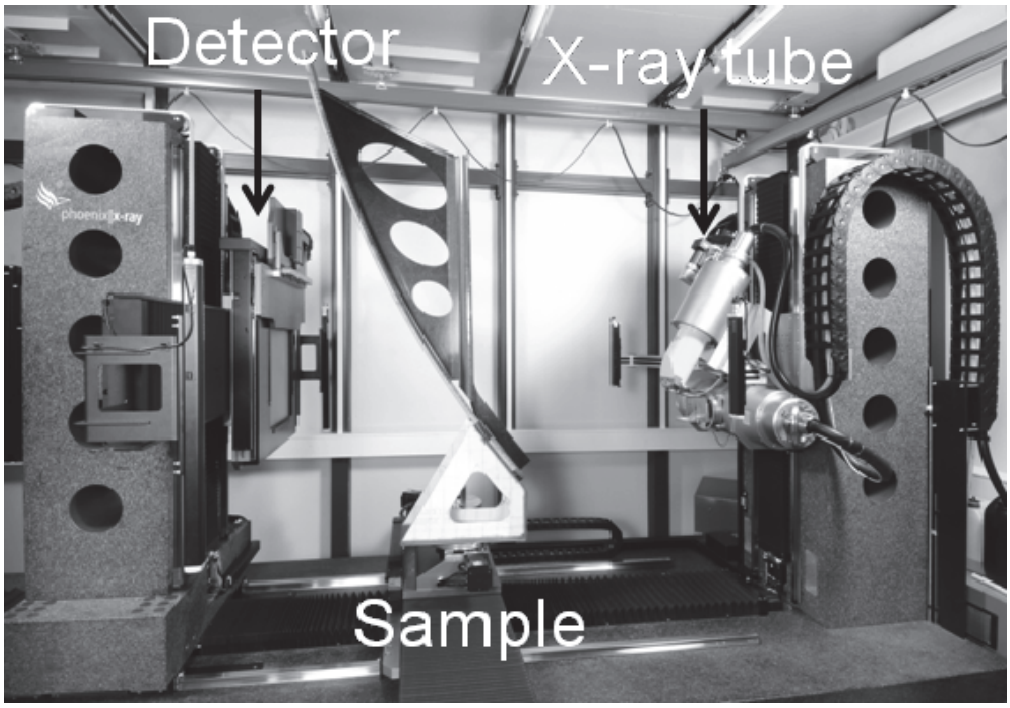

Figure 7: Vtomex L450, micro-CT device, from Phoenix X-ray/GE with a 240 kV x-ray tube at the DLR.

4.2 Mechanical testing

Table 1 gives an overview of the investigated plates, performed mechanical tests and the respective load orientations. Some of the plates were investigated in desiliconized state. This is also mentioned in Table 1. In order to differentiate between delaminated plates and plates with no delamination the endings _D and _ND are introduced. The definition of delaminated plates is given in chapter 5.2. Plate PH2035_ND was mainly used for investigating the in-plane behaviour of C/C-SiC in varying orientations. Plate PH1991_ND was investigated in Double Cantilever Beam (DCB) and End-Notched Flexure (ENF) test for the determination of interlaminar properties. Plate PH1879_D showed large delaminated areas in the C/C and desiliconized state, as will be shown in chapter 5.2. For that reason PH1879_D was used to investigate the influence of free silicon on the mechanical behaviour in siliconized state. In desiliconized state PH1879_D was used to validate the developed FE-approach to predict the influence of

delaminations on the mechanical behaviour. A cut-off section from a delaminated reject plate was used for preparing short-beam bending samples and comparing the results from bending test with the results from FE-models created directly from meshed grey scale CT-data.

Table 1: Investigated plates, performed mechanical tests and loading directions.

	PH2035_ND	PH1991_ ND	PH1991_ ND Desil.	PH1879_ D	PH1879_ D Desil.	Reject cut-off_D
Tensile	Vary. Orientations	0/90°	0/90°	-	-	-
3-Point Bending	Vary. Orientations	0/90°	0/90°	0/90°	0/90°	0/90°
4-Point Bending	-	0/90°	0/90°	-	-	-
SENB	Vary. Orientations	-	-	-	-	-
DCB	-	0/90°	-	-	-	-
ENF	-	0/90°	-	-	0/90°	-

4.2.1 *In-plane testing: bending, tensile and SENB testing*

All mechanical tests were performed in a universal testing machine (Zwick) at room temperature. The tensile tests were performed with two strain gauges in longitudinal and one strain gauge in transverse direction. In 4-point bending strain gauges were applied on the top and bottom side of the samples in longitudinal direction.

In 3-point bending strain gauges could only be applied at the bottom side opposite to the point of load transmission. The bending tests in 0/90° direction were performed with ratios of support distance, L, to thickness, d, ranging from 2.5 to 25. In all other directions 3-point bending was performed with L/d~ 20. Table 2 gives an overview of the performed mechanical tests, their geometries and loading orientations.

Table 2: Test geometries and orientations.

Test	Test Geometries	Investigated orientations	3rd dimension/ mm
Tensile	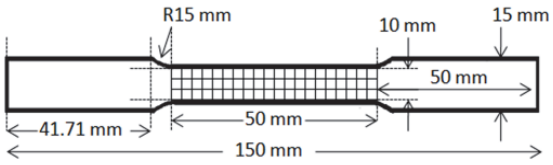	0/90°, 15/75°, 30/60°, 45°	2.3/ 5
3-Point Bending	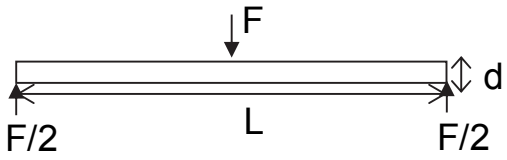	0/90°, 15/75°, 30/60°, 45° (L/d=2.5-25)	10
4-Point Bending	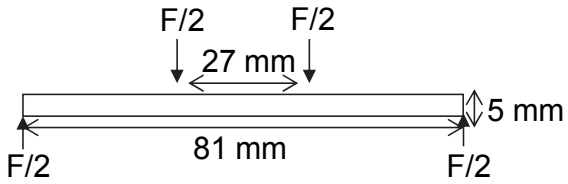	0/90°, 45°	10
SENB	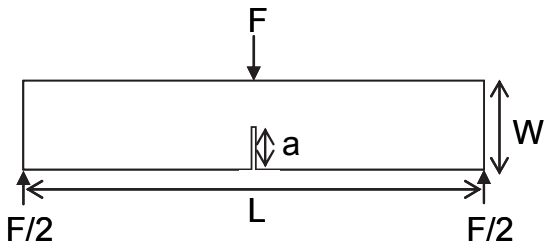	0/90°, 45°, 90/0° (in-plane: L=22.5 mm; W=4.4 mm), 0/90° (translaminar: L=14 mm; W=3 mm)	2.3 in-plane; 10 trans-laminar

The SENB tests were conducted similar to the work from Kuntz [23]. The pre-notch a was introduced by abrasive cutting with a saw blade of 300 µm thickness. The SENB tests were performed to investigate the fracture toughness in four different notch orientations relative to the carbon fibre fabric:

- the in-plane fracture toughness with fibre orientations relative to the crack of 0/90°, 45° and 90/0°
- the translaminar fracture toughness for a crack orientated perpendicular to the 0/90° fabrics.

Figure 8 illustrates the investigated orientations.

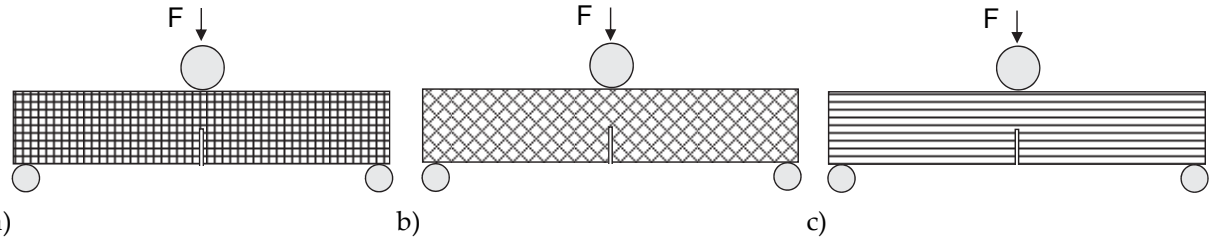

Figure 8: SENB-orientations: in-plane in 0/90°- or 90/0°- (a), 45°-orientation (b) and translaminar with 0/90°-fibre orientation (c).

For in-plane SENB testing the samples had a height W of about 4.4 mm, the width was 2.3 mm and the outer span was set to 22.5 mm. For translaminar SENB tests the notch was introduced perpendicular to the fabric layers. The samples had a height of about 3 mm and the outer support distance was set to 14 mm. Different ratios of initial crack length to sample height were investigated for all orientations. The K_{Ic} value, that is the critical stress intensity factor, was determined from the load maximum following the equations from Tada et al.[38]. Additionally the WOF was determined from the area under the load-displacement curves as described by Nakayama [39]. The used equations and detailed evaluation are shown in chapter 6.1.3 together with the respective results. The translaminar SENB samples were also used to compare the K_{Ic} value obtained from pre-notched and pre-cracked samples. For this reason the pre-notched samples were tested until first failure, then the created crack length was determined and the samples were loaded to complete failure. The results in chapter 6.1.3 show that the K_{Ic} values, obtained from pre-notched and pre-cracked samples, are comparable. That is why the other orientations were investigated with pre-notched samples only. Five samples per orientation were evaluated for tensile, 3-point and 4-point bending. All bending samples failed due to tensile cracks. Compression or shear failure was not observed for standard material without interlaminar defects. In SENB testing at least four samples per direction were analysed.

4.2.2 *Interlaminar mechanical testing*

The following two chapters, 4.2.2.1 and 4.2.2.2, give an overview of the DCB and ENF test set-up. The detailed evaluation methods and equations are shown in chapter 6.1.4. with the related results.

4.2.2.1 Mode I interlaminar testing: DCB

Double-cantilever beam tests were performed similar to the ASTM D 5528–94a standard [33] for the determination of mode I interlaminar fracture toughness of

unidirectional fibre-reinforced polymer matrix composites. The pre-notch was introduced by abrasive cutting with a saw blade of 300 µm thickness. A sharp pre-crack was then introduced by opening the sawed crack front with a scalpel. The initial crack front was then marked under the light microscope and used to calculate the initial crack length a. Aluminium blocks with drilled holes were glued with adhesive X60 on the outer surfaces of the two cantilevers. A steel pin connected the aluminium blocks on each side to the load introductions of the Zwick machine, see Figure 9. The ASTM standard is describing different methods to determine the critical energy release rate in mode I, G_{Ic}:

- Deviation from linearity in load-deflection curve
- Visual observation of crack propagation
- 5%-offset or maximum load

For brittle matrix composites the deviation from linearity should correspond to the visual observation of crack propagation. For tough matrix composites first non-linearity may be observed before crack growth is visually detected. For the investigated C/C-SiC material a visual observation of the crack initiation was not possible. In addition the C/C-SiC material itself was showing non-linear behaviour under those load conditions. That is why the 5%-offset method was used. In that case the intersection point of the load deflection curve with a 5%-decreased stiffness curve was determined to calculate the G_{Ic} value. The further evaluation followed the ASTM standard. Additionally the G_{Ic} value was evaluated following an Airbus Industry Test Method (AITM) [34] to compare the obtained results. The investigated samples had a height of about 5 mm, 10 mm of width and about 50 mm length. Therewith the test geometry deviated from the AITM and ASTM standard geometries (length > 125 mm, width = 20-25 mm) [33]. Nevertheless the geometrical guidelines of the ASTM standard were fulfilled. Those are:

$$a \leq 0.042 \sqrt{\frac{h^3 E}{G_{Ic}}} \quad \textbf{(1)}$$

$$t \leq \frac{h}{4} + 0.01 \sqrt{a^2 + \frac{0.0434 h^3 E}{G_{Ic}}} \quad \textbf{(2)}$$

$$h \geq 8.28 \sqrt[3]{\frac{a^2 \, G_{Ic}}{E}} \quad \textbf{(3)}$$

with the sample height h, the initial crack length a, E the Young's modulus in longitudinal direction and G_{Ic} the critical energy release rate. The test speed was set to 1 mm/min. During testing the GOM Aramis System for optical strain measurement was used to take images at defined load steps. Therefore all samples were painted with black and white speckle pattern before testing. The painting of the sample surfaces also helped for the observation of crack propagation.

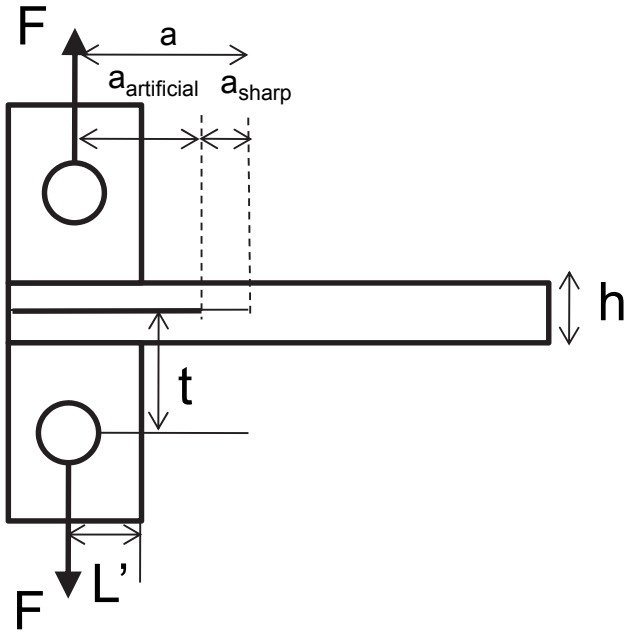

Figure 9: Test geometry for DCB interlaminar mode I testing.

4.2.2.2 Mode II interlaminar testing: ENF

The critical energy release rate in mode II, G_{IIc}, was determined similarly to the Airbus Industry Test Method (AITM) for fibre reinforced plastics [35]. The test geometry was adapted for the C/C-SiC material. The AITM standard suggests a support distance of 100 mm, width of 25 mm, height of 3 mm and an initial crack length of 40 mm. The C/C-SiC samples had a height of about 5 mm, width of 10 mm and varying initial crack lengths. An empirical approach was used to choose the right support distance for the C/C-SiC material. First, a support distance of 100 mm was used. All samples failed due to bending failure. Interlaminar crack propagation was not observed. Consequently a shorter support distance of 25 mm was used to cause higher interlaminar shear stress relative to the bending stress. As expected shear failure occurred. Because of the short beam length only little crack propagation and variations of initial crack length were possible. That is why finally a compromise of 50 mm support distance was chosen. The pre-notch was again introduced by abrasive cutting with a saw blade of 300 µm thickness. Afterwards a sharp pre-crack was introduced by opening the sawed crack front with a scalpel. Again, the initial crack

front was marked under the light microscope and used to calculate the initial crack length a. In between of the sawed crack part an aluminium plate was positioned to fill the gap produced by sawing, see Figure 10. In that way additional bending of the lower cantilever beam should be reduced. The test speed was set to 0.1 mm/min. All samples were sprayed with white colour to increase contrast and facilitate the observation of crack growth. A digital camera was used to take images at defined load steps during testing. The evaluation of G_{IIc} followed the equations from AITM-standard [35], Szekrenyes [36] and Allix et al. [37]. The relevant equations are shown in chapter 6.1.4.2 together with the evaluation of test results.

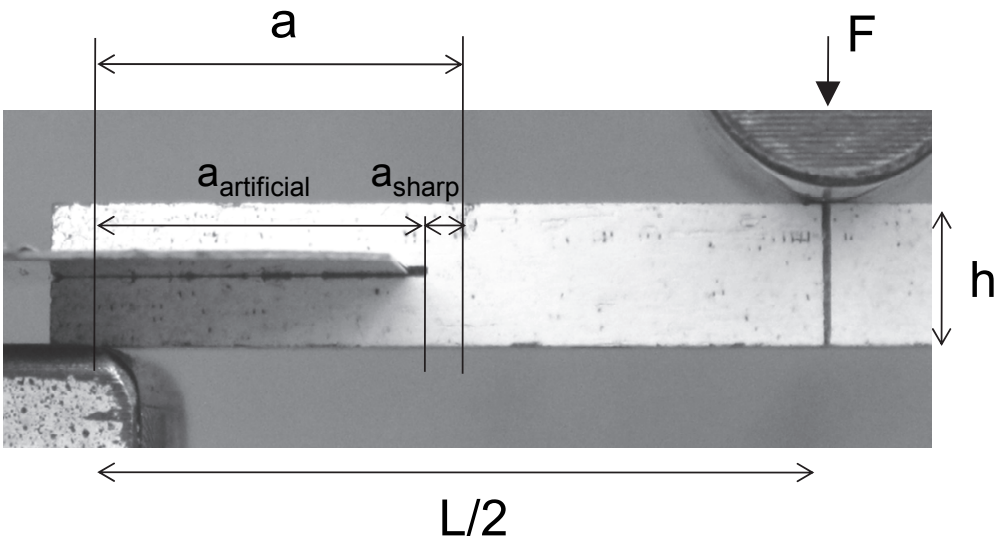

Figure 10: Pre-cracked part of ENF test set-up.

5. Investigated material

The investigated material C/C-SiC was produced in-house at the German Aerospace Centre, DLR, Institute of Structures and Design, by LSI process. Standard C/C-SiC plates of 330 x 330 mm² were produced out of HTA woven fabric layers. The weft and warp directions of the fabric were switched after each layer to get similar mechanical properties in 0 and 90° direction. After silicon infiltration all plates were ground to get even surfaces and the desired thickness. The dog-bone specimens for tensile testing were cut by water-jet. The samples for bending, SENB, DCB and ENF testing were produced by abrasive cutting.

5.1 Processing of plate materials

All investigated plates were produced following the LSI process as described in chapter 3.1. The CFRP bodies were produced in autoclave technique from twill 2/2 pre-pregs, except for the reject cut-off_D which was produced in RTM technique from dry plain fabric. Table 3 is summarizing the main properties of the investigated plates. The plates PH2035_ND and PH1991_ND are standard materials without delaminations. They were used to investigate the in-plane properties without manufacturing defects and the interlaminar properties with inserted artificial pre-cracks. In contrast the reject cut-off_D and PH1879_D showed strong delaminations. The reject segment was used to evaluate the bending FE-models created from micro-CT data directly. Plate PH1879_D was used to investigate the impact of free silicon on the mechanical properties and to evaluate the fracture mechanical FE approach, developed for predicting the behaviour of desiliconized C/C-SiC with delaminations.

Table 3: Properties of investigated plate material.

	Delamination	Thickness in CFRP / mm	Layers in CFRP / -	Fibre volume fraction in CFRP / %	Thickness of ground C/C-SiC / mm
PH2035_ND	No Delam.	3.2	13	58.6	2.3
PH1991_ND	No Delam.	12.5	51	56.8	4.92
PH1879_D	Delam.	6.6	27	56.9	5.12
Reject cut-off_D	Delam.	11	~45	~56	5.0

5.2 *Formation and definition of delaminations in C/C-SiC plate material*

First of all, Figure 11 shows the ultrasonic test results from plate PH1879_D at different processing steps. The delamination is clearly detected in the C/C state and in the desiliconized state. Only half of the plate was desiliconized. The delaminated regions can roughly be described by the regions of blue and black colours, i.e. high ultrasound attenuation, in the images from C/C and desiliconized state. The broad histograms in C/C state and desiliconized state also indicate delaminated regions. In CFRP state only minor inhomogenities are detected via ultrasonic testing. Nevertheless the plate delaminated during pyrolysis. During siliconization the delaminations were filled with free silicon. Other plates showed that it mainly depends on the height of delamination in C/C state if it is completely filled with silicon or not. In the case of plate PH1879_D the delaminations were completely filled, that is why ultrasonic testing of the siliconized state showed a rather homogenous result. During desiliconization the free silicon was removed again and the delamination shows almost the same extent as in C/C state. The first process step to differ between delaminated and standard plates is therefore the C/C state.

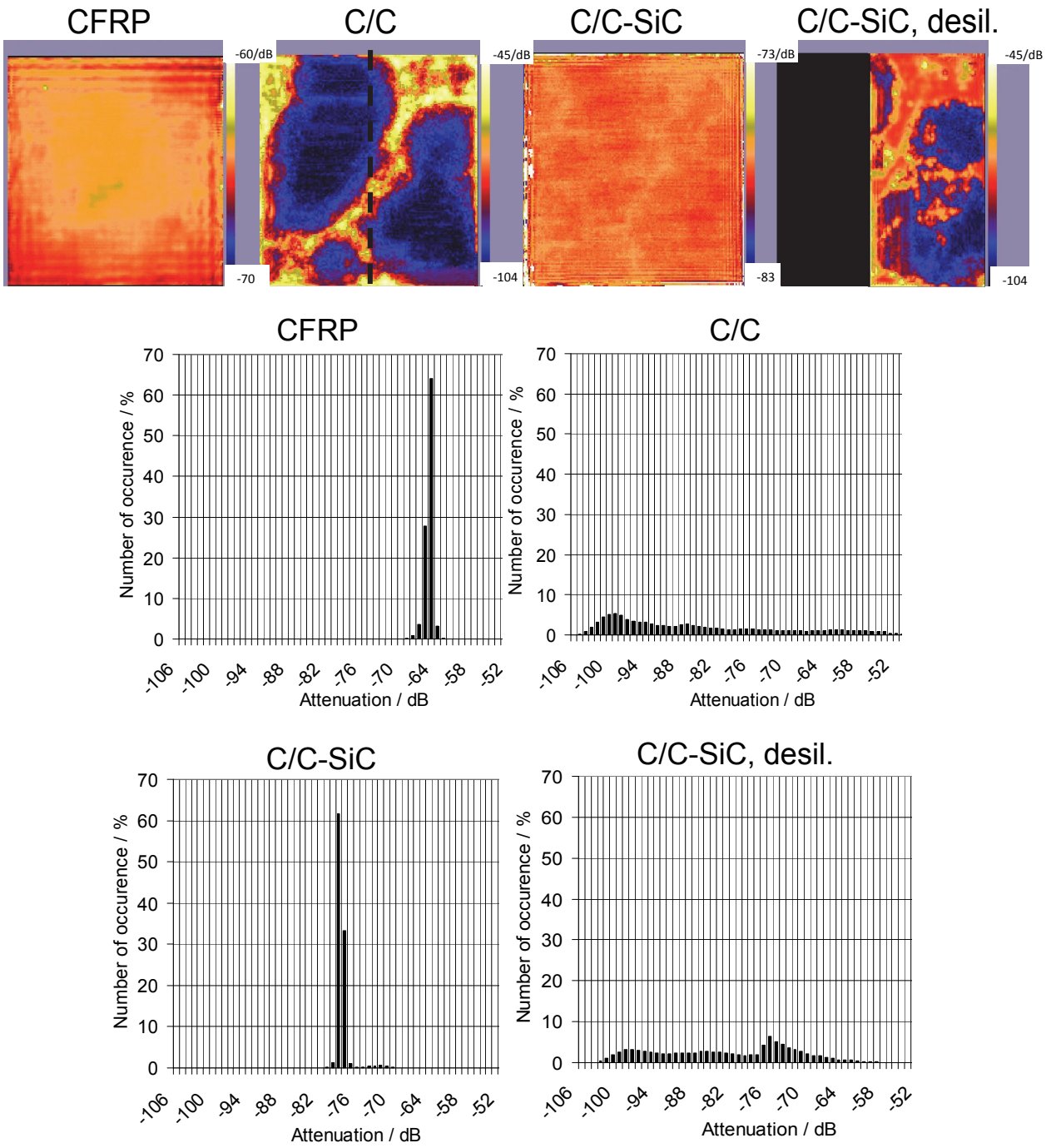

Figure 11: Ultrasonic test results of PH1879_D in subsequent processing steps, from left to right, and related histograms of ultrasound attenuation.

Figure 12 shows the CFRP and C/C state of PH2035_ND as well as the C/C state of PH1991_ND. PH1991_ND was scanned in C/C state only. The comparison of CFRP and C/C state of the plate PH2035_ND shows that certain inhomogenities from CFRP state are transferred to C/C state. It has to be emphasised here that especially PH2035_ND showed a rather homogenous histogram in CFRP state, see Figure 12. Nevertheless, the slight variations in CFRP state caused enhanced variations in

ultrasound attenuation in C/C state. Therefore it can be assumed that inhomogenities in CFRP state are enforced during pyrolysis and can possibly lead to delamination. The inhomogenities in CFRP state of plate PH1879_D, shown in Figure 11, could have contributed to the delamination in C/C state. In C/C state the delamination of PH1879_D is clearly indicated by a broad histogram with two major peaks and one of it at strong ultrasound absorption of -100 dB. In contrast, the standard plates PH2035_ND and PH1991_ND show rather homogenously distributed histograms in C/C state. Due to the ultrasonic results and related histograms a clear differentiation between delaminated and standard plates can be taken in C/C state.

The reason for delamination of even plates is not yet clear. Nevertheless the plates PH1879_D and PH2035_ND showed a strong influence of CFRP state on the distribution of porosity in C/C state. In general it was observed that thicker plates, with thicknesses over 5 mm, have a stronger tendency to delaminate as the thinner ones.

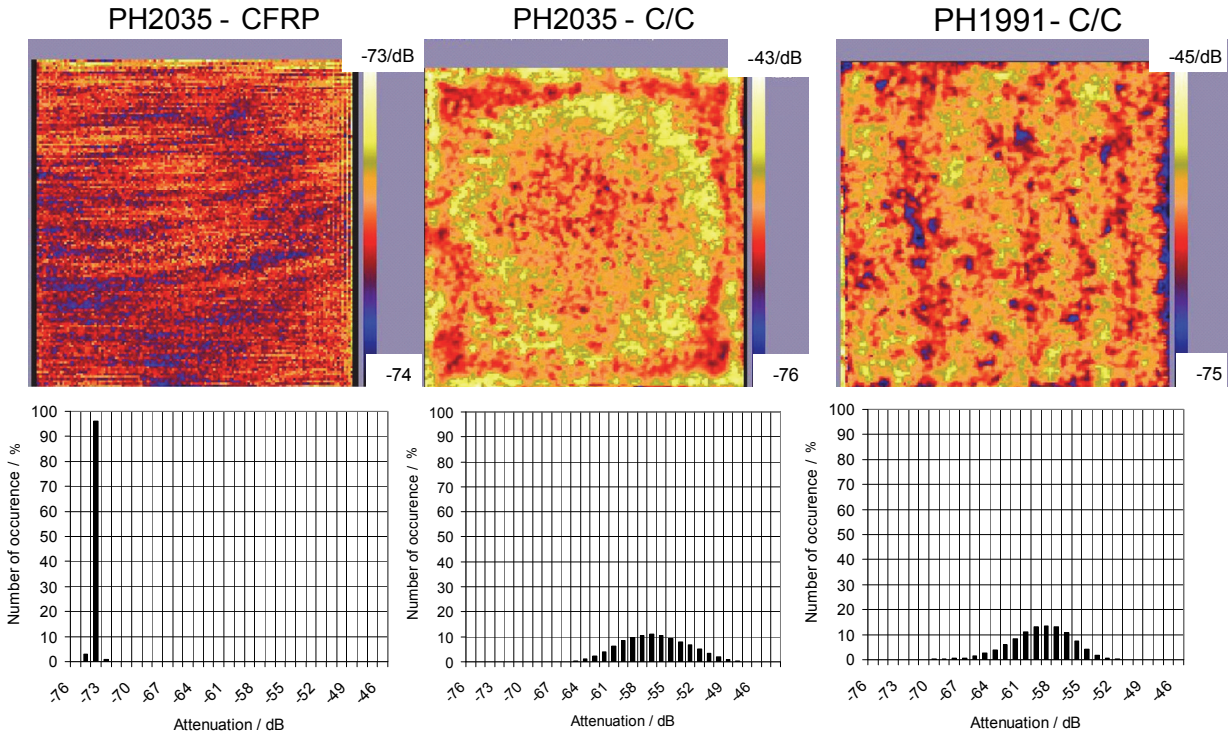

Figure 12: Ultrasonic test results of PH2035_ND in CFRP and pyrolyzed state, as well as PH1991_ND in pyrolyzed state only; the related histograms of ultrasound attenuation are shown.

6. Mechanical behaviour of C/C-SiC without manufacturing defects

The mechanical characterization and modelling of C/C-SiC without manufacturing defects is going to be described on the following pages. The critical energy release rates are going to be determined on artificially pre-cracked samples.

6.1 Experimental results

The subsequent experimental results describe the in-plane and interlaminar mechanical behaviour of C/C-SiC. The results were used as input and for the validation of the FE-modelling in chapter 6.2 and 7.3.2, respectively.

6.1.1 *Tensile and bending tests of siliconized and desiliconized C/C-SiC in fibre direction*

The results in this chapter were all measured from samples of plate PH1991_ND. One half of Plate PH1991_ND was desiliconized to get a direct comparison of the mechanical properties in siliconized and desilconized state. Figure 13 shows the Young's moduli evaluated from strain gauge measurements under tensile and bending load of siliconized C/C-SiC. The Young's moduli were evaluated for each sample in the same stress regime of 10-30 MPa by linear regression method. The bending stress was calculated following beam theory:

$$\sigma_b = \frac{1.5FL}{bd^2} \qquad \textbf{(4)}$$

with the load F, the support distance L, width b and height of the sample d. The Young's moduli of the different test methods are mainly in the range of 60-70 GPa. However a slight decrease in calculated Young's modulus is observed for decreasing L/d-ratios. This observation may be explained by the increased shear deformation at small L/d-ratios leading to increased effective stresses, not respected in general beam theory. In general, the moduli from 4-point, 3-point and tensile test are all similar. The modulus of the compression side from 4-point bending is about 65 GPa, too. It can be stated, independently of the test method, that the Young's modulus of C/C-SiC in 0/90° direction is about 65 GPa under tensile and compression loading. Because of the non-linear behaviour of C/C-SiC the Young's modulus has always to be considered in dependency of the evaluated stress regime (here 10-30 MPa). A reduced Young's

modulus of about 60 GPa for the 0/90° direction is usually used for FE-modelling due to the non-linearity of the stress-strain behaviour.

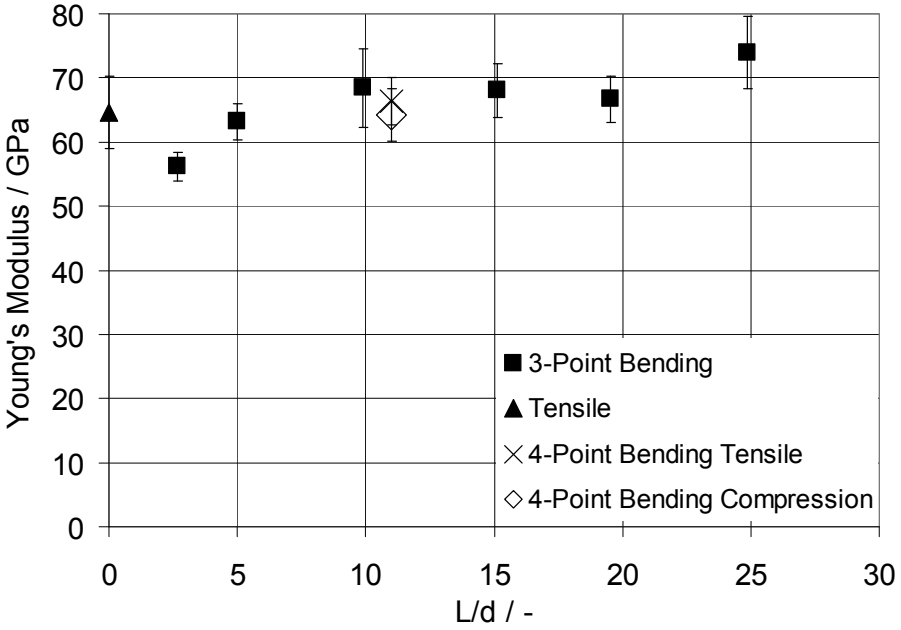

Figure 13: Young's modulus evaluated from strain gauge measurements under bending and tensile load for the siliconized plate PH1991_ND.

Figure 14 a shows the theoretical bending strength values at varying L/d-ratios and the corresponding maximum shear stresses. The same trend is observed as for the Young's modulus in Figure 13: the calculated bending strength is slightly reduced with decreasing L/d-ratio. The explanation is identical. The 3-point bending strength at L/d=10 is about 210 MPa. It is only slightly higher than the 4-point bending strength at a comparable L/d-ratio, which shows that the loaded volume does not have a significant impact on the strength of C/C-SiC. Typical Weibull materials show a significantly lower strength in 4-point bending.

The bending-tensile strength ratio is 1.71 considering the 4-point bending strength. Compression or shear failure was not observed in any of the samples, although, high interlaminar shear stresses up to 36 MPa were reached for very low L/d-ratios. The maximum interlaminar shear stress τ_{max} was calculated following the equation:

$$\tau_{max} = \frac{3}{4}\frac{F}{bd} \qquad \textbf{(5)}$$

The strain at maximum load was defined as failure strain. Figure 14 b shows that the bending failure strain is about 4 o/oo for all L/d-ratios. In contrast to the theoretical Young's moduli and bending stresses, the failure strains are independent of the L/d-ratio. This proofs the explanation from above: due to shear deformation the actual tensile stresses are underestimated by beam theory for low L/d-ratios. The failure

strain from tensile testing is about 2.4 o/oo. The ratio of 4-point bending to tensile failure strain is 1.55 which is slightly lower than the ratio of 4-point bending to tensile strength (1.71).

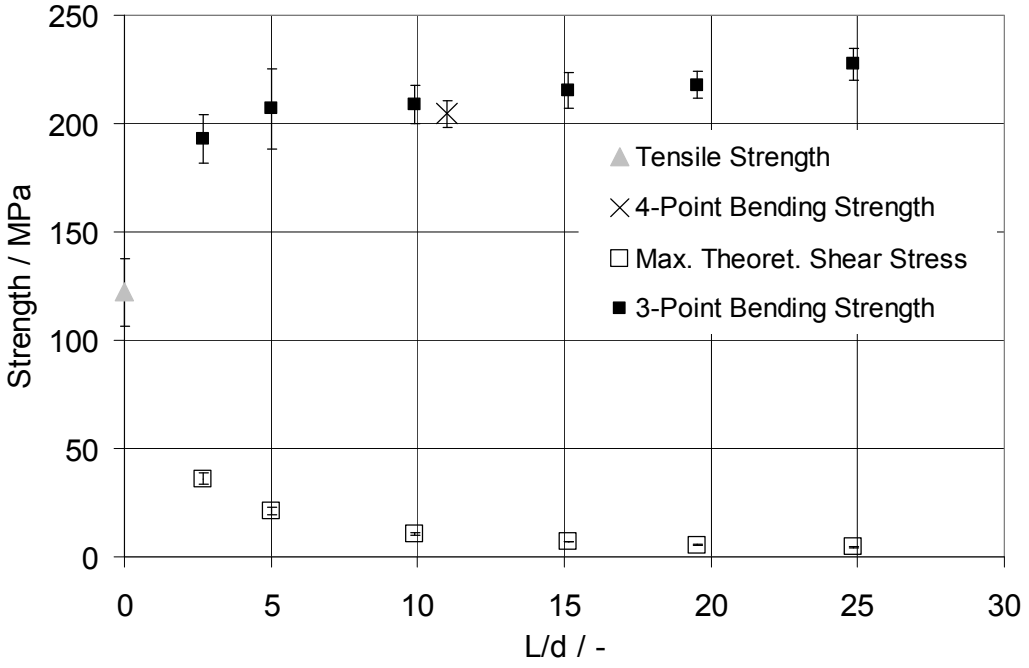

a)

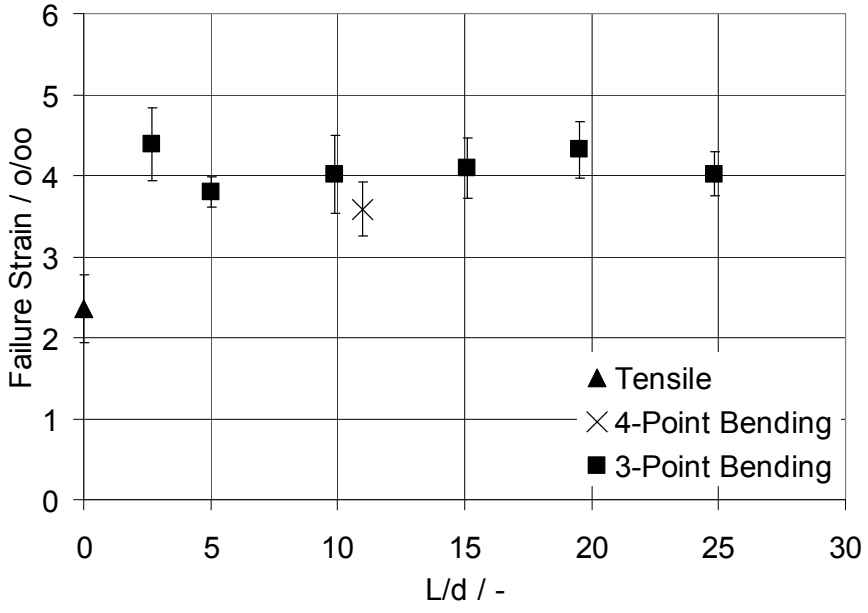

b)

Figure 14: Tensile, bending strength, respective shear stresses (a) and failure strains (b) at varying L/d-ratios from plate PH1991_ND in siliconized state.

Figure 15 shows a comparison of the mechanical properties in siliconized and desiliconized state of plate PH1991_ND. The Young's moduli from 4-point, 3-point and tensile testing are at the same level in both states. Although, the stiffness remains

constant the strength is reduced by about 20-40 MPa due to desiliconization, see Figure 15 b. The porosity, measured by Archimedes method, increased from 1.3% to 5% after desiliconization. The 4-point bending-tensile strength ratio is slightly increased to 1.78 in comparison to 1.71 for the siliconized state.

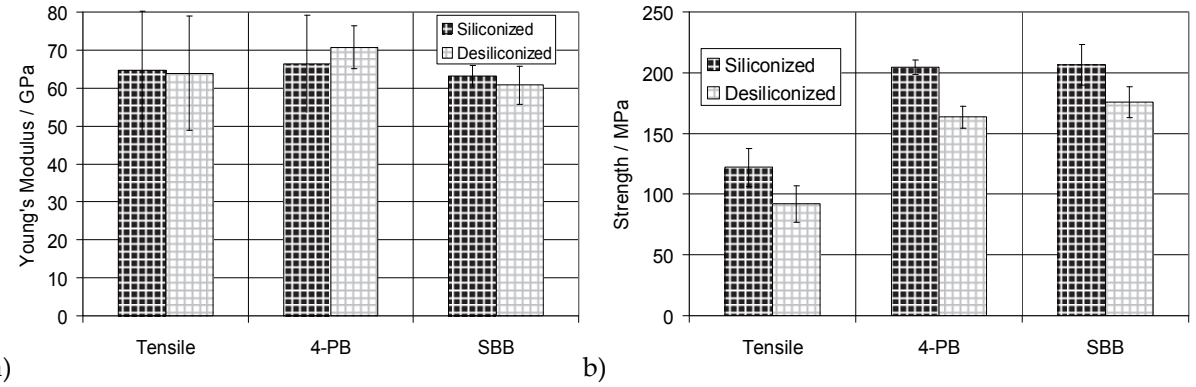

Figure 15: Comparison of Young's modulus (a) and strength (b) for siliconized and desiliconized C/C-SiC from tensile, 4-point and short-beam bending test (L/d=5) of plate PH1991_ND.

Finally, the short-beam bending test (L/d=5) was used to evaluate the interlaminar shear modulus G of siliconized and desiliconized material. The evaluation follows beam theory [40][41] and the assumption that the total displacement of the beam is the sum of deformation due to bending moment u_M and shear stresses u_s:

$$u_{total} = u_M + u_s \quad \textbf{(6)}$$

$$u_M = \frac{F}{4Eb}\left(L/d\right)^3 \quad \textbf{(7)}$$

$$u_s = \frac{\gamma L}{2} \quad \textbf{(8)}$$

with shear strain $\gamma=\tau/G$ and the average shear stress τ:

$$\tau = \frac{F}{2bd\,5/6} \quad \textbf{(9)}$$

The correction factor for rectangular cross-sections of 5/6 was introduced by Timoshenko [41] in order to consider the reduced effective shear area due to the actual parabolic shear stress distribution. The deformation due to shear stresses is therefore:

$$u_s = \frac{FL}{bdG\frac{20}{6}} \quad \textbf{(10)}$$

The interlaminar shear modulus G is then:

$$G = \frac{1}{\frac{20}{6} bd\left(\frac{u_{total}}{FL} - \frac{L^2}{4Ebd^3}\right)} \quad \textbf{(11)}$$

Considering the strain gauge measurement ε on the tensile side and by using $E=\sigma_b/\varepsilon$ for the Young's modulus with equation (4) the interlaminar shear modulus can be determined directly from the total displacement and the strain gauge measurement for any load point:

$$G = \frac{FL}{\frac{20}{6} bd\left(u_{total} - \frac{\varepsilon L^2}{6d}\right)} \quad \textbf{(12)}$$

As shown above, the Young's modulus is slightly underestimated for low L/d-ratios. Therefore the evaluation of interlaminar shear modulus from short-beam bending test is slightly overestimating the true value. Nevertheless the L/d-ratio of 5 was chosen to evaluate the interlaminar shear modulus because only for low L/d-ratios the shear deformation is detectable at all. Figure 16 a is showing exemplarily the stress-strain curves evaluated for one short-beam bending sample of desiliconized PH1991_ND material. As explained above the shear modulus is calculated from the difference in strain of the two curves. The bending stresses σ_b in Figure 16 a were calculated following equation (4). The strains from total deflection ε_{total} were estimated following the equation (7) and (4) from general beam theory:

$$\epsilon_{total} = u_{total} \frac{6d}{L^2} \quad \textbf{(13)}$$

Figure 16 b is showing the evaluated Young's modulus, E, and interlaminar shear modulus, G, of the respective curves. The tangential Young's modulus is about 70 GPa for very low bending stresses and decreases to 50 GPa for stresses close to failure. Because of the displacement offset the shear modulus curve goes to infinity at low stress values, compare Figure 16 b. Those values are not to be considered, that is why the shear modulus was evaluated at 50 MPa of bending stress. For higher stress values the calculated interlaminar shear modulus is slightly increasing because the Young's modulus is decreasing. Figure 17 shows the average interlaminar shear moduli from siliconized and desiliconized C/C-SiC. In contrast to the Young's moduli, see Figure 15 a, the interlaminar shear modulus of desiliconized C/C-SiC is clearly reduced in comparison to the siliconized material.

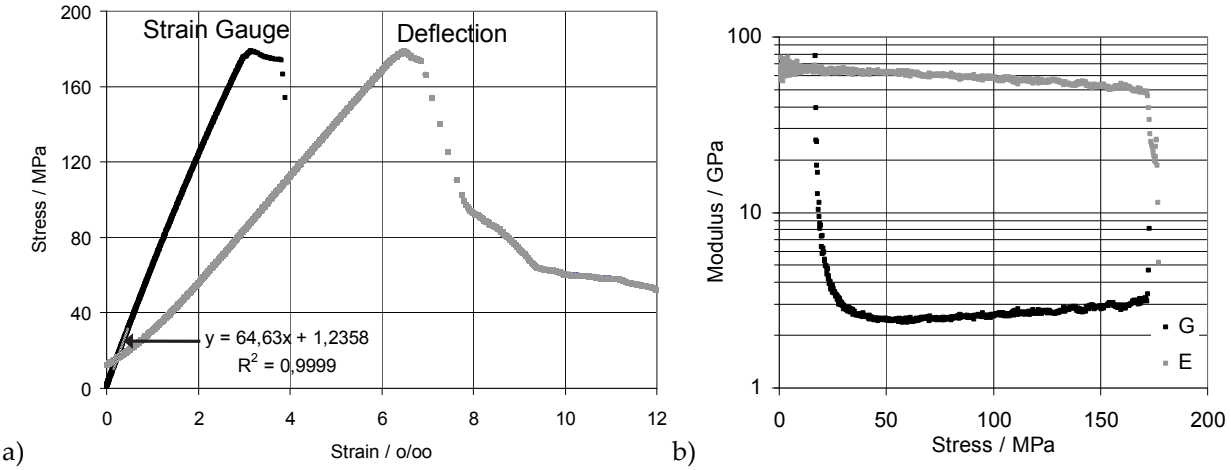

Figure 16: Exemplary stress-strain curves evaluated from total deflection and from strain gauge measurement (a), corresponding tangential E-modulus and interlam. shear modulus G (b) from PH1991_ND in desiliconized state.

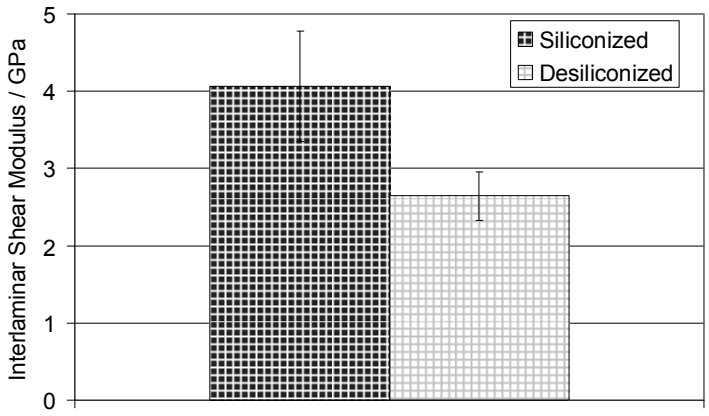

Figure 17: Interlaminar shear moduli evaluated from short-beam bending of siliconized and desiliconized samples of PH1991_ND.

6.1.2 *Tensile and bending tests in varying orientations*

The results from mechanical testing in varying orientations relative to the 0/90° fibre reinforcement are summarized in the following. Figure 18 shows the load-deflection recorded in different directions during 3-point bending test (L/d=20.9). The stiffness decreases with increasing angle between fibre and loading direction as expected. The load-displacement response in 0° and 15° is almost linear, in contrast the 30° and 45° directions show strong non-linear behaviour. All curves show a steep load drop after reaching failure load, indicating rather brittle failure. The sample surfaces showed directly after failure a crack through at least 30% of the sample thickness. It was not possible to stop the testing machine at the load maximum or to drive slowly enough

to see single ply failure. All of the bending samples failed by tensile failure at the lower side of the sample. Shear or compression failure was not observed. Interesting enough: the load drop observed in long beam bending is much more pronounced as in short-beam bending, see Figure 16 a. It is common for CMCs, as mentioned by Fink [14], that larger loaded volumes show increased brittle failure. The brittle failure is indicated here by the load drop after reaching ultimate load.

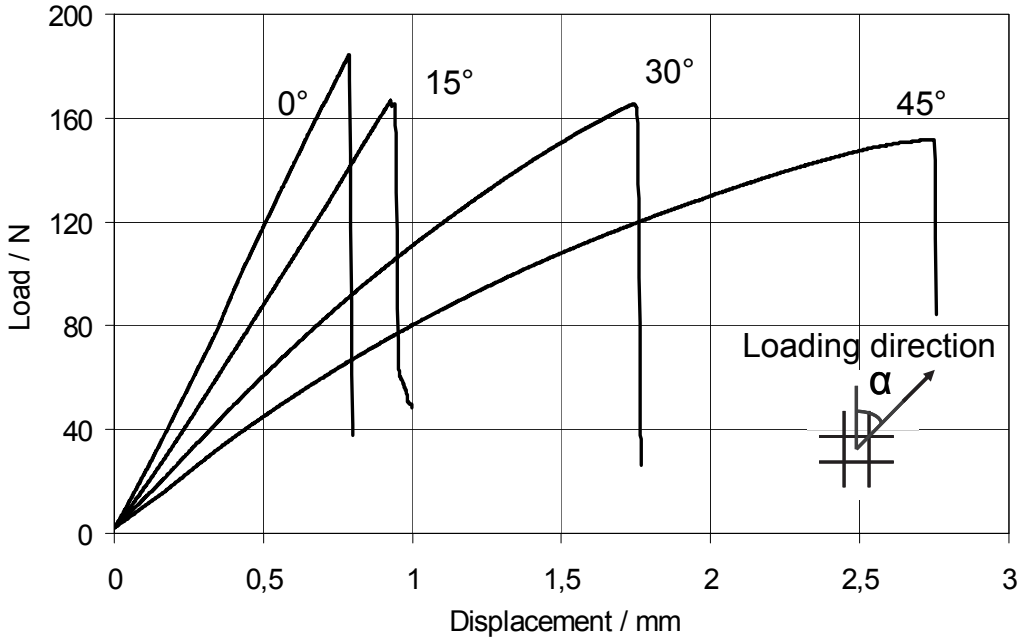

Figure 18: Load-displacement behaviour from 3-point bending tests (L/d = 20.9) in varying directions from plate PH2035_ND in siliconized state.

The stress-strain curves from tensile and bending test in different orientations relative to the 0/90° fabric are compared in Figure 19 a. There are mainly three significant results: first of all, the tensile strength lies in all directions about 100 MPa below the respective bending strength. Further the elastic behaviour from tensile and bending test is similar. And finally, the non-linearity observed in tensile testing is more distinctive leading to failure at only about half of the bending failure strain. The strain measurements on the 4-point bending samples revealed that the stress-strain behaviour on the compression side is less non-linear compared to the strongly non-linear behaviour under tension (Figure 19 b). This becomes very clear in the 45° loading direction. The stiffness under compression and tensile load are comparable but only for a low stress regime up to 20 MPa for 45°. The tensile and compression curves are similar up to 50 MPa for 0°.

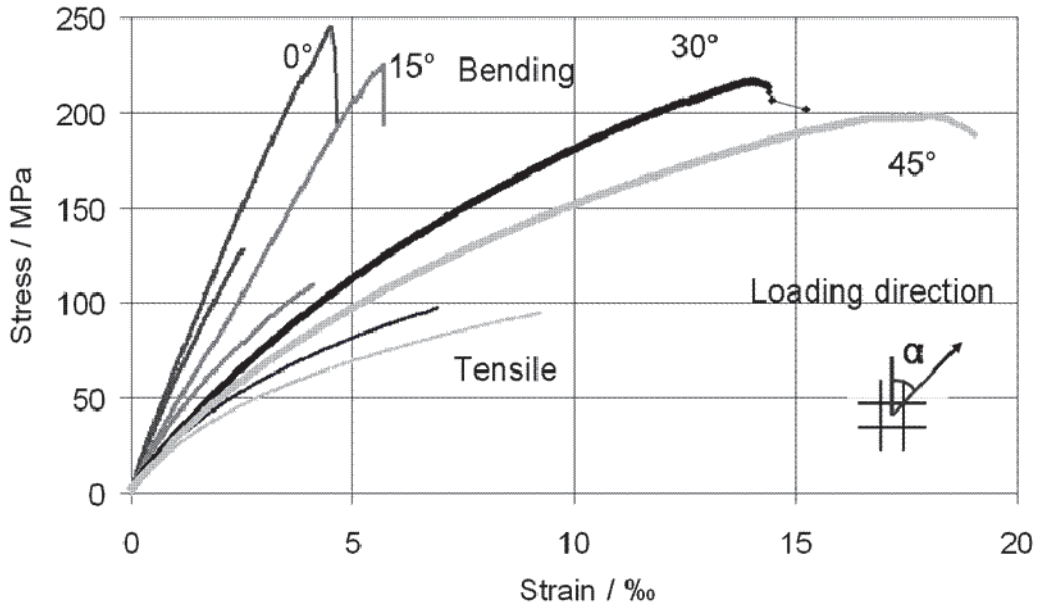

a)

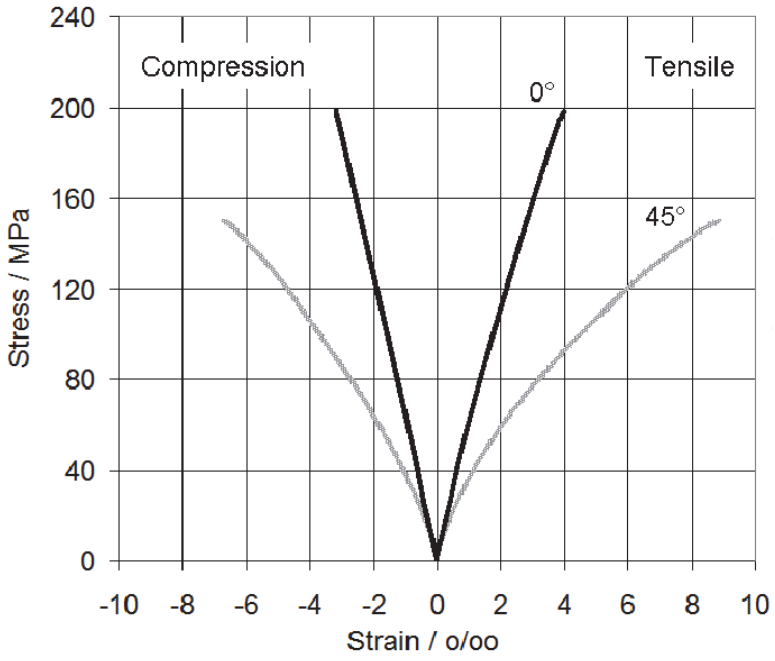

b)

Figure 19: Stress-strain behaviour from tensile test, 3- (a) and 4-point bending (b) in different orientations. Bending stresses were calculated assuming beam theory.

The differences in stress-strain behaviour under tensile and compression load (Figure 19 b) were confirmed by compression test results published by Fink [14]. The results in Figure 19 b and the results from Fink [14] show that classical beam theory cannot be applied to calculate accurately the tensile and compressive stresses in the bending sample. The comparison of theoretical stress-strain curves under tensile and bending load in Figure 19 a shows that the linear elastic compression side supports the non-linear tensile side and leads to decreased stress and strain values at the lower tensile

side. This becomes most clear for the 45° bending stress-strain curve: tensile failure strain is reached at a theoretical bending stress of about 150 MPa. The tensile failure strain is reached at about 100 MPa in tensile loading. This behaviour shows that the apparent stress at the tensile side of the bending sample must be about one third lower than the theoretical stress value in 45° direction. Just by comparing the failure strains in Figure 19 a it can be demonstrated that the theoretical bending to tensile strength ratio must be at least 1.5 for 45° and about 1.15 for 0° direction. Nevertheless, the difference of bending to tensile strength cannot be explained solely by the differing stress-strain behaviour. That is why additionally the effect of crack propagation under bending load was investigated by SENB testing.

6.1.3 *SENB testing*

The in-plane SENB tests showed similar load-displacement behaviour for the 0/90° and 45° orientations, see Figure 20. The curves show linear behaviour up to failure load followed by a small load drop and a section of stable crack propagation. A much stronger load drop was observed during bending tests (Figure 18). In contrast to the bending tests the behaviour of the 45° SENB test is almost linear elastic and the stiffness is similar to the 0/90° orientation. This indicates that the chosen test set-up is well suited to suppress non-linear effects in 45° orientation. On the other hand it shows, that shear deformation is influencing the overall stiffness leading to increased stiffness of the 45° orientation relative to the 0/90° samples.

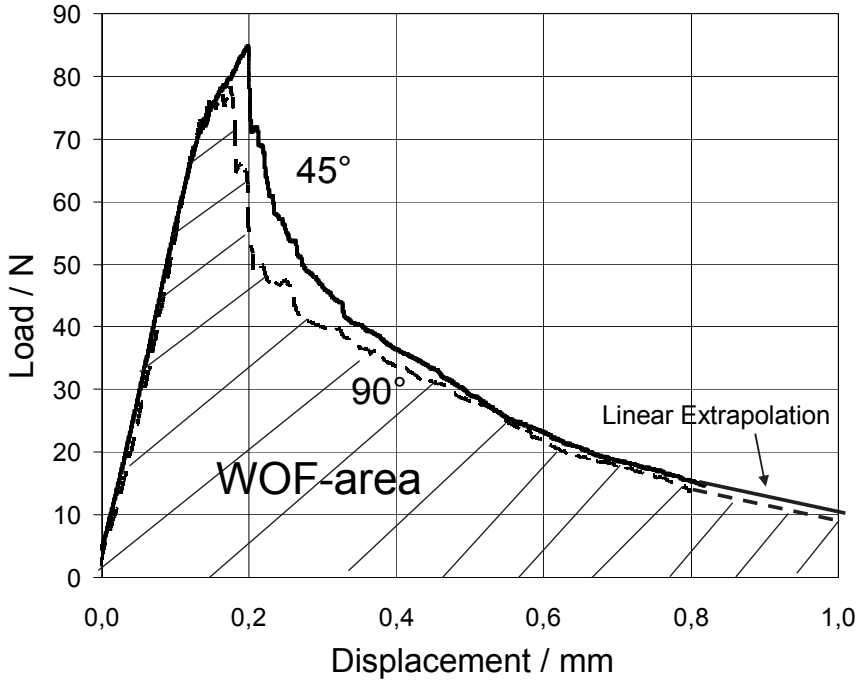

Figure 20: Load-displacement from SENB in 0/90° and 45° direction with an initial relative crack length of a/W = 0.41.

The SENB tests were evaluated regarding the K_{Ic} value and the WOF-area (Figure 20). The equations from Tada et al. [38] were used to determine the K_{Ic} values from the maximum load:

$$K_{Ic} = \sigma_b \sqrt{\pi a}\, F(a/W) \tag{14}$$

with initial crack length a, height of SENB sample W and bending stress σ_b from equation (4). For L/W=4, F(a/W) is:

$$F\left(\frac{a}{W}\right) = \frac{1}{\sqrt{\pi}} \cdot \frac{1.99 - \frac{a}{W}(1 - \frac{a}{W})(2.15 - \frac{3.93a}{W} + 2.7(\frac{a}{W})^2)}{(1 + \frac{2a}{W})(1 - \frac{a}{W})^{3/2}} \tag{15}$$

The equation from Nakayama et al. [39] was used to calculate the WOF from the load-displacement curves, as shown in Figure 20:

$$WOF = \frac{\int F du}{2b(W - a)} \tag{16}$$

Figure 21 a shows that the K_{Ic} values and also the WOF determined in the different directions are almost constant. This result is confirmed by plotting the bending strength of the differently orientated SENB samples over the relative crack length in Figure 21 b. There is a good accordance with the results from LEFM calculated for an overall average K_{Ic} value of 5.4 MPa $m^{1/2}$.

The results from translaminar SENB test from pre-notched and pre-cracked samples agree both with the curve from LEFM. In that way it was confirmed that the notches introduced by abrasive cutting are comparable to sharp pre-cracks. All other results were obtained with pre-notched samples.

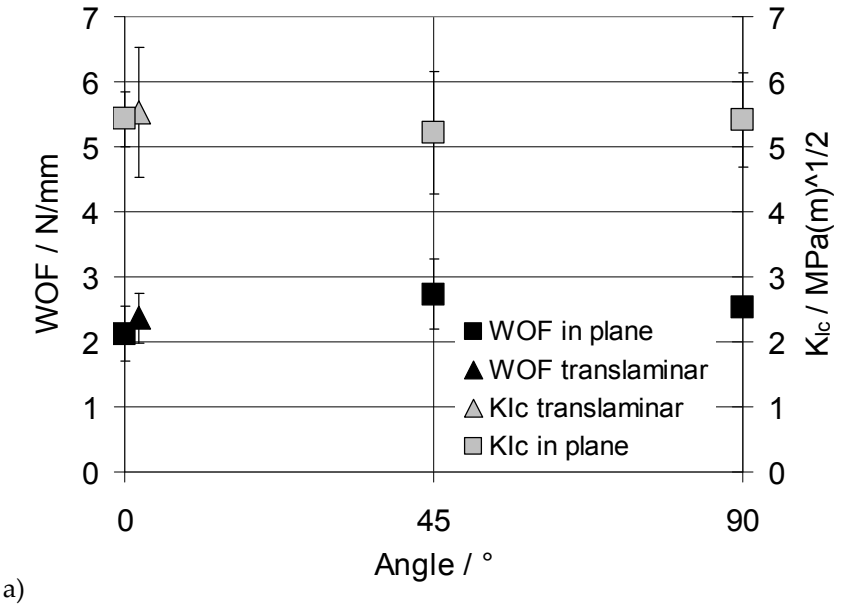

a)

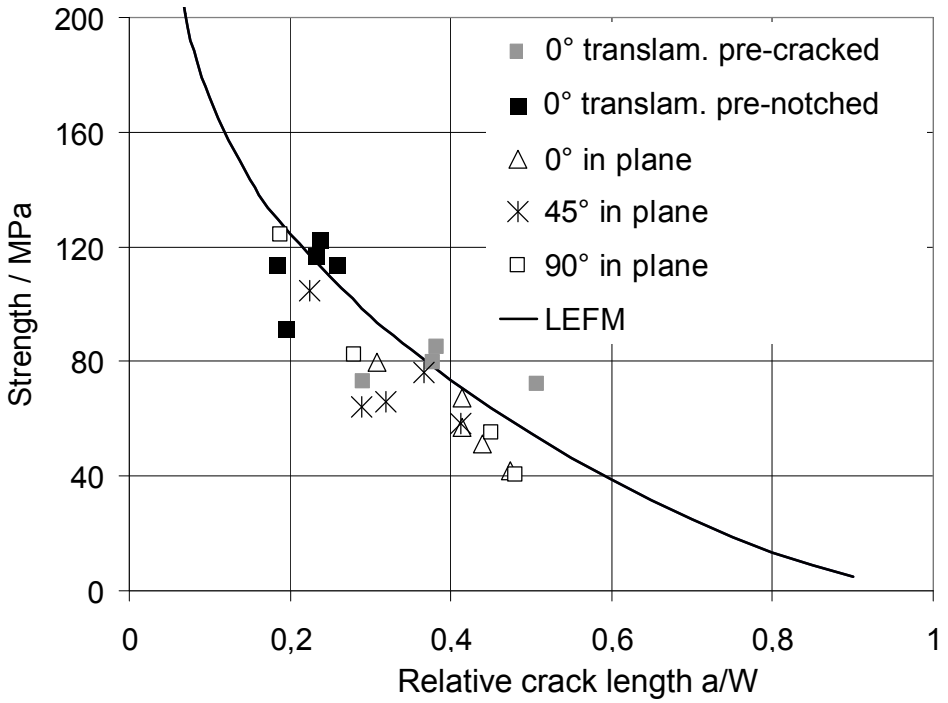

b)

Figure 21: WOF and K_{Ic} values measured in SENB test in different orientations (a), bending strength from LEFM and SENB tests (b).

6.1.4 *Interlaminar test results*

This chapter is summarizing the experimental results from desiliconized PH1991_ND C/C-SiC material in DCB and ENF testing. The test results were evaluated in regard of

stiffness, critical energy release rates and crack propagation curves in comparison with analytical solutions from LEFM. The investigations of interlaminar fracture of C/C-SiC are focusing on the desiliconized state because it was shown in chapter 5.2 that delaminations appear mainly after desiliconization in C/C-SiC.

6.1.4.1 Mode I: DCB

First, the stiffness of the six DCB-samples with varying initial crack lengths was evaluated. An effective Young's modulus was evaluated from the linear part of the load-deflection curves following beam theory as cited by Allix et al. [37]:

$$E = \frac{dF}{du} \cdot \frac{2a^3}{3I} \qquad \textbf{(17)}$$

with a, initial crack length, and I, geometrical moment of inertia of one cantilever beam:

$$I = b\left(\frac{h}{2}\right)^3 /12 \qquad \textbf{(18)}$$

b is the width, h is the height of the sample. The average effective modulus was determined to be 24.5 +/- 4.5 GPa. Figure 22 shows the width-normalized stiffness from experiment and theoretical curves for the effective modulus of 24.5 GPa and for a tensile modulus of 58 GPa, which was used for FE-modelling. Due to interlaminar shear deformations, the stiffness is by far overestimated for the effective Young's modulus of 58 GPa.

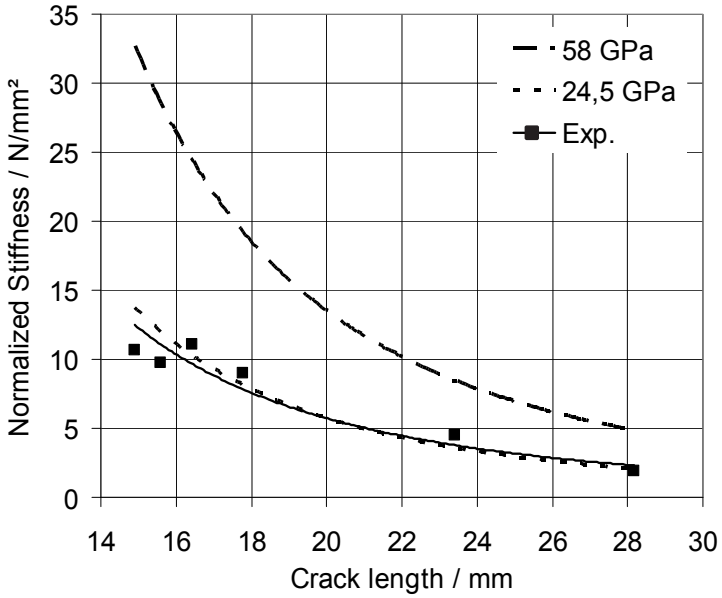

Figure 22: Width-normalized stiffness in dependency of initial crack length: results from LEFM [37], equation (17), for different Young's moduli and experimental data with exponential regression curve.

Since the crack initiation could not be clearly resolved by the images taken with the GOM/ARAMIS camera, the 5%-offset method was used to determine the load at crack initiation. Figure 23 shows the normalized load-deflection curves of four selected samples with varying initial crack lengths and the 5%-reduced stiffness lines for the determination of initiation load. The samples 8, 9 and 12 reached full delamination over the complete sample length. The interlaminar crack started to run upwards leading to bending failure of the upper cantilever arm for all other samples. Overall six samples were tested in DCB set-up. All load deflection curves in Figure 23 show a first kink below 1 N/mm of width-normalized load. The kink is possibly caused by the alignment of the test set-up.

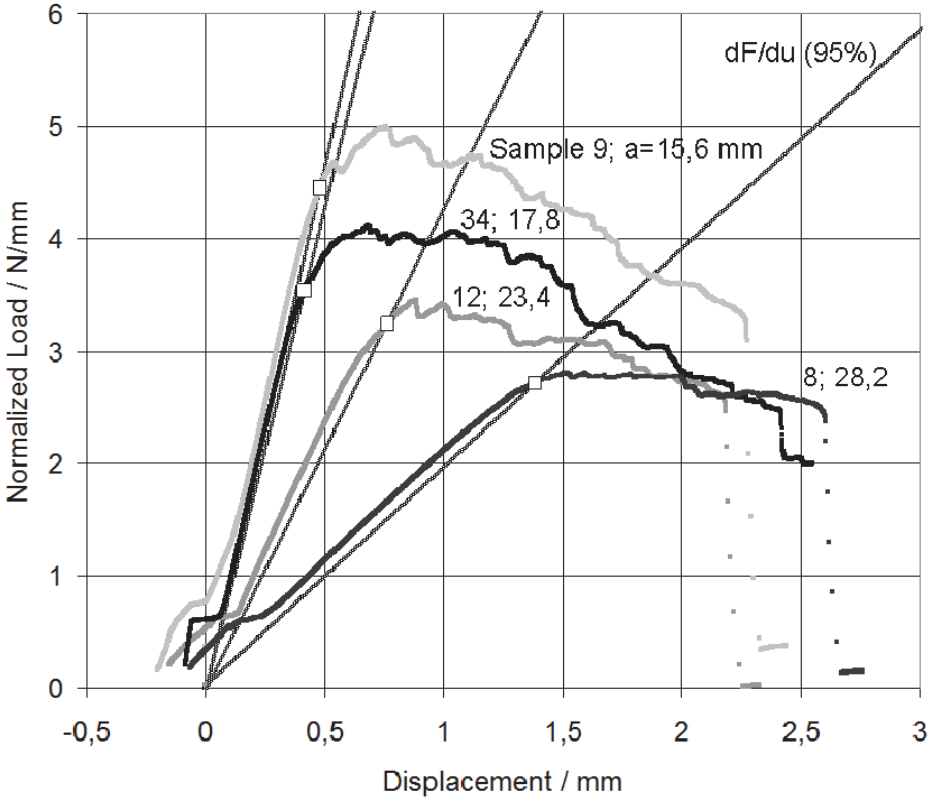

Figure 23: **Normalized load-deflection curves from DCB test, 95%-slopes and critical load points. The sample numbers and initial crack lengths are indicated.**

Different methods were applied to calculate the G_{Ic} values for crack initiation from 5%-offset loads:

First the beam theory was used [33]:

$$G_{Ic} = \frac{3Fu}{2ba} \tag{19}$$

The average G_{Ic} was determined to be:

G_{Ic} = 0.180 +/-0.032 N/mm

This value is overestimating the G_{Ic}, as described in ASTM standard, since the beam is in practice not perfectly built in, i.e. clamped at the delamination front, and so rotation may occur at the delamination front. This can be corrected by considering a slightly longer delamination a + Δ, where delta may be determined by plotting the compliance $C^{1/3}$ over the crack length a. In Figure 24 the compliance $C^{1/3}$ is plotted over the respective initial crack length of all investigated samples. The average delta, that is the intersection point with the x-axis, was determined to be 1.98 mm. The stiffening of the loading blocks has to be corrected, following ASTM standard [33], if the distance

between load line and delamination front is less than 50 mm. This was the case for all samples so the compliance was corrected by C/N and N was calculated following the equation:

$$N = 1 - \left(\frac{L'}{a}\right)^3 - \frac{9}{8}\left(1 - \left(\frac{L'}{a}\right)^2\right)\left(\frac{ut}{a^2}\right) - \frac{9}{35}\left(\frac{u}{a^2}\right) \quad \textbf{(20)}$$

L' and t are described in Figure 9, u is the total load point deflection.

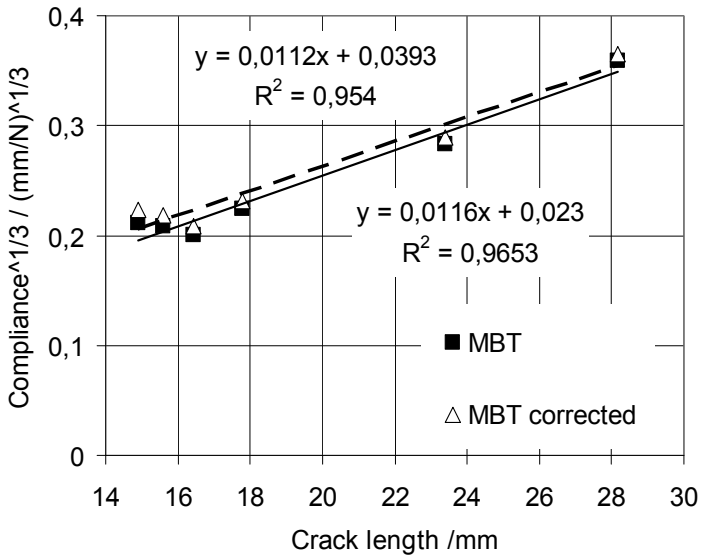

Figure 24: Determination of delta for Modified Beam Theory, MBT, following ASTM standard with and without loading block correction.

The loading block corrected delta was determined to be 2.2 mm. G_{Ic} was calculated following Modified Beam Theory (MBT):

$$G_{Ic} = \frac{3Fu}{2b(a + |\Delta|)} \quad \textbf{(21)}$$

The average G_{Ic} without loading block correction was determined to be:

G_{Ic} = 0.163+/- 0.029 N/mm. The average G_{Ic} from loading block corrected MBT is:

G_{Ic} = 0.174 +/- 0.032 N/mm.

Since the impact of loading block correction on G_{Ic} was rather low and the FE results in chapter 6.3, Figure 50, did also not show a distinctive influence of loading blocks, the consequent evaluations were focusing on MBT without loading block corrections. Figure 25 a shows the G_{Ic} values in dependency of total initial crack length. Figure 25 b shows the G_{Ic} values plotted over the sharp initial crack length, which is the total crack length minus the sawed crack length, compare Figure 9. There is no clear trend between crack length and initiation fracture toughness, neither for the total crack

length nor for the sharp crack length. However, it has to be considered here that the sharp crack length was only varying from 1-6 mm and therewith the impact of crack length on initiation fracture toughness might not have become noticeable.

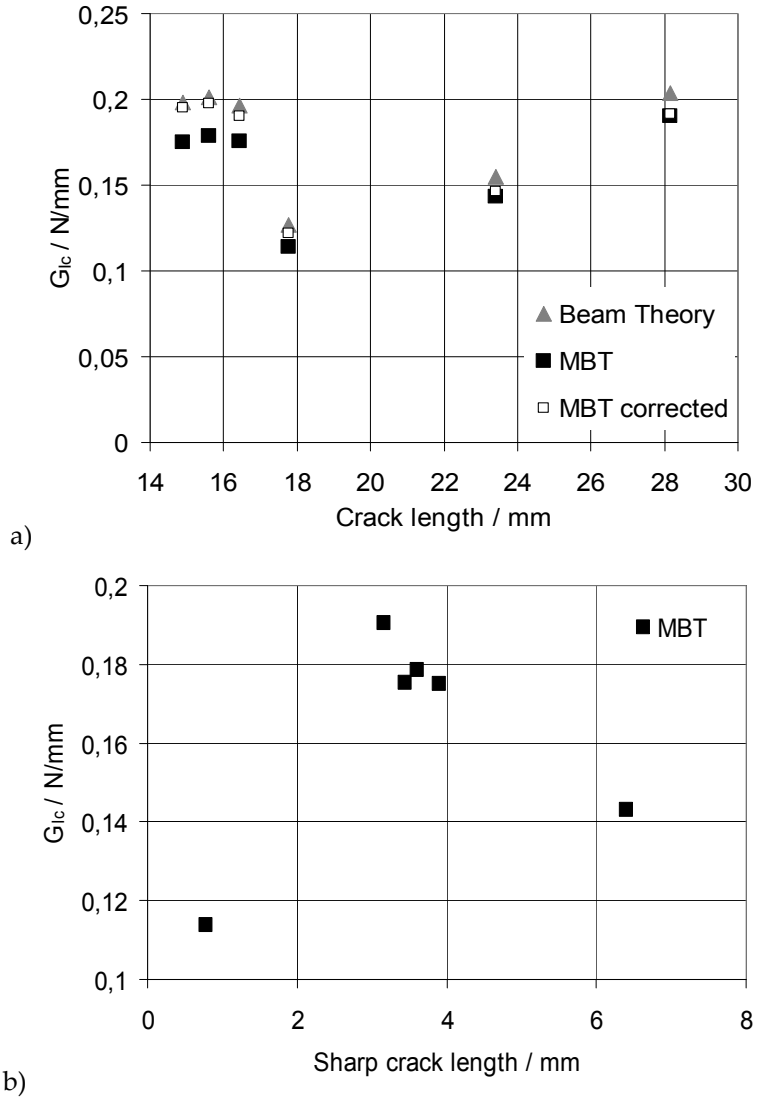

Figure 25: G_{Ic} values for crack initiation in dependency of total initial crack length (a) and sharp crack length (b). MBT values were computed from average delta values, 1.98 and 2.2 mm respectively.

Figure 26 shows the R-curves, that is the fracture toughness in dependency of the propagation crack length. The propagation crack length was determined with the help of optical strain evaluations, compare Figure 29.

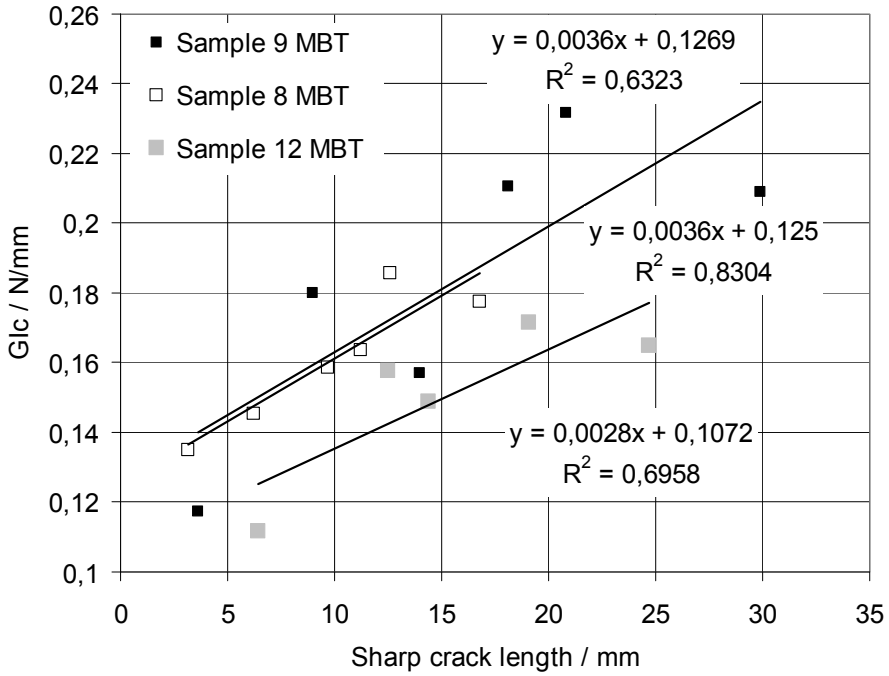

Figure 26: Exemplary R-curves for three samples following MBT without loading block corrections.

All samples in Figure 26 show a clear increase of fracture toughness with crack length. The slopes are similar. The evaluation followed MBT without loading block corrections. The delta values were determined for each sample separately.

The average inititation G_{Ic} value of 0.16 N/mm from MBT was finally used for the determination of the crack propagation curves with Young's moduli of 24.5 and 58 GPa in Figure 27. The propagation curves were determined following LEFM [37]:

$$u = \frac{(bG_{Ic})^{3/2}\sqrt{EI}}{3F^2} \qquad \textbf{(22)}$$

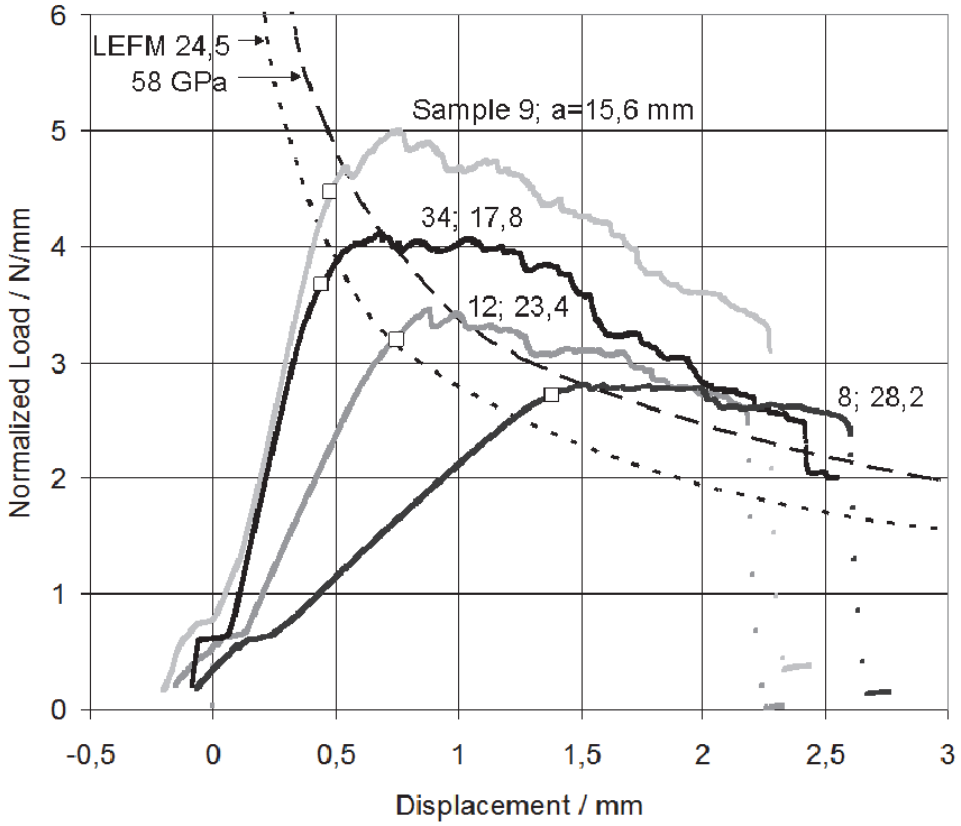

Figure 27: Crack propagation curves from LEFM for G_{Ic} = 0.16 N/mm and varying Young's moduli in comparison with experimental load-deflection data.

Figure 27 shows that the initiation of crack growth can be described by LEFM with an effective modulus of 24.5 GPa and an average G_{Ic} of 0.16 N/mm. Nevertheless, the experimental crack propagation curves do not follow the distinct load decrease from LEFM. In contrast, the experimental curves show a load plateau after crack initiation. That means, the C/C-SiC material is indicating an increase of propagation fracture toughness with increasing crack length as also shown by the R-curves in Figure 26.

The average inititation G_{Ic} of 0.16 N/mm from MBT without loading block corrections was used for the LEFM calculations and for the numerical investigation in chapter 6.2.2.1 because it was found to be a reasonable average value for the initiation and propagation fracture toughness of desiliconized C/C-SiC, see Figure 26. Finally, the Airbus Industry Testing Method [34] was applied to the samples 8, 9 and 12, which reached total delamination. The Airbus standard is an area method. The determination of initiation G_{Ic} and R-curves is not possible. The following equation was used:

$$G_{Ic} = \frac{A}{b a_p} \tag{23}$$

A is the integrated area, see Figure 28, b is the width of the specimen and a_p is the propagation crack length (final crack length - initial crack length). The average G_{Ic} from AITM standard was calculated to be 0.167+/-0.040 N/mm. Figure 29 shows the images and optical strain measurements of sample 9 at varying load points. The optical strain measurements are only of qualitative interest to detect the current crack length. The quantitative values are not reliable. It is hardly possible to detect the crack length at the grey scale images of Figure 29. The optical strain measurements, however, indicate the crack position roughly at the right end of the high strain areas. The first crack propagation for sample 9 was observed between load point 2 and 3 which is at slightly higher load than determined by 5%-offset method, i.e. 51.1 N at load point 2 in Figure 28. This corresponds to ASTM standard [33]: for tough matrix composites non-linear behaviour can occur before visual crack propagation is observed. In general the observation of crack propagation in C/C-SiC material is difficult and it is assumed that the first very fine interlaminar cracks could not be visually detected. Crack observation under load with light microscopy is highly recommended.

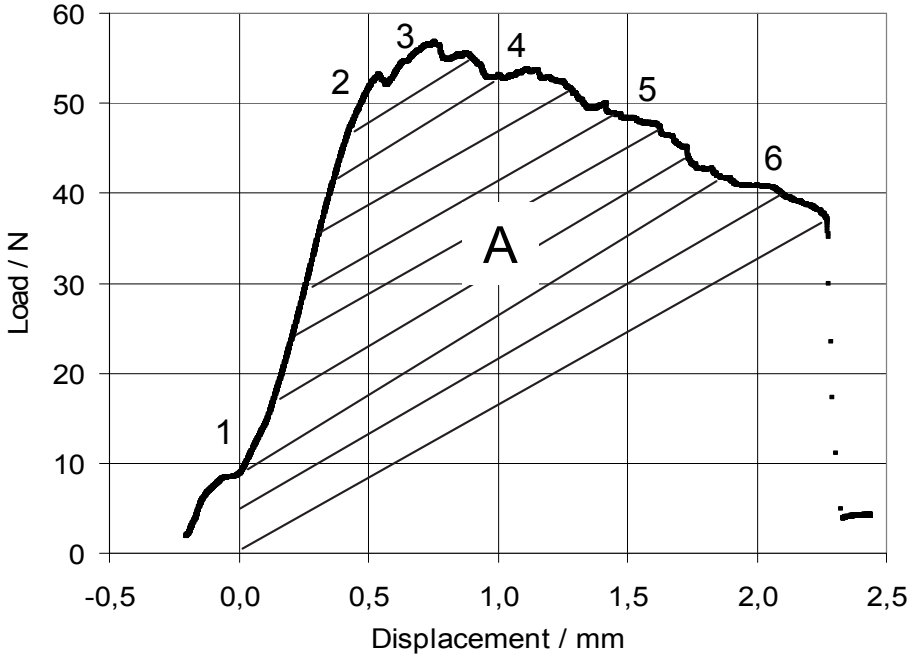

Figure 28: Load-deflection curve of sample 9 with integrated area defined as energy to achieve the total propagated crack length; numbers 1-6 refer to Figure 29.

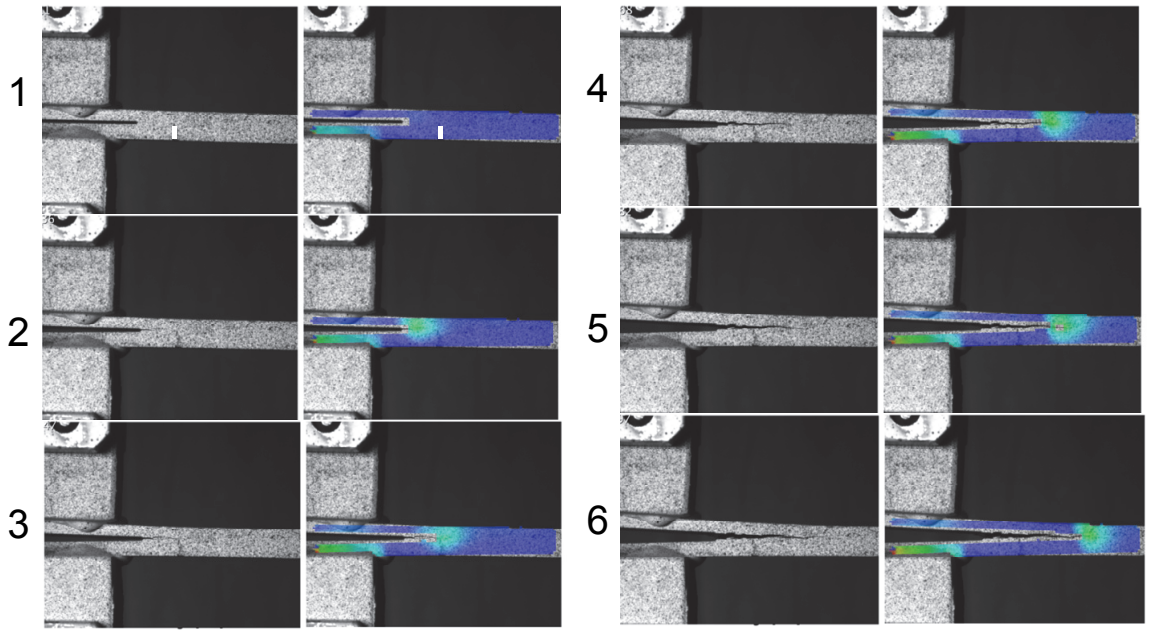

Figure 29: Grey scale images and qualitative interlaminar strain distribution at load steps 1-6, related to Figure 28. The initial crack length is marked as white bar in image 1.

6.1.4.2 Mode II: ENF

Samples for 3-point bending and ENF testing were cut from plate PH1991_ND after desiliconization. A part of the samples was tested without pre-cracking in a corresponding 3-point bending set-up with L/d=10. The 3-point bending strength was measured to be 140.3 +/- 6.5 MPa. The effective modulus, determined from deflection with equations (4) and (7), was 43.4 +/- 4.7 GPa in average. Six samples of plate PH1991_ND were tested in ENF set-up. Two samples had to be rejected: the artifical pre-crack in sample 2 had an offset to the upper bound; the crack in sample 5 changed significantly the crack plane during propagation. Finally, the G_{IIc} was evaluated from four samples: 3, 4, 6 and 7. First the stiffness S of the pre-cracked samples was compared with the analytical solutions following Allix et al. [37] for $0 \leq a \leq L/2$:

$$S = \frac{384EI}{L^3 + 12a^3} \qquad \textbf{(24)}$$

I is again the geometrical moment of inertia of one half beam, see equation (18). A good agreement between experimental and analytical stiffness was obtained when the effective Young's modulus of 43.4 GPa from 3-point bending with L/d=10 was used. The stiffness was overestimated using a standard Young's modulus of 58 GPa, see Figure 30.

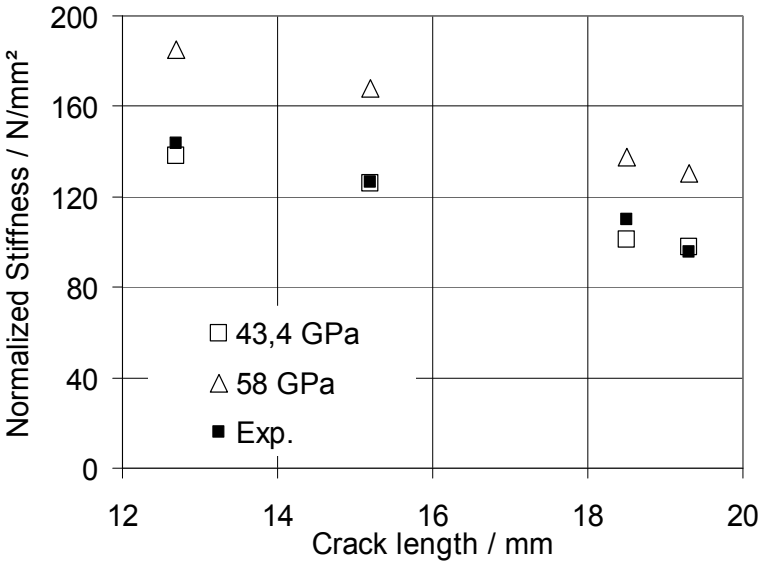

Figure 30: Normalized stiffness from LEFM and experiment in dependency of total initial crack length for ENF samples; the Young's moduli used for the LEFM computations are given.

There are different ways to determine the critical load point of crack initiation as it was also mentioned for mode I testing in chapter 4.2.2.1. The AITM standard for ENF mode II testing [35] proposes to determine the load point where crack propagation is visually observed. However, the visual detection of crack propagation is even more difficult in mode II testing than in mode I. Therefore it was attempted to use again the 5%-offset method as described in chapter 6.1.4.1. This method did also not succeed because the samples showed strong non-linear behaviour, leading to an underestimation of the critical load points. Finally the point where the load-deflection-curves showed the first strong kink was used to evaluate the initiation G_{IIc}, see Figure 31.

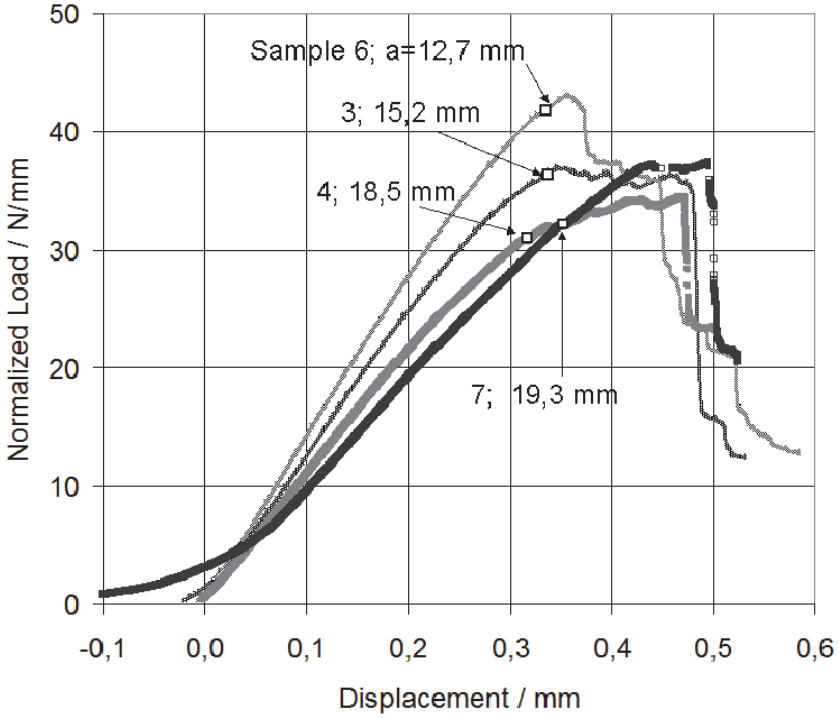

Figure 31: Width-normalized load-displacement curves from ENF-test, the critical load points for the respective sample number and initial crack length are indicated.

The final steep load drops in Figure 31 are not caused by interlaminar shear failure but by bending failure. Figure 32 shows the load-displacement curve of sample 6 and images from varying load points. First crack propagation is visually detected at 340 N, image 2, which corresponds to the first kink of the load-deflection curve. At load maximum, image 3, the shear crack propagates but also a tensile crack on the lower side is already observed. The subsequent images show progressive shear and tensile failure. Image 6 shows additional tensile failure from the interlaminar shear crack growing upwards in direction of the central load introduction. The determination of an R-curve was not possible in mode II testing. The crack length during propagation could not be resolved and shortly after shear crack propagation bending failure occurred for all specimens.

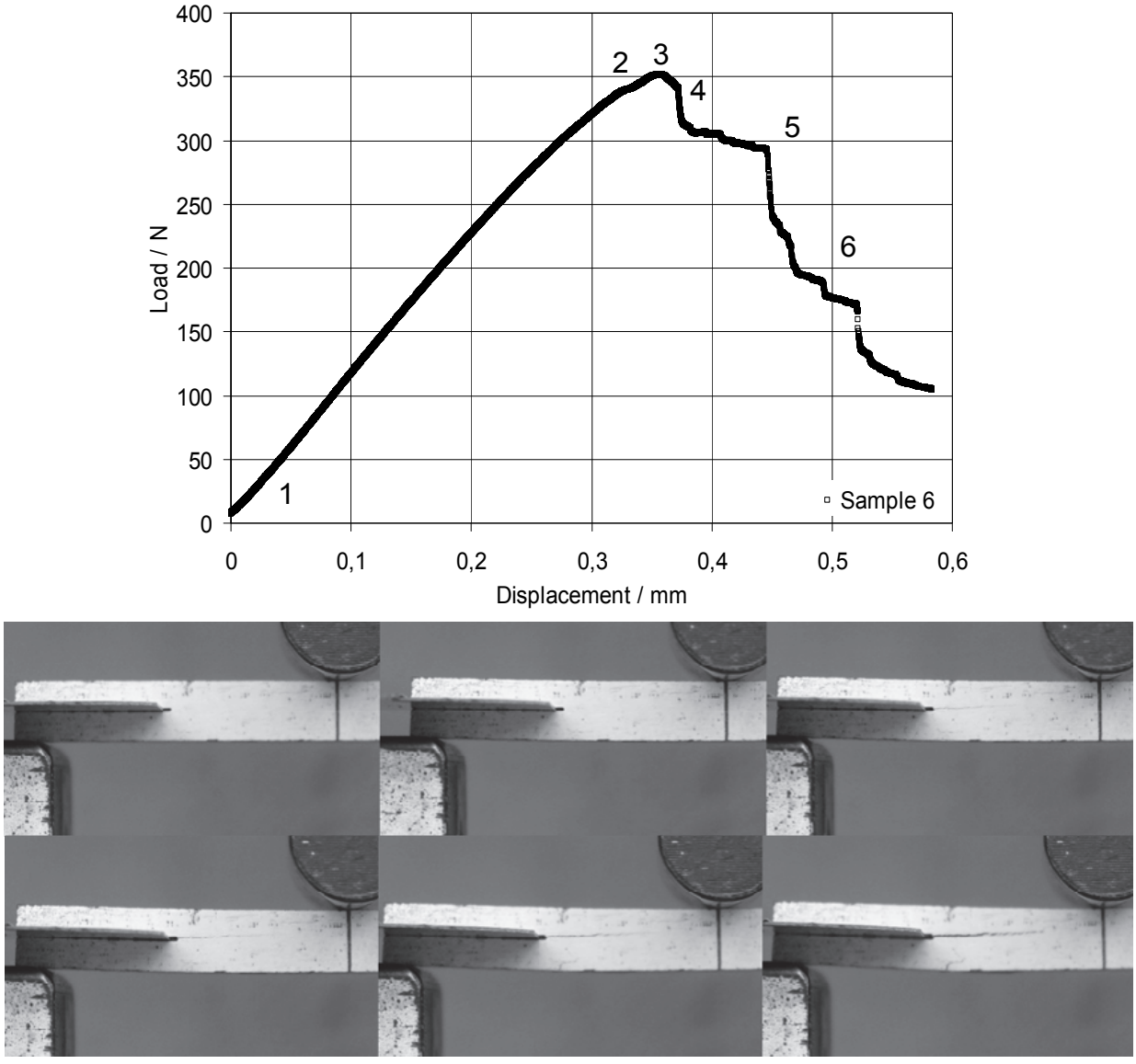

Figure 32: Load-displacement curve of sample 6 with images at varying load points (F= 5, 340, 350, 340, 300, 200 N), from left to right.

The critical load points in Figure 31 were used to calculate the initiation G_{IIc} following Szekrenyes [36]:

$$G_{IIc} = \frac{9a^2F^2}{16b^2E(\frac{h}{2})^2} \quad \textbf{(25)}$$

G_{IIC} is 0.275 +/- 0.032 N/mm in average for an effective modulus of 43.4 GPa. The average G_{IIC} is 0.21 +/- 0,02N/mm when using a typical tensile modulus of 58 GPa. Following again Szekreneyes [36] G_{IIC} can also be determined directly from the displacement at critical load without knowing the Young's modulus:

$$G_{IIc} = \frac{9a^2Fu}{2b(3a^3 + (\frac{L^3}{4}))} \quad \textbf{(26)}$$

with displacement u, crack length a, the support distance L of 50 mm and load F. The average G_{IIC} for the four valid samples was determined to be 0.31 +/- 0.04 N/mm. Figure 33 shows that the initiation G_{IIC} increases with increasing total and also sharp crack length. The sharp crack length is the total crack length minus the sawed part of the crack. The slopes in Figure 33 are roughly 3-4 times higher than in Figure 26 for the mode I fracture toughness, which shows that the increase of fracture toughness with crack length is even more pronounced under mode II loading. Since G_{IIc} is showing a strong increase with total and sharp crack length, it may be assumed that the mode II fracture toughness is more sensitive to microstructural effects, like fibre bridging or crack deflection, than G_{Ic}.

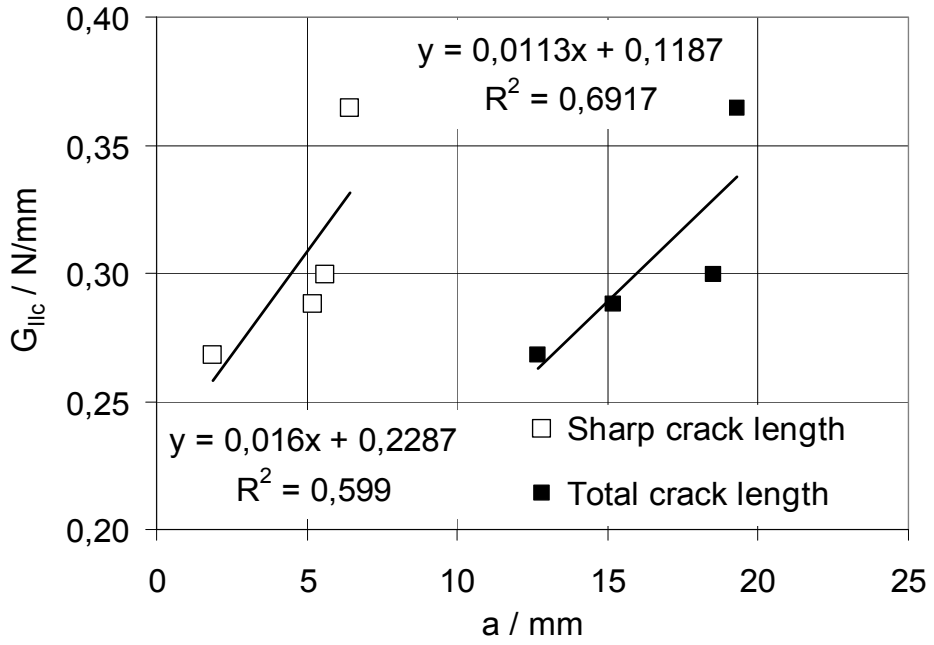

Figure 33: G_{IIc} for crack initiation in dependency of initial crack length: the sharp crack length is the total crack length minus the sawed part.

The average G_{IIC} value of 0.31 N/mm, the effective modulus of 43.4 GPa and an average height of 4.94 mm was finally used to calculate the crack propagation curve in Figure 34. The following equation from Allix et al. [37] was used:

$$u = \frac{FL^3}{384EI} + \frac{16}{F^2}\left(\frac{bG_{IIc}}{3}\right)^{3/2}\sqrt{EI} \quad \textbf{(27)}$$

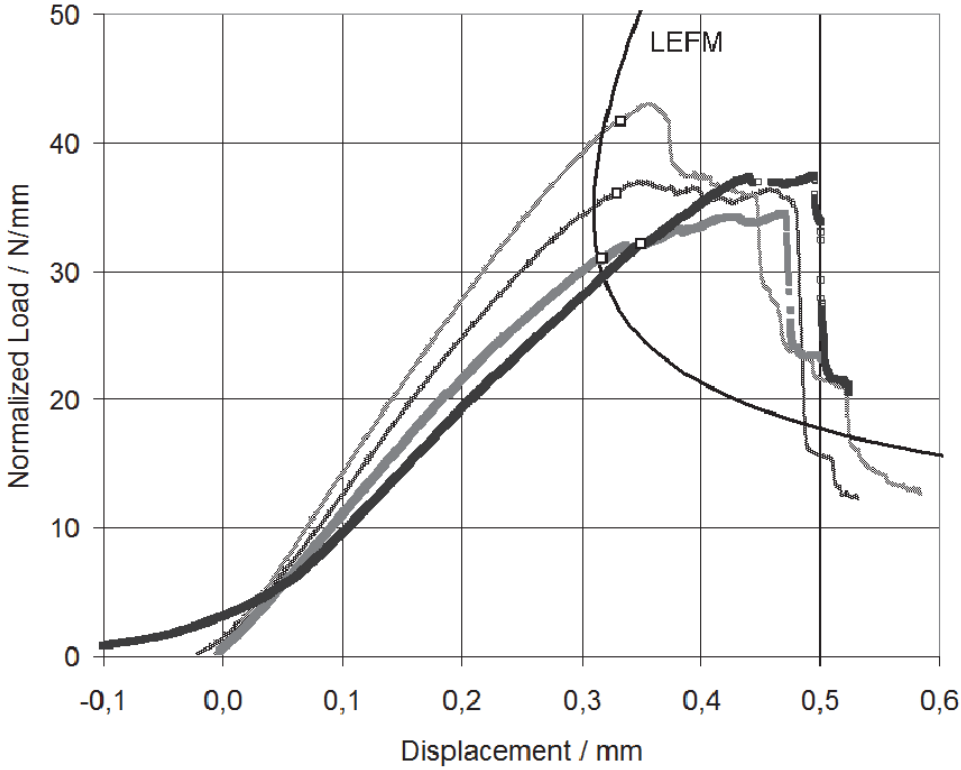

Figure 34: Load-deflection curves from ENF test, critical load points and crack propagation curve from LEFM with E = 43.4 GPa and G_{IIc} = 0.31 N/mm.

There is a good agreement of the crack propagation curve from LEFM and the interlaminar crack initiation, indicated by kinking of the experimental load-deflection curves in Figure 34. Nevertheless, the experimental curves do not show a distinctive load drop after crack initiation but even a slight increase in load, followed by a load-plateau. The final load drop is caused due to bending failure as mentioned above, see Figure 32.

The same evaluation method, as used for the samples of the desiliconized plate PH1991_ND, was also used for ENF samples of the desiliconized plate PH1879_D. The goal of the ENF tests on plate PH1879_D was to proof if similar properties compared to the standard plate PH1991_ND may be assumed for non-delaminated regions in plate PH1879_D. Therefore three samples of plate PH1879_D, which were free of interlaminar manufacturing defects after desiliconization, were chosen, pre-cracked and tested. One specimen had to be rejected because of variations in crack plane during crack propagation. The normalized load-deflection curves for the two valid samples are plotted in Figure 35. The critical load points are indicated as well as the respective initial crack lengths. The average G_{IIc} determined from the two curves, following equation (26), is 0.35 N/mm. That is slightly higher than the G_{IIc} of 0.31 N/mm from plate PH1991_ND. The calculated stiffness from equation (24), using again an effective modulus of 43.4 GPa, does neither fit to sample 10, with a crack length of 13.7 mm, nor to sample 13 with a crack length of 19.5 mm. In the first case

the theoretical slope is much higher in the second case the experimental slope is underestimated. The initial slopes of the experimental curves are almost equal which is not comprehensive. Although plate PH1991_ND showed better agreement with the predicted slopes, a similar behaviour of the samples from plate PH1879_D and the standard plate PH1991_ND was found. Taking the four samples from PH1991_ND and two samples from PH1879_D into account an overall average G_{IIc} of 0.32 +/- 0.05 N/mm was determined for desiliconized C/C-SiC following equation (27).

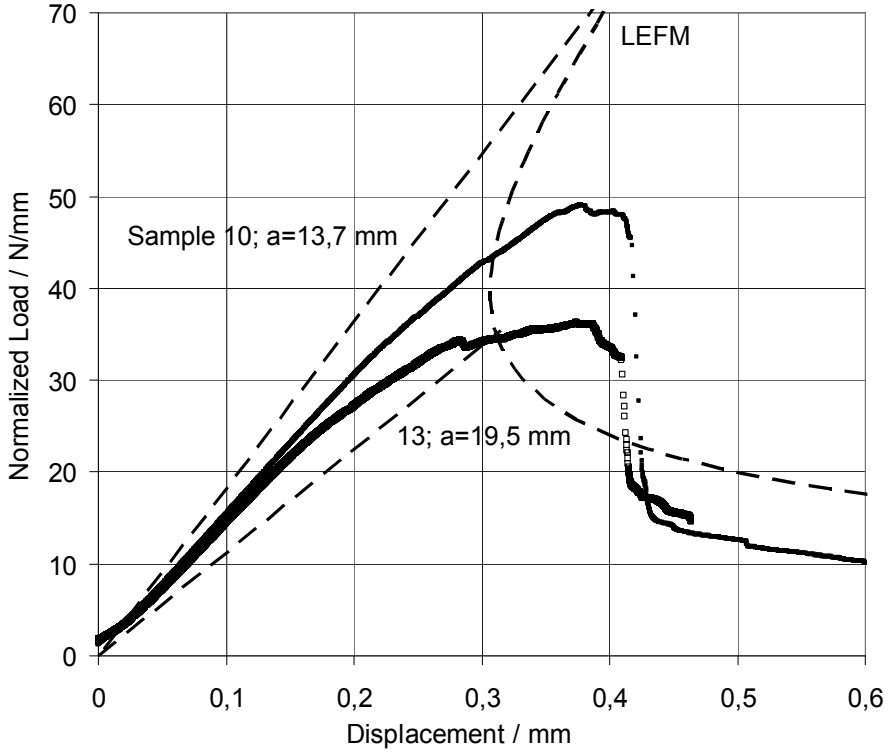

Figure 35: Width-normalized load-displacement curves from plate PH1879_D; stiffness and crack propagation curve from LEFM with G_{IIC} = 0.35 N/mm and E = 43.4 GPa.

6.2 FE-set up

6.2.1 *In-plane modelling: tensile, bending, SENB test*

First of all, it was aimed at describing the failure strength from tensile testing under varying orientations by typical failure criterions for orthotropic materials. Two failure criterions, the Hill criterion and the Tsai-Wu criterion, were fitted to experimental data of C/C-SiC and compared to the tensile test results. All necessary data to determine

the Hill and Tsai-Wu parameters is listed in Table 4. The orientations 0 and 90° correspond to the axes of the (x,y)-fibre coordinate system.

Table 4: Experimental data for the determination of Hill and Tsai-Wu parameters.

	Strength / MPa
Avg. Tensile 0 and 90°	128
Shear 0°	80
Tensile 45°	99
Compression 0°	250

The mathematical expression of the Tsai-Wu criterion in plane-stress state is [42]:

$$H_1\sigma_x + H_2\sigma_y + H_6\tau_{xy} + H_{11}{\sigma_x}^2 + H_{22}{\sigma_y}^2 + H_{66}{\tau_{xy}}^2 + 2H_{12}\sigma_x\sigma_y < 1 \quad \textbf{(28)}$$

For 0/90° fibre orientation:

$$H_1 = H_2 = \frac{1}{\sigma_t^{max}} - \frac{1}{\sigma_c^{max}} \quad \textbf{(29)}$$

$$H_{11} = H_{22} = \frac{1}{\sigma_t^{max}} \cdot \frac{1}{\sigma_c^{max}} \quad \textbf{(30)}$$

$$H_{66} = \frac{1}{(\tau_{xy}^{max})^2} \quad \textbf{(31)}$$

$$H_{12} = \frac{2}{\sigma_{45°}^2} - \frac{H_1 H_2}{\sigma_{45°}^2} - \frac{1}{2}(H_{11}H_{22}H_{66}) \quad \textbf{(32)}$$

σ_t^{max} and σ_c^{max} are the tensile and compression strength in 0/90° direction, τ_{xy}^{max} is the respective shear strength and $\sigma_{45°}$ is the tensile strength in 45° direction. The shear and compression strength in Table 4 were taken from an existing DLR database.

Table 5 gives a summary of the Tsai-Wu parameters determined for siliconized C/C-SiC.

Table 5: Tsai-Wu parameters for C/C-SiC.

H_1	0.0038125 / 1/MPa
H_2	0.0038125/ 1/MPa
H_6	0
H_{11}	0.00003125/ 1/MPa²
H_{22}	0.00003125/ 1/MPa²
H_{66}	0.00015625/ 1/MPa²
H_{12}	1.76656E-05/ 1/MPa²

Additionally, the Hill-criterion [43][44] was determined for the strength values of Table 4. For plane stress condition the Hill criterion is reduced to:

$$\sigma_{eff} = \sqrt{F\sigma_y^2 + G\sigma_x^2 + H\left(\sigma_x - \sigma_y\right)^2 + 2N\tau_{xy}^2} \quad \textbf{(33)}$$

with $\sigma_{eff} \leq 128$ MPa, that is the average tensile strength in 0 and 90° fibre direction, also called reference strength σ_0. F, G, H and N are defined as:

$$F = \frac{1}{2}\left(\frac{1}{R_{yy}^2} + \frac{1}{R_{zz}^2} - \frac{1}{R_{xx}^2}\right) \quad \textbf{(34)}$$

$$G = \frac{1}{2}\left(\frac{1}{R_{zz}^2} + \frac{1}{R_{xx}^2} - \frac{1}{R_{yy}^2}\right) \quad \textbf{(35)}$$

$$H = \frac{1}{2}\left(\frac{1}{R_{xx}^2} + \frac{1}{R_{yy}^2} - \frac{1}{R_{zz}^2}\right) \quad \textbf{(36)}$$

$$N = \frac{3}{2}\left(\frac{1}{R_{xy}^2}\right) \quad \textbf{(37)}$$

with the strength ratios and the reference strength σ_0=128 MPa:

$$R_{xx} = \frac{\sigma_x^{max}}{\sigma_0} \quad ; \quad R_{yy} = \frac{\sigma_y^{max}}{\sigma_0} \quad ; \quad R_{zz} = \frac{\sigma_z^{max}}{\sigma_0} \quad ; \quad R_{xy} = \sqrt{3}\frac{\tau_{xy}^{max}}{\sigma_0} \quad \textbf{(38)}$$

R_{zz} was not calculated following the equation from literature [43][44] but R_{zz} was fitted to the 45° tensile strength $\sigma_{45°}$, using equation (32) with $\sigma_x = \sigma_y = \tau_{xy} = \sigma_{45°}/2$:

$$\sigma_0 = \sqrt{\left(\sigma_{45°}/2\right)^2 \left(\frac{1}{R_{zz}^2} + \frac{3}{R_{xy}^2}\right)} \tag{39}$$

Consequently:

$$R_{zz} = \sqrt{\frac{1}{\left(\frac{2\sigma_0}{\sigma_{45°}}\right)^2 - \frac{3}{R_{xy}^2}}} \tag{40}$$

The following stress ratios were calculated, as shown in Table 6:

Table 6: Hill-stress ratios.

R_{xx}	1.0
R_{yy}	1.0
R_{zz}	0.49
R_{xy}	1.08

Figure 36 a shows a comparison of the calculated major normal and shear stress fractions from tensile test with the resulting stress limits from the Tsai-Wu and Hill failure criterions. Only the major normal stress fractions are plotted in Figure 36 a. The tensile and shear stress fractions in the (x,y)-fibre coordinate system were calculated by the reduced Cartesian transformations [45] for each tensile strength $\sigma_1(\alpha)$:

$$\sigma_x = \sigma_1 cos^2\alpha \; ; \qquad \sigma_y = \sigma_1 sin^2\alpha \; ; \qquad \tau_{xy} = -\sigma_1 sin\alpha \, cos\alpha \tag{41}$$

The shear stress limits were calculated from $\sigma_x(\alpha)$ and $\sigma_y(\alpha)$ by Tsai-Wu and Hill equations (28)(33). Both criterions describe the tensile strength in the different orientations rather well. Figure 37 b shows the Hill and Tsai-Wu failure criterions as determined for C/C-SiC in the σ_x-τ_{xy}-plane. The envelope for combined normal stresses in x and y direction, i.e. under biaxial normal load, was not-plotted because the results vary strongly with the R_{zz}-, respectively H_{12}-parameter. Those parameters have to be validated by further biaxial testing first.

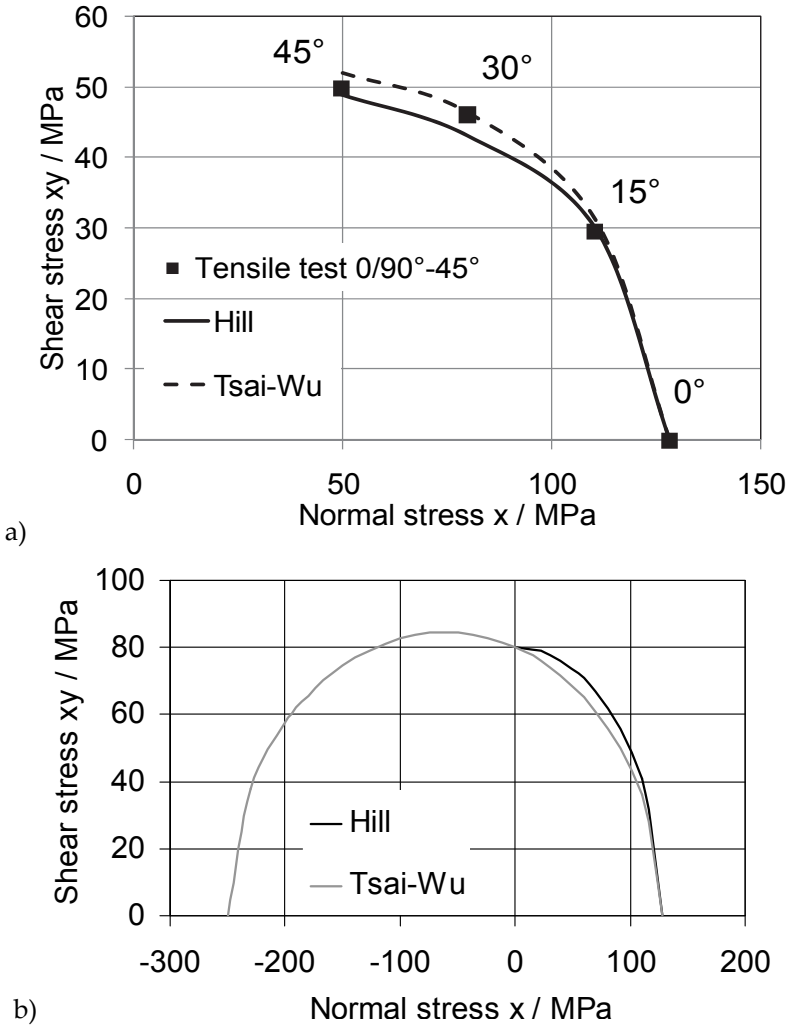

Figure 36: Tensile test results in comparison with Hill and Tsai-Wu criterions (a) Hill and Tsai-Wu failure envelopes (b).

An anisotropic hardening model was needed to describe the non-linear behaviour of C/C-SiC. The commercial code ANSYS WB 12.1 [44] is providing different yield models which are based on the Hill yield criterion. Since the Hill failure criterion was describing the tensile strength in satisfying accuracy, it was expected that the generalized Hill yield function from Shih and Lee [46], implemented in ANSYS, would also give results in good agreement with the experimental non-linear behaviour.

For isotropic hardening multilinear hardening models are implemented in ANSYS. However, for anisotropic hardening only the bilinear model, following the work from Valliappan et al. [47] is applicable. This bilinear model was used to describe the behaviour beyond yield stress.

The equivalent stress K for the generalized Hill yield criterion by Shih and Lee [46] is:

$$(\sigma)^T [M](\sigma) - (\sigma)^T \{L\} = K \qquad \textbf{(42)}$$

The formulation is similar to the anisotropic Hill criterion but with an extension $(\sigma)^T\{L\}$ for differing tensile and compression yield properties. The 0/90°-reinforced C/C-SiC has three orthogonal planes of symmetry. The plastic behaviour therefore can be described by the three element coordinate directions and the three shear stress-strain curves. M has the form:

$$M = \begin{bmatrix} M_{11} & M_{12} & M_{13} & 0 & 0 & 0 \\ M_{12} & M_{22} & M_{23} & 0 & 0 & 0 \\ M_{13} & M_{23} & M_{33} & 0 & 0 & 0 \\ 0 & 0 & 0 & M_{44} & 0 & 0 \\ 0 & 0 & 0 & 0 & M_{55} & 0 \\ 0 & 0 & 0 & 0 & 0 & M_{66} \end{bmatrix} \quad \textbf{(43)}$$

With M_{jj} for j = 1-3 and 4-6, respectively:

$$M_{jj} = \frac{K}{\sigma_{+j}\sigma_{-j}}; \; M_{jj} = \frac{K}{\tau^2{}_j} \quad \textbf{(44)}$$

Assuming plastic incompressibility yields the following off axis relations:

$$M_{12} = -1/2(M_{11} + M_{22} - M_{33}) \quad \textbf{(45)}$$

$$M_{13} = -1/2(M_{11} - M_{22} + M_{33}) \quad \textbf{(46)}$$

$$M_{23} = -1/2(-M_{11} + M_{22} + M_{33}) \quad \textbf{(47)}$$

σ_{+j} is the tensile yield stress, σ_{-j} is the compressive yield stress in j direction. The compressive yield stress is handled as a positive number here. τ_j is the respective shear yield stress.

With M_{11}=1, K is defined in the (x,y)-fibre coordinate system to be:

$$K = \sigma_{+x}\sigma_{-x} \quad \textbf{(48)}$$

Since the C/C-SiC material did not show a distinctive yield point in any direction, virtual initial yield stresses, σ_{0j} and τ_{0j}, were defined as half of the ultimate tensile and shear strength from best average curves, see Figure 37. A best average stress-strain curve of 0 and 90° tensile test was selected for the tensile input in x and y direction. The secant slopes from 0 MPa to the virtual yield point and from there on to failure stress were determined. Figure 37 shows the determination of the secant slopes for the uniaxial tensile stress-strain curve in x direction and for the xy shear stress-strain curve. The input data for the bilinear behaviour and yield stresses are summarized in Table 7. Although, the simple bilinear input for the shear stress-strain-curve shows some deviations from the experimental curve the resulting numerical stress-strain behaviour, e.g. the 45° tensile behaviour, showed good agreement with the experimental 45° tensile test, as will be shown in chapter 6.2.1.

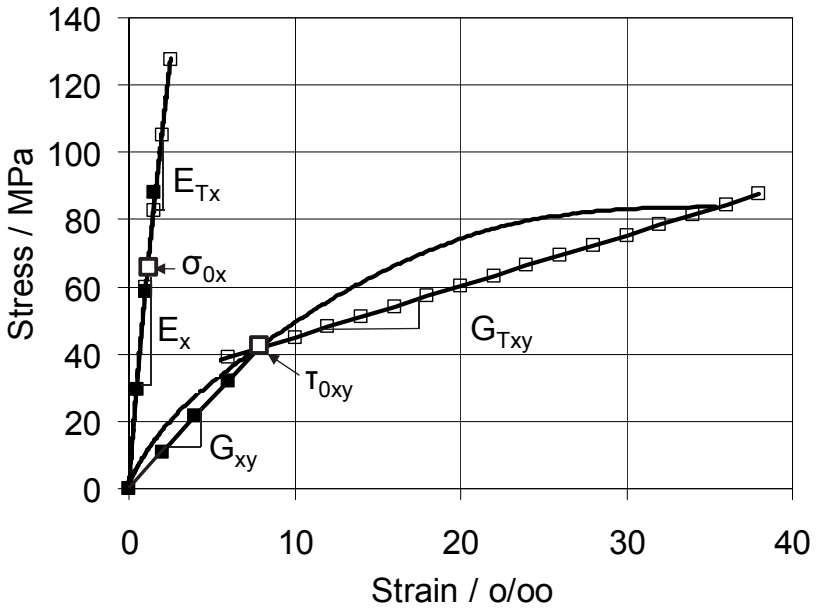

Figure 37: Determination of in-plane input data for bilinear hardening model [22].

Table 7: Input data in fibre coordinate system (x,y) for bilinear hardening model.

	Strength σ_{max} / MPa	Yield stress $\sigma_{+0j} = 1/2\ \sigma_{max}$ / MPa	Compressive yield stress σ_{-0j} / MPa	Elastic modulus E_j / GPa	ν	Tangent modulus E_{+Tj} / GPa	Compressive tangent modulus E_{-Tj} / GPa
x	128	64	64	58	-	44	56
y	128	64	64	58	-	44	56
z	-	64	64	20	-	19	19
xy [a]	80	40	-	5.14	0.01	1.6	-
yz [a]	76	38	-	6.6	0.1	2.54	-
xz [a]	21.4	10.7	-	9.06 (6.6) [b]	0.1	4	-

[a] Measurements from Iosipescu test [48]; [b] Theoretical value due to 0/90° symmetry.

Finally M was calculated from the input data in Table 7:

$$M = \begin{bmatrix} 1 & -0.5 & -0.5 & 0 & 0 & 0 \\ -0.5 & 1 & -0.5 & 0 & 0 & 0 \\ -0.5 & -0.5 & 1 & 0 & 0 & 0 \\ 0 & 0 & 0 & 2.56 & 0 & 0 \\ 0 & 0 & 0 & 0 & 2.84 & 0 \\ 0 & 0 & 0 & 0 & 0 & 35.78 \end{bmatrix} \quad \textbf{(49)}$$

Only the shear stress ratios deviate from the isotropic ratios: $M_{44} = M_{55} = M_{66} = 3$.

Table 7 shows that identical yield stresses were applied as input for tensile and compression yielding. The compression behaviour is nearly linear elastic. Nevertheless similar yield stresses had to be defined to fulfill the consistency equations, see equations (50) and (51).

The following consistency equation had to be fulfilled due to the requirements of the plastic incompressibility:

$$\frac{\sigma_{+x} - \sigma_{-x}}{\sigma_{+x}\sigma_{-x}} + \frac{\sigma_{+y} - \sigma_{-y}}{\sigma_{+y}\sigma_{-y}} + \frac{\sigma_{+z} - \sigma_{-z}}{\sigma_{+z}\sigma_{-z}} = 0 \quad \textbf{(50)}$$

Furthermore the yield stress has to describe a closed elliptical envelope. So the following criterion had to be met:

$$M_{11}^2 + M_{22}^2 + M_{33}^2 - 2(M_{11}M_{22} + M_{22}M_{33} + M_{11}M_{33}) < 0 \quad \textbf{(51)}$$

The strength differential vector {L} in equation (42) describes the differences in tensile and compressive yield stress and has the form:

$$\{L\} = \begin{bmatrix} L_1 \\ L_2 \\ L_3 \\ 0 \\ 0 \\ 0 \end{bmatrix} \quad \textbf{(52)}$$

The entries of {L} are calculated as described in equation (53). {L} is equal to zero when using the input yield stresses from Table 7. That means, no differences in initial tensile and compression yield stresses were defined in order to fulfill the consistency equations (50) and (51).

$$L_j = M_{jj}(\sigma_{+j} - \sigma_{-j}) \quad \textbf{(53)}$$

Since the yield stress changes with plastic strain, the consistency criterions are also limiting the range of tangent moduli E_T in Table 7, which may be chosen. Due to the restrictions for differing tensile and compressive tangent moduli, E_T, it was not possible to model the almost linear elastic compression side, with E_{-Tx} = 56 GPa,

together with the non-linear tensile side, with E_{+Tx} = 44 GPa, by using the presented bilinear hardening model and the parameters from Table 7.

The anisotropic non-linear tensile behaviour, however, could be modelled separately with the parameters in Table 7 by using the yield model from Shih and Lee [46] and the work hardening rule, as presented by Valliappan et al. [47].

The subsequent yield strength increases with the amount of plastic work done in that direction, as described by Valliappan et al. [47]. The plastic work is equated to get an equivalent change in all directions. In that way the subsequent yield strengths in the fibre coordinate system may be calculated from any adopted loading direction. The total plastic work in x direction, W_x^p, is e.g. [47]:

$$W_x^p = 1/2\varepsilon_x^p(\sigma_{0x} + \sigma_x) \qquad \textbf{(54)}$$

with plastic strain ε_x^p and the initial yield stress σ_{0x} and the updated yield stress σ_x.

$$\varepsilon_x^p = (\sigma_x - \sigma_{0x})/E_{px} \qquad \textbf{(55)}$$

E_{px} is the plastic modulus:

$$E_{px} = \frac{E_x E_{Tx}}{E_x - E_{Tx}} \qquad \textbf{(56)}$$

E_T is the tangent modulus from bilinear uniaxial stress-strain input; as determined in Figure 37 and summarized in Table 7. The updated yield stress for the bilinear stress-strain behaviour in x direction is:

$$\sigma_x = \sqrt{2W_x^p E_{px} + \sigma_{0x}^2} \qquad \textbf{(57)}$$

The last equation determines the updated yield stresses by equating the amount of plastic work done on the material to an equivalent amount of plastic work in each of the coordinate directions [47].

The stress-strain results from 4-point bending test, Figure 19 in chapter 6.1.2, and the compression tests presented by Fink [14] showed that the compression behaviour of C/C-SiC is mainly linear elastic. The tensile behaviour, depending on the fibre orientation, showed strong non-linearity. Because of the restrictions of the consistency equations (50) and (51) of the bilinear hardening model by Valliappan et al. [47] the FE-model for C/C-SiC under bending load had to be divided into an upper elastic and a lower non-linear half body, see Figure 38 a. The non-linear tensile part was modelled with the complete data in Table 7. The linear elastic compression part was modelled using only the Young's moduli and initial shear moduli from Table 7.

Since the differing stress-strain behaviour is leading to an upwards shift of the neutral plane, the subdivision into half bodies is not exactly correct. However, the middle section of the beam is not reaching yield stress at all and therefore this simplification is acceptable.

The residual sample height was divided, into an upper linear elastic and lower non-linear section for modelling the SENB test, as shown in Figure 38 b. This assumption was confirmed by linear-elastic FEA. Linear hexahedron elements (Solid95) were used for the 3D bending- and linear rectangular elements (Plane42) for the 2D SENB-model.

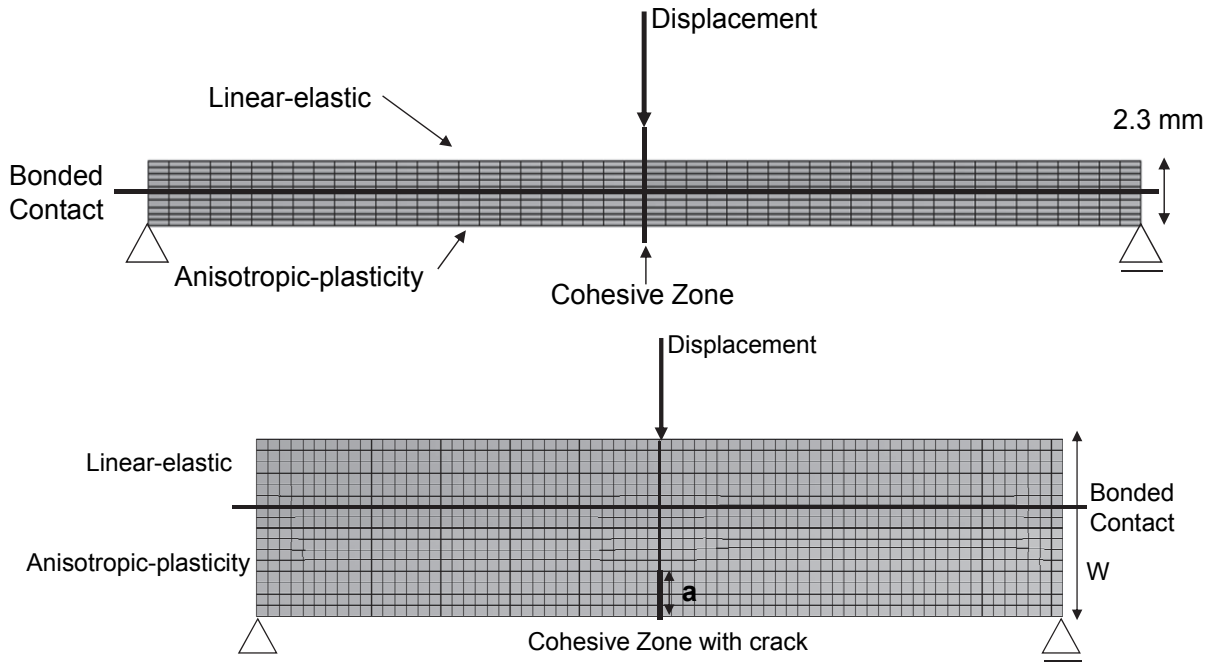

Figure 38: FE-models for bending (a) and SENB test (b), see also [22].

The same input data, Table 7, was used for bending and SENB-modelling. Only the interlaminar shear modulus G_{xz} was reduced to 2.4 GPa for modelling the SENB test. The interlaminar tangent shear modulus was down scaled accordingly. The reduction of G_{xz} showed little influence on the long-beam bending results but was necessary to fit the FEA to the results from SENB test with short support distance and strong interlaminar shear deformation. The interlaminar shear modulus from Iosipescu test, 9.06 GPa [48] in Table 7 , was found to be much higher than evaluated from SENB test or from short-beam bending test, ca. 4 GPa, see Figure 17. The desiliconized C/C-SiC was modelled with the data from Table 7, too. Only the interlaminar shear modulus was adapted to 4 GPa to fit to the experimental load deflection data. Due to the large differences between interlaminar shear modulus from Iosipescu test [48] and from short-beam bending, Figure 17, the true value is not yet clear.

The ultimate failure of C/C-SiC in SENB and 3-point bending test was modelled with Cohesive Zone Elements (Conta174, Targe170). The cohesive zone was introduced in the middle of the sample at the location of maximum tensile and compressive stresses. The cohesive zone modelling approach was chosen in order to simulate crack propagation in C/C-SiC by taking all pseudo-plastic damage processes, like micro-cracking at the crack front, into account.

The cohesive zone model describes the debonding of the material as a linear contact stress-separation curve, as presented by Alfano and Crisfield [32], see Figure 39. The

separation starts at the maximum stress value σ_{max} followed by linear softening up to the critical separation value u_c.
Following the work from Rice [49], the area under the stress-separation curve is equivalent to the critical strain energy release rate G_c as defined by Griffith [50]. In that way Rice is establishing a link between cohesive zone theory by Dugdale [51] and Barenblatt [52] with Griffith theory. Rice is concluding that the integral of any stress-separation curve is equal to two times the surface energy in the case of small-scale yielding.
Nakayama [39] described the energy needed to create new surfaces as the sum of the thermodynamic surface energy and the energy dissipated by plastic or pseudo-plastic deformations. The total energy to create surfaces by crack propagation is corresponding to the WOF. The WOF was determined in SENB tests for C/C-SiC. The input for the critical energy release rate of the cohesive zone model was defined as:

$$G_c = \frac{1}{2}\sigma_{max}\, u_c = 2\, WOF \tag{58}$$

The softening behaviour can be described with the following equation from ANSYS documentation [44]:

$$\sigma = K_n u(1 - d_n) \tag{59}$$

Where σ is the contact stress, K_n is the initial contact stiffness, u is the separation and d_n is the debonding or damage parameter. The debonding parameter for mode I is defined as:

$$d_n = \left(\frac{u - u_s}{u}\right) \cdot \left(\frac{u_c}{u_c - u_s}\right) \tag{60}$$

with u_s the separation at maximum stress σ_{max}.

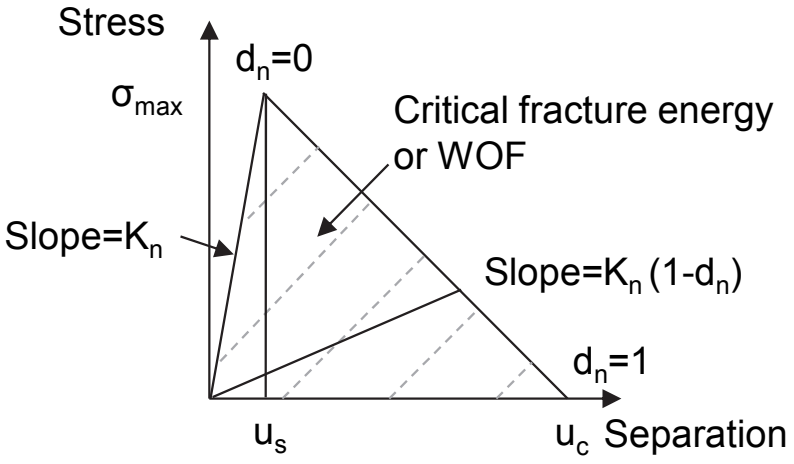

Figure 39: Cohesive zone model with linear softening [32][44].

The initial contact stiffness K_n was defined as $1e^6$ MPa/mm which can be considered as ideal rigid contact. Further input values for the cohesive zone model are the Work of Fracture (WOF) as determined from SENB testing, chapter 6.1.3, and the directional ultimate tensile strength σ_{max}. Since the WOF was determined to be almost independent of crack orientation, see Figure 21 in chapter 6.1.3, an average value of 2.5 N/mm was applied for all loading directions. The WOF for desiliconized C/C-SiC, 1.75 N/mm, was taken from SENB results from Weisenberger [53]. The maximum stress value was defined, corresponding to the average tensile strength in the respective direction, see Table 8 and Figure 49 b for siliconized C/C-SiC. The tensile strength of desiliconized C/C-SiC was applied accordingly.

Table 8: Average tensile strength values used for cohesive zone failure models of plate PH2035_ND in siliconized state.

	σ_{max} / MPa
0°	140
15°	118
30°	106
45°	100

6.2.2 *Modelling of interlaminar behaviour*

Plate PH1879_D showed that the delaminations were filled with free silicon during siliconization. The free silicon was then removed during desiliconization again, compare Figure 11. Therefore the more critical state for interlaminar failure is the desiliconized state. Thus the interlaminar fracture mechanical modelling is focusing on desiliconized C/C-SiC. The mode I and II interlaminar fracture tests of desiliconized C/C-SiC in 0/90° orientation were modelled as 2D plane strain state with linear elastic properties only. The poisson ratios and first slopes in Table 7 were applied as elastic properties. The experimental results in chapter 6.1.1 confirmed that the Young's moduli of siliconized and desiliconized C/C-SiC are similar. Only the interlaminar shear modulus had to be adapted to the experimental stiffness. An interlaminar shear modulus of 4 GPa was used for DCB- and ENF-models.

6.2.2.1 DCB-model

Figure 40 shows the 2D-FE-set-up with aluminium loading blocks for DCB-modelling. The aluminium parts were modelled as isotropic linear elastic with E = 70 GPa and ν = 0.34. Further. The test was also modelled without loading blocks, so the displacement

was directly applied at the sample surface. Interlaminar failure was modeled by Cohesive Zone Elements, as described in Figure 39, chapter 6.2.1. K_n was again set to $1e^6$ MPa/mm and σ_{max} was defined as 5 MPa, that is the interlaminar tensile strength as determined from Geinitz [48]. The critical fracture energy was set to 0.16 N/mm as determined in chapter 6.1.4.1. Linear rectangular elements with 0.5 mm edge length were applied. 1000 substeps were used for the total displacement of about 1.5 mm.

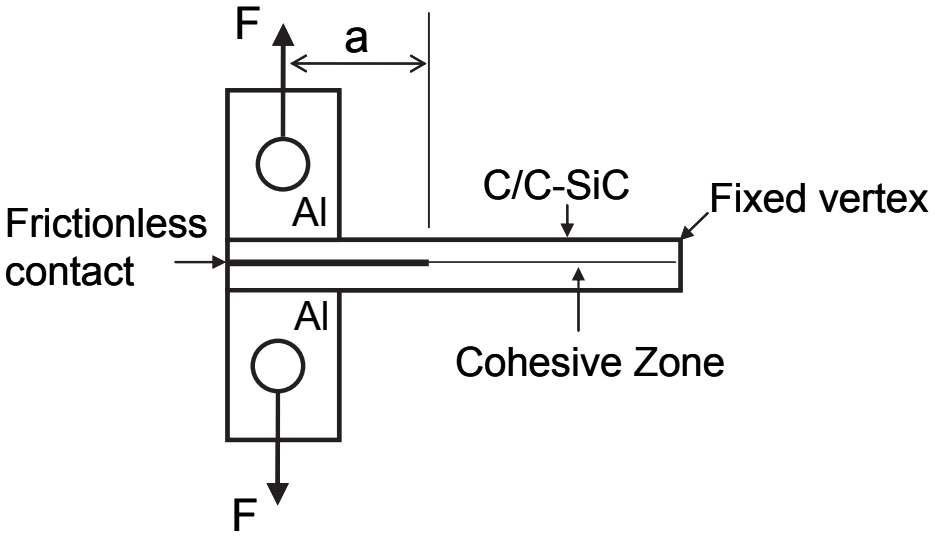

Figure 40: FE-set-up for DCB-model.

6.2.2.2 ENF-model

Figure 41 shows the 2D FE-set-up for ENF-modelling with exemplary initial crack lengths (12.7-18.5 mm). The frictionless contact region was adapted for the particular initial crack length. A frictionless contact was used due to the negligible influence of friction shown in chapter 6.3.5., Figure 52. The mode II failure was modelled by Cohesive Zone Elements, as described in chapter 6.2.1. The equations (58)-(60) from mode I correspond directly to the respective equations for mode II. K_n was set to $1e^6$ MPa/mm and τ_{max} was defined as 25 MPa, that is the interlaminar shear strength of C/C-SiC measured in compression shear test [1]. The critical fracture energy was set to 0.31 N/mm, respectively 0.35 N/mm, depending on the investigated plate material (Ph1991_ND and PH1879_D), see chapter 6.1.4.2. Linear rectangular elements of 0.5 mm edge length were applied. 1000 substeps were used for the total displacement of about 0.5 mm. ENF samples from C/C-SiC material tend to bending failure, as shown in chapter 6.1.4.2. For this reason additional perpendicular cohesive zone regions at the respective crack lengths and at the middle of the ENF-sample were introduced. Those are the regions of maximum normal stresses where tensile failure possibly may occur. The parameters for tensile failure modelling correspond to the cohesive zone parameters from bending and SENB models, see chapter 6.2.1. The maximum stress

value in 0/90° orientation, σ_{max}, was reduced to 92 MPa since the desiliconized C/C-SiC material showed lower tensile strength values than the siliconized C/C-SiC, compare Figure 15 b. The WOF was reduced to 1.75 N/mm as determined by Weisenberger [53] for desiliconized C/C-SiC. In order to compensate for the slight non-linear effects in 0/90° orientation the σ_{max} value was increased from 92 to 105 MPa when linear-elastic analysis were perfomed. The explanation therefore is given in chapter 6.3.3, Figure 48.

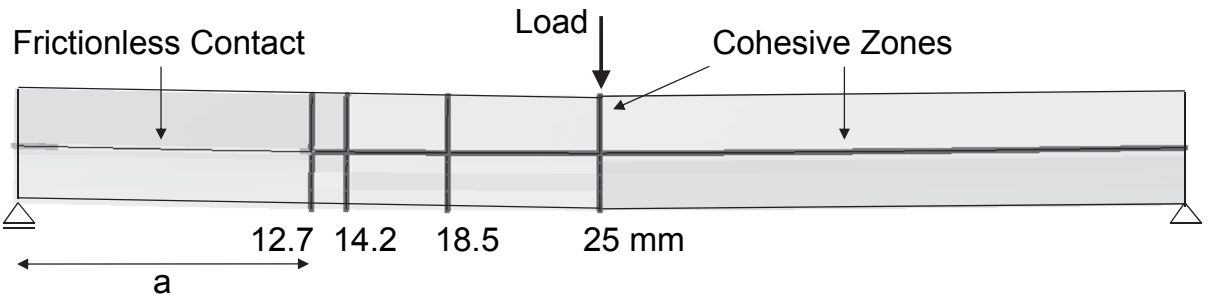

Figure 41: FE-set-up for ENF-model with varying initial crack length a; the frictionless contact was adapted for the investigated crack length.

6.3 FE- and experimental results

6.3.1 *Non-linear behaviour under tensile load*

In the first step the anisotropic yield model with bilinear hardening, see chapter 6.2.1, was evaluated by comparing the longitudinal and transverse stress-strain curves from tensile testing and FEA. The stress-strain curves from experiment and FE-modelling show good agreement in longitudinal as well as in transverse direction, see Figure 42. The initial stiffness from FEA is slightly below the experimental slopes in 30° and 45° orientation. This can be understood by considering the bilinear input data (Figure 37) which is always softer than the experimental data. Nevertheless the non-linear behaviour is overall well reproduced by the bilinear hardening model.

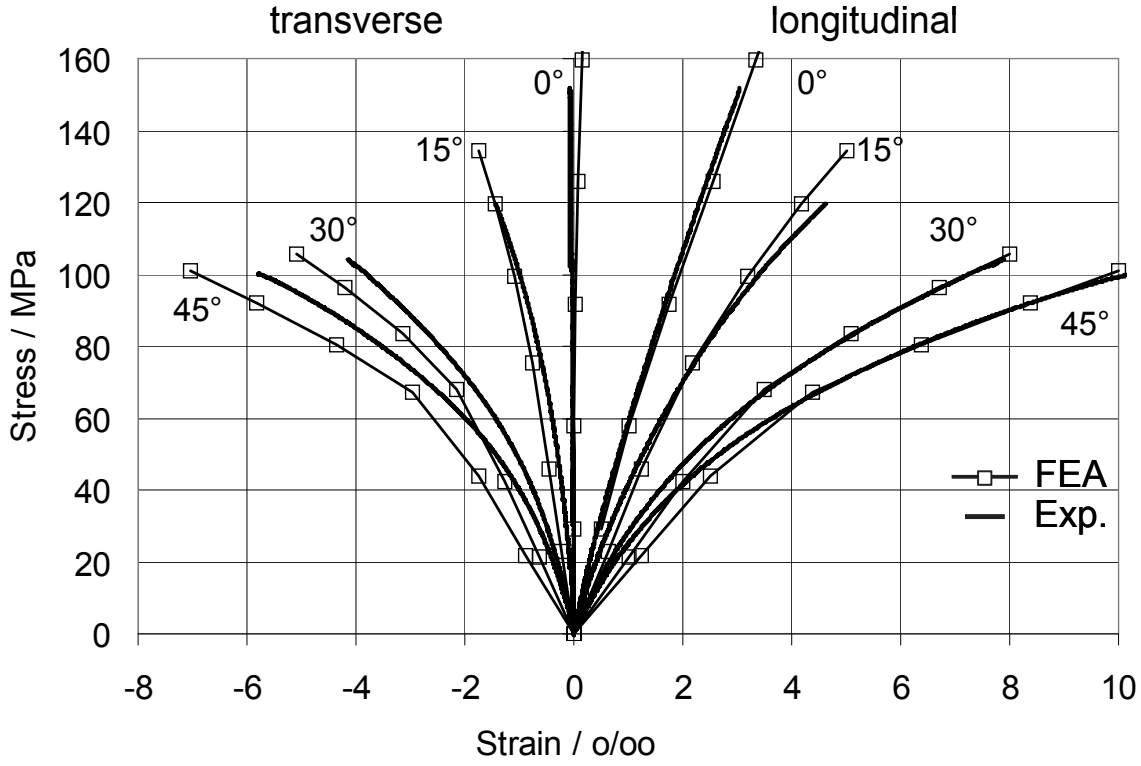

Figure 42: Comparison of longitudinal and transverse stress-strain behaviour from tensile test and FEA with anisotropic yield model and bilinear hardening [22].

6.3.2 *Non-linear behaviour under bending load*

Since the anisotropic yield model with bilinear hardening reproduced effectively the tensile behaviour in the different orientations it was applied for the tensile side of the bending model, too. Figure 43 shows the resulting strains from FEA and from experiment plotted together with the theoretical bending stresses calculated from the applied load. The stress-strain behaviour measured by strain gauges on the tensile side and the strains from FEA at the corresponding location are in good agreement.

The bending and tensile stress-strain curves from experiment and FEA are directly compared for the 45° loading direction. This comparison proofs the assumption from chapter 6.1.2: the differing stress-strain behaviour at the lower and upper side of the bending sample leads to decreased effective stresses on the tensile side. On the other hand, increased compressive stresses appear at the compression side of the beam. The neutral axis is shifted upwards in the direction of the compression side.

Classical beam theory cannot be applied to calculate the tensile and compression stresses of the bending sample accurately. The linear elastic compression side supports the non-linear tensile side and leads to decreased effective tensile stress values. In that

way an upwards shift of the theoretical bending stress-strain curves, see Figure 19 a and Figure 43, is caused. Figure 19 a in chapter 6.1.2 showed that this effect is pronounced for the loading directions with strong non-linear tensile behaviour, i.e. 30° and 45° directions. The experimental assumptions were confirmed by the FE results in Figure 43.

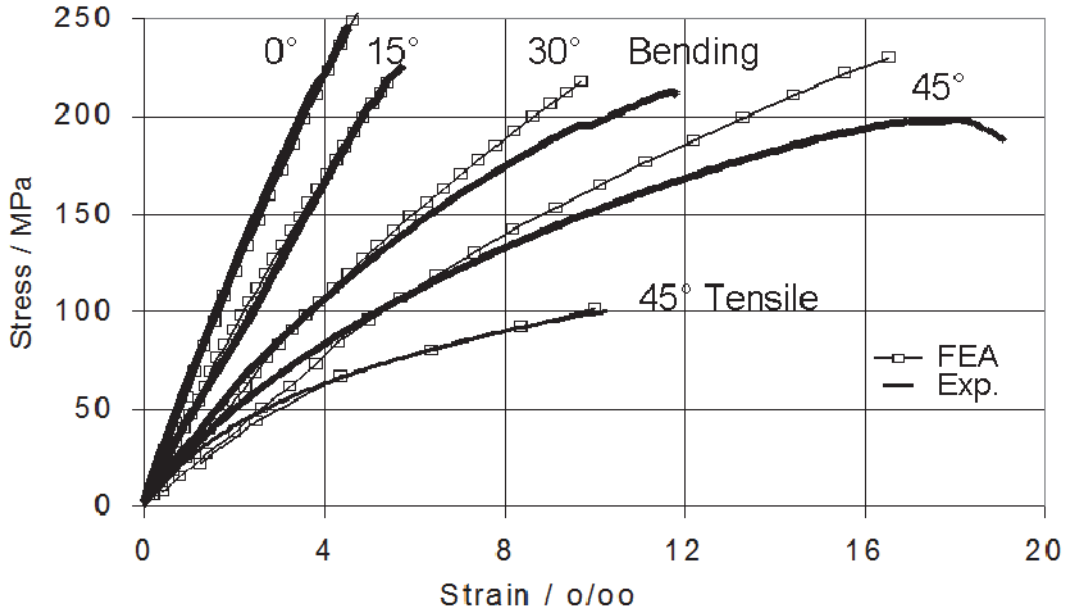

Figure 43: Strain results from FEA and experiment evaluated at the tensile side of the bending sample; the theoretical stress values were calculated from the applied load, following beam theory; the 45° tensile stress-strain curve is plotted for a direct comparison [22].

6.3.3 *Bending and SENB failure*

In the next step the translaminar SENB test was modelled partially bilinear with a cohesive zone introduced in the middle of the sample, see Figure 38 b. The fibre orientation is similar to the normal bending case in 0/90° direction but with shorter support distance and inserted notch. Figure 44 shows the FE-results from different meshes for a SENB test without initial crack (a/W=0). The results are almost independent of the investigated element sizes. For all meshes, a good agreement in stiffness and maximum load was reached in comparison to the experimental result. That is why the coarser mesh with 0.2 mm edge size was selected for the subsequent analysis.

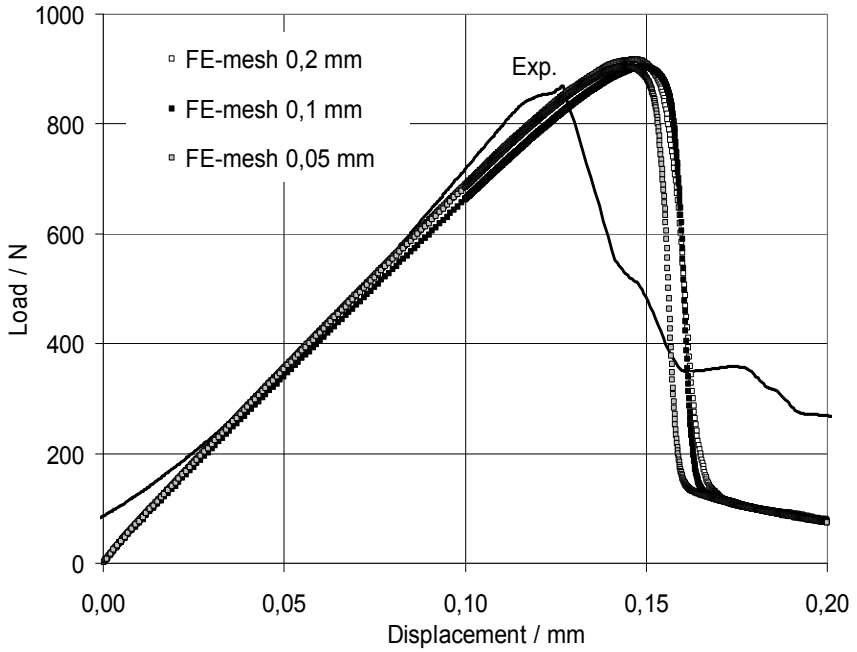

Figure 44: FE and experimental load-deflection curves for SENB set-up with a/W = 0; variation of element size.

Figure 45 shows a comparison of load-deflection curves from experiment, FEA and LEFM for different initial crack length ratios a/W. The crack propagation curve from LEFM is also plotted. The crack propagation curve was determined from the maximum bending stresses for varying a/W-ratios with an average K_{IC} value of 5.4 $MPam^{1/2}$ using equation (14). The average K_{IC} value was determined in chapter 6.1.3, see Figure 21 b. The loads plotted in Figure 45 were then calculated from the maximum bending stresses following equation (4). The following equations from Tada et al. [38] were used to calculate the theoretical stiffness for different ratios of a/W in Figure 45:

$$u_{total} = u_{nc} + u_c \tag{61}$$

The total displacement u_{total} is the sum of the displacement without crack u_{nc} and displacement due to crack opening u_c.

$$u_{nc} = \frac{F}{S_{nc}} \tag{62}$$

the experimental stiffness S_{nc} without pre-crack, a/W = 0, was determined to be 7033 N/mm, see Figure 45. The displacement due to crack opening u_c is:

$$u_c = L\frac{\sigma_b}{E}V\left(\frac{a}{W}\right) \tag{63}$$

with E = 17 GPa, which is the effective Young's modulus calculated from the experimental stiffness of 7033 N/mm following equation (7), and the correction factor V(a/W) from Tada et al. [38]. V(a/W) for L/W = 4 is:

$$V\left(\frac{a}{W}\right) = \left(\frac{\frac{a}{W}}{1-\frac{a}{W}}\right)^2 \left(5.58 - 19.57\left(\frac{a}{W}\right) + 36.82\left(\frac{a}{W}\right)^2 - 34.94\left(\frac{a}{W}\right)^3 + 12.77\left(\frac{a}{W}\right)^4\right) \quad \textbf{(64)}$$

The stiffness from FEA, experiment and LEFM are in good agreement for the investigated a/W-ratios. In general, the experimental and numerical results follow the crack propagation curve from LEFM. Only the load plateau from FEA is more pronounced than observed in experiment. The maximum load points from LEFM, FEA and experiment are in good agreement. The FEA is slightly overestimating the maximum load. Figure 46 confirms this result. The overall behaviour is well reproduced by FEA. Figure 45 and Figure 46 demonstrate that the critical load points for C/C-SiC may be predicted by the LEFM, using an average K_{Ic} value of 5.4 MPam$^{1/2}$, or by FEA, using the average G_{Ic} of 5 N/mm and the tensile strength of 140 MPa from chapter 6.1.3.

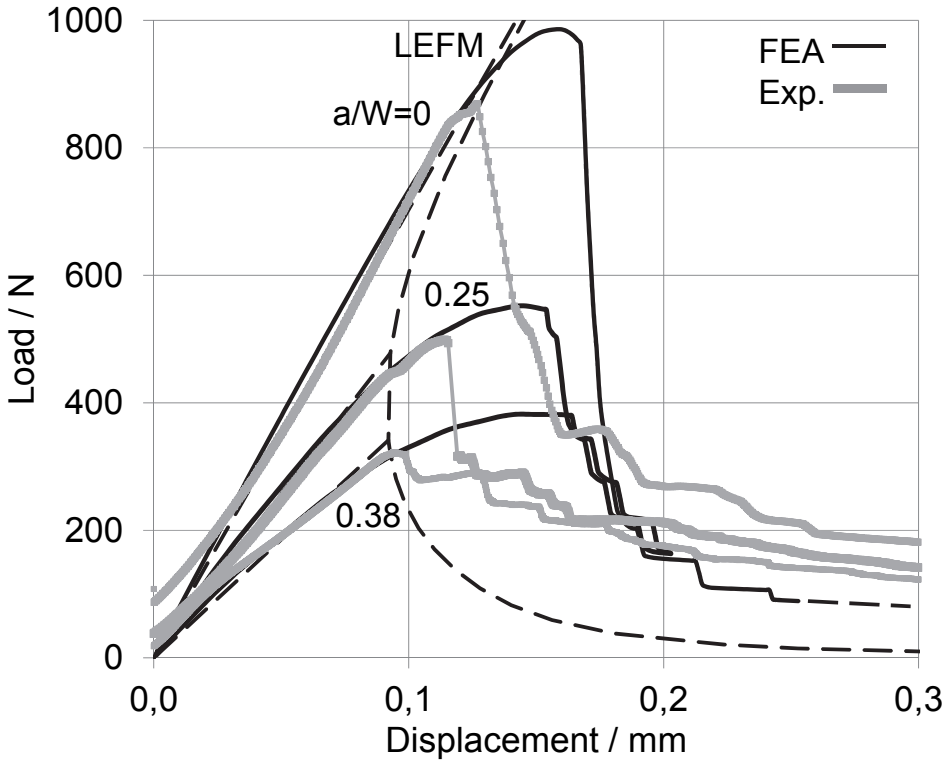

Figure 45: FE- and experimental load-deflection curves for SENB test with varying initial a/W-ratios in comparison with the slopes and crack propagation curve from LEFM.

Figure 46 shows the bending strength from experiment, LEFM and FEA in dependency of the relative crack length. Additionally, results from completely linear

elastic FEA are shown. The linear elastic FE-results are located on the curve from LEFM. The results from the partial non-linear FEA, however, show slightly higher strength values than LEFM and SENB test results. Only for small relative crack length lower than 0.1 the FEA deviates from LEFM. The resulting strength of an un-notched short-beam bending sample is again in rather good agreement with the experimental bending strength. Since the short beam bending strength of 200 MPa is relatively low compared to long beam bending strength of 240 MPa in the same direction, see Figure 49 b, the non-linear FEA is slightly overestimating this value.

Figure 46 is crucial because it shows that the bending strength can be reproduced with a fracture mechanical approach and cohesive zone modelling. The strength for a/W = 0 goes to infinity from a fracture mechanical point of view. Practically, the bending strength is limited by the strength of the material. The advantage of FEA in contrast to LEFM is the combination of fracture mechanical theory with the strength of materials. Considering the fracture mechanical solution, it could also be stated that the bending strength is equivalent to an inherent a/W-ratio of about 0.1. Indeed the C/C-SiC material is showing shrinkage matrix cracks which could be described as inherent pre-cracks. This hypothesis would implicate, however, that the bending strength of C/C-SiC material increases with increasing sample thickness. But this is not the case, as can be seen by comparing the bending strength in 0/90° direction for L/d ~ 20 for plate PH1991_ND and PH2035_ND in siliconized state. PH1991_ND had a thickness of about 4.92 mm, the thickness of plate PH2035_ND was 2.3 mm. The respective theoretical bending strengths are: 220 and 240 MPa, compare Figure 14 a and Figure 49 b. The observed opposite trend may be explained by the higher fibre volume content of plate PH2035_ND.

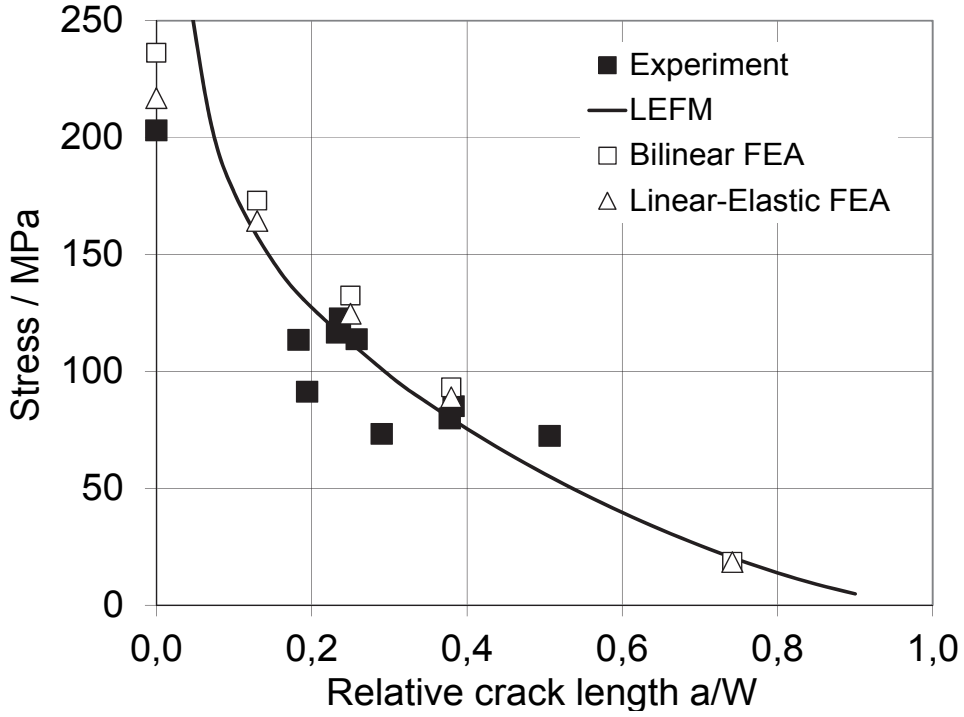

Figure 46: Bending strength from SENB test, LEFM, linear and non-linear FEA.

Subsequently, the same approach was used to model the long beam bending test in different loading directions. First the influence of translaminar G_{Ic} on the theoretical bending strength was investigated. Again, the critical stress value σ_{max} for the initiation of debonding was defined as the average tensile strength in 0/90° direction, i.e. 140 MPa (Table 8 and Figure 49 b). Figure 47 shows the theoretical bending stress, determined from the applied load of the FEA, plotted over the deflection. The resulting theoretical bending strength for low G_{Ic} values lies slightly above the tensile strength. Brittle failure with a steep load drop is observed after ultimate load. Even double the tensile strength is reached for high G_{Ic} values. The stress-deflection curve shows a reduced load drop and almost a plateau at maximum load.

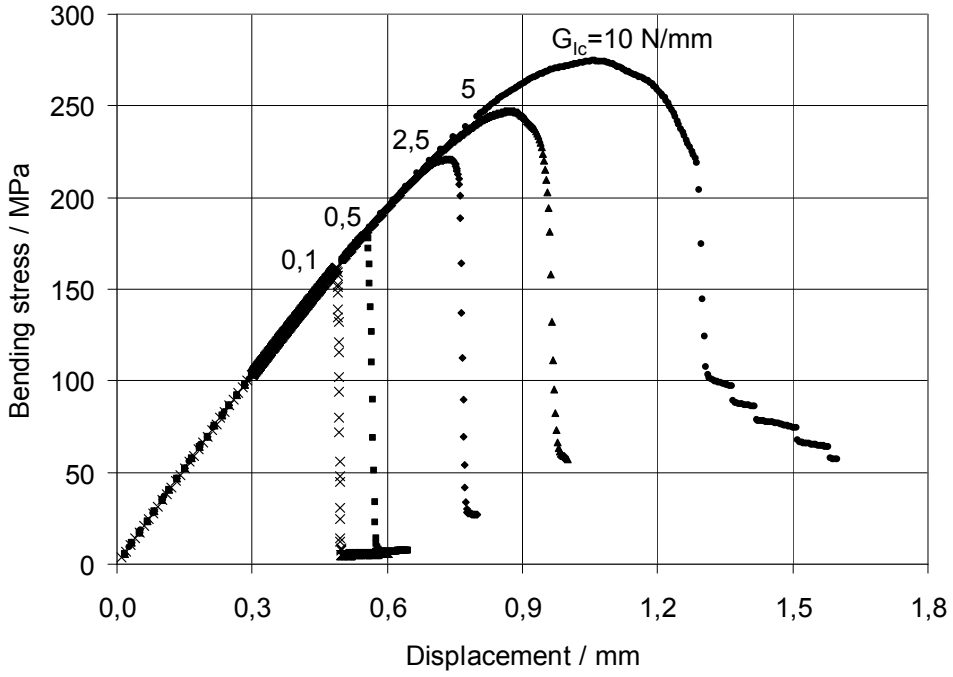

Figure 47: Theoretical stress values plotted over the deflection curves from partial bilinear FEA with varying translaminar G_{Ic}.

The results in Figure 47 show that the bending strength in 0/90° orientation is about 20 MPa above the tensile strength of 140 MPa for a very low G_{Ic} value of 0.1 N/mm. The difference is caused by the bilinear material model on the tensile side. Figure 48 a is comparing results from linear elastic and partial bilinear FEA. It is shown that the bending strength corresponds to the tensile strength for the linear elastic FEA with low G_{Ic} values. The 0/90° orientation shows only slight non-linear behaviour. Therefore, the difference between the bending strength from linear elastic and partial bilinear FEA is only ca. 20 MPa, compare Figure 46 (a/W = 0) and Figure 48 a. At the failure stress of 140 MPa, the true tensile stress from the bilinear analysis is 20 MPa below the linear elastic FE-result, compare Figure 48 b. Figure 48 a and b demonstrate that the ratio of bending to tensile strength is depending on two factors: first the differing material behaviour under tensile and compression load and secondly the fracture toughness. In 0/90° direction the non-linearity of the tensile side causes a

bending to tensile strength difference of 20 MPa. The residual difference of about 60-80 MPa can be explained by the fracture toughness of the material.

Assuming a similar non-linear tensile stress-strain behaviour for desiliconized C/C-SiC leads to a decrease of effective bending stresses of about 13 MPa at a true tensile stress of 92 MPa. That means at a given load and beam geometry a linear-elastic FEA or beam theory would compute a bending stress of 105 MPa when the true tensile strength value of 92 MPa is reached in an non-linear analysis.

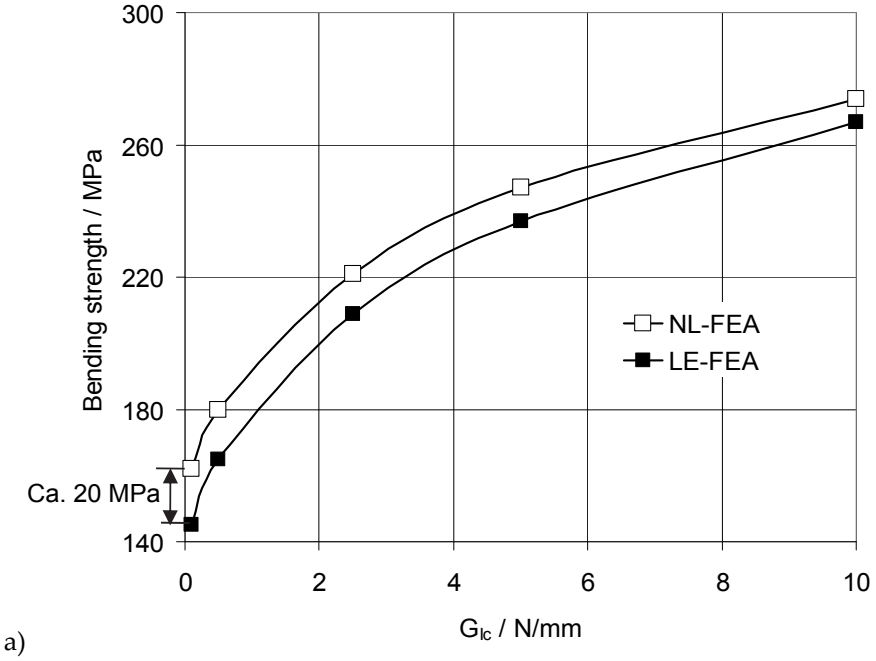

a)

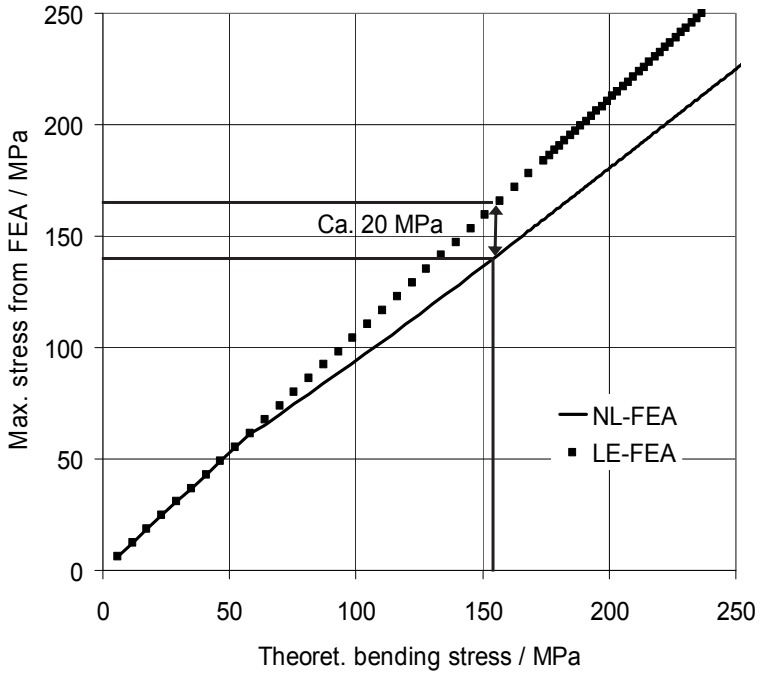

b)

Figure 48: Comparison of linear elastic and partial bilinear FEA: theoretical bending strength (a), maximum longitudinal tensile stress (b).

Finally, the average WOF 2.5 N/mm, as determined in chapter 6.1.3, and the directional tensile strengths (Table 8 and Figure 49 b) were used to model the long-beam bending failure in varying orientations. The resulting load-deflection behaviour from partial bilinear FEA is in good agreement with the experimental curves, see Figure 49 a. Overall, Figure 49 a and b demonstrate that the bilinear hardening model in combination with the fracture mechanical cohesive zone approach predicts the bending strength with good accuracy.

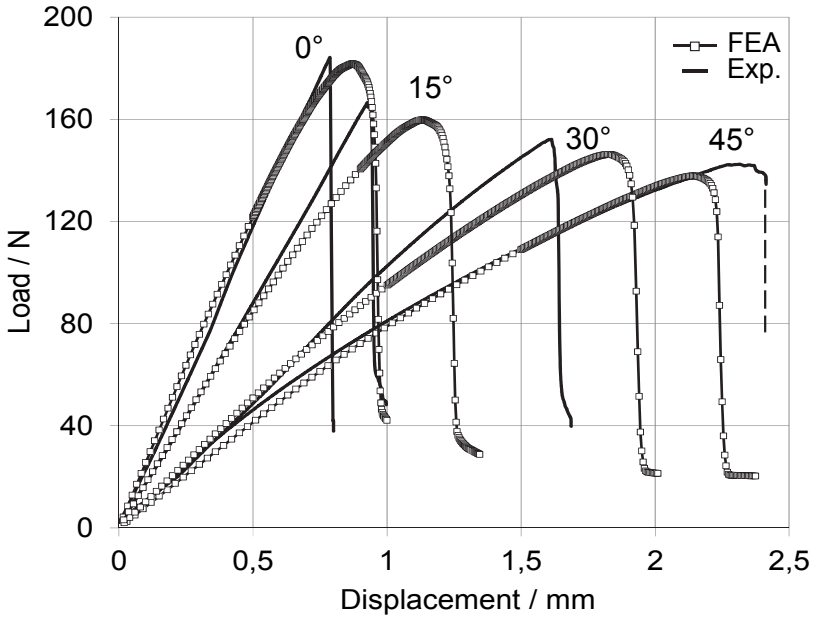

a)

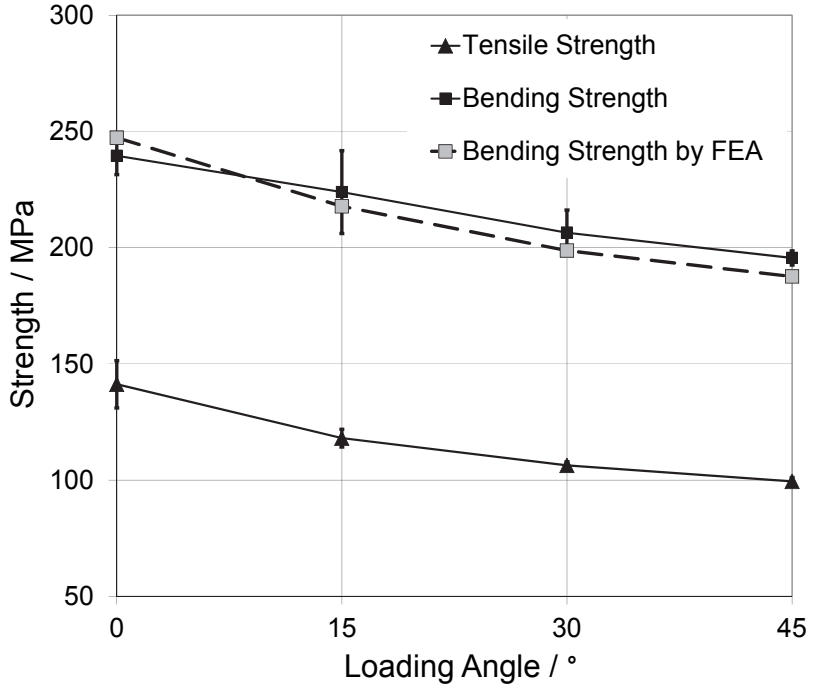

b)

Figure 49: Load-deflection curves from partial bilinear FEA with cohesive zone failure model (a), theoretical failure stresses from FEA and experiments (b).

6.3.4 *DCB-results*

The present chapter is comparing the results from 2D-FEA of DCB test with experimental results and LEFM calculations from chapter 6.1.4.1. The FEA was performed as described in chapter 6.2.2.1. Mode I interlaminar failure was modelled by Cohesive Zone Elements. The C/C-SiC material itself was modelled as linear elastic. Figure 50 a shows the load-displacement curves from 2D-FEA with and without aluminum loading blocks. The load-deflection curves are similar even for the relatively short initial crack length of 15.6 mm. It does obviously not affect the results if the load is introduced via loading blocks or directly on the sample surface. Therefore the subsequent simulations were performed without loading blocks. Figure 50 b and c show the crack length and interlaminar tensile strains at the load points 1-4 indicated in Figure 50 a. The load drop after image 4 is caused due to total delamination of the sample.

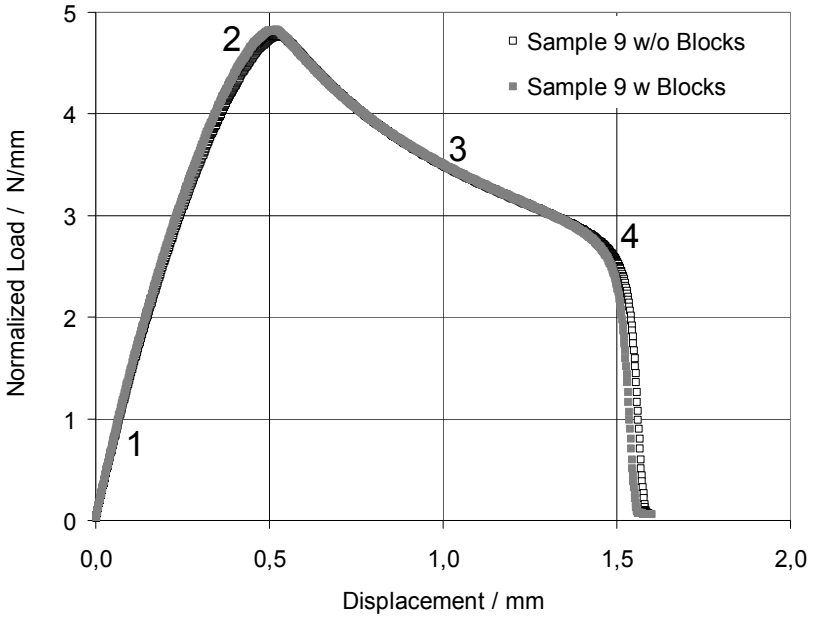

a)

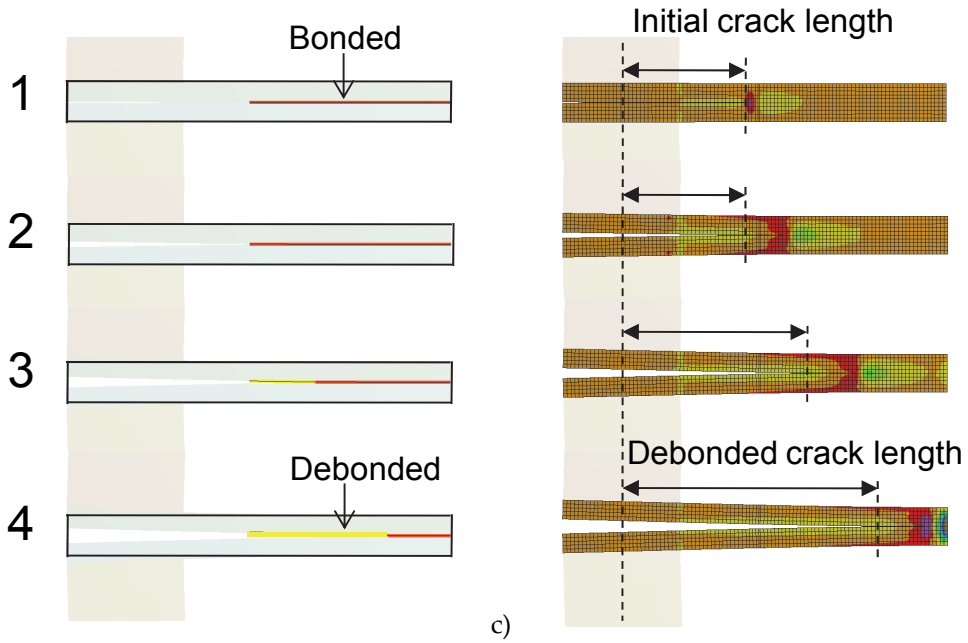

b) c)

Figure 50: Load-displacement curves from 2D-FEA of DCB test with an initial crack length of 15.6 mm (a), corresponding cohesive zone status (b) and qualitative interlaminar strain distribution for load points 1-4 (c).

Figure 51 shows the width-normalized load-displacement curves from experiment, FEA and the crack propagation curves from LEFM for two different Young's moduli. The stiffness from FEA and DCB test correspond rather well, except for sample 8 with the largest initial crack length. The crack in sample 8 showed a slight offset from the midplane which might explain the lower experimental stiffness. In this case the FEA is overestimating the stiffness. The LEFM curve for the average effective modulus of 24.5 GPa corresponds well with the experimental load points of crack initiation (5%-offset),

as shown in chapter 6.1.4.1, Figure 27. The crack propagation curve from LEFM for a standard Young's modulus of 58 GPa agrees perfectly with the propagation curve from FEA with the same Young's modulus. However, LEFM with a Young's modulus of 58 GPa is overestimating the experimental stiffness and therewith its crack initiation loads (5%-offset), see Figure 22 and Figure 27.

In contrast to the LEFM and FEA crack propagation curves the experimental curves show less decrease of load after crack initiation. The load stays almost constant until the delamination has reached the end of the sample, especially for larger initial crack length, compare sample 8 in Figure 51. That means: the crack initiation is well described by LEFM and FEA for all samples. But the full delamination is reached at much larger displacements in experiment than in FEA. Following equation (19) from beam theory, the G_{Ic} is increasing with crack propagation. Therewith, the comparison of FEA and experimental crack propagation curves confirmed the results from chapter 6.1.4.1, Figure 26, indicating a strong increase of G_{Ic} with crack propagation for C/C-SiC. Nevertheless, the linear elastic 2D-FEA, using a Young's modulus of 58 GPa and a critical energy release rate G_{Ic} of 0.16 N/mm with linear softening, was in good agreement with the experimental stiffness and crack initiation loads.

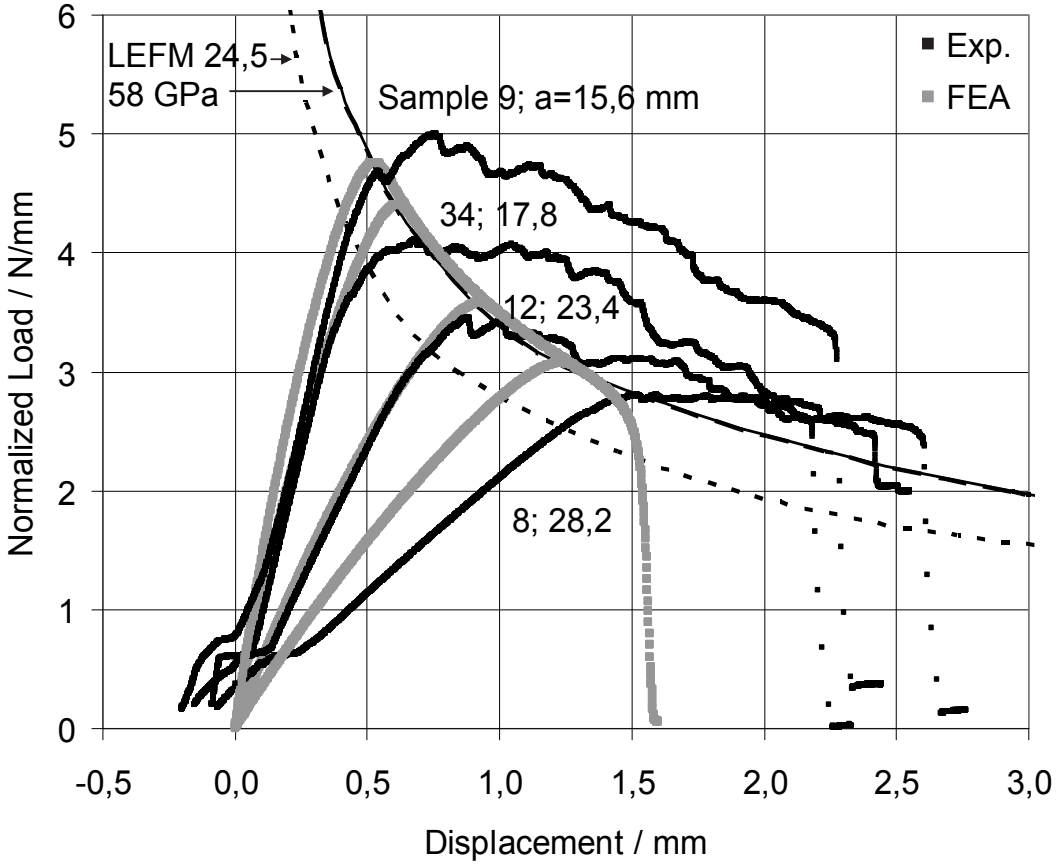

Figure 51: Load-displacement curves from DCB test, FEA and propagation curves from LEFM (G_{Ic} = 0.16 N/mm); sample numbers and initial crack lengths are indicated.

6.3.5 *ENF-results*

The following pages are summarizing the results from 2D linear elastic FEA of ENF test in comparison with experimental and analytical results from LEFM. Figure 52 a and b are showing the FEA-results for different FE-parameters. Figure 52 a indicates that the FE-results are rather independent of element kind (linear or quadratic) and size. A linear mesh with 0.5 mm edge length was used for further modelling. Figure 52 b demonstrates that the coefficient of friction μ has some influence on the FE-result. The results are comparable for μ=0 and μ=0.2. The stiffness and maximum load is slightly increased for μ=0.7. The coefficient of friction between C/C-SiC surfaces is about 0.7. However, the coefficient of friction between aluminum and grinded C/C-SiC is rather low, about 0.2 [54]. The ENF-testing was performed with an aluminum plate in between of the sawed part of the crack planes. Because of the low coefficient of friction between aluminum and C/C-SiC the coefficient of friction was simply set to 0 for further FEAs. The crack propagation curves in Figure 52 and Figure 53 were calculated for an effective Young's modulus of 43.4 GPa, as presented in chapter 6.1.4.2.

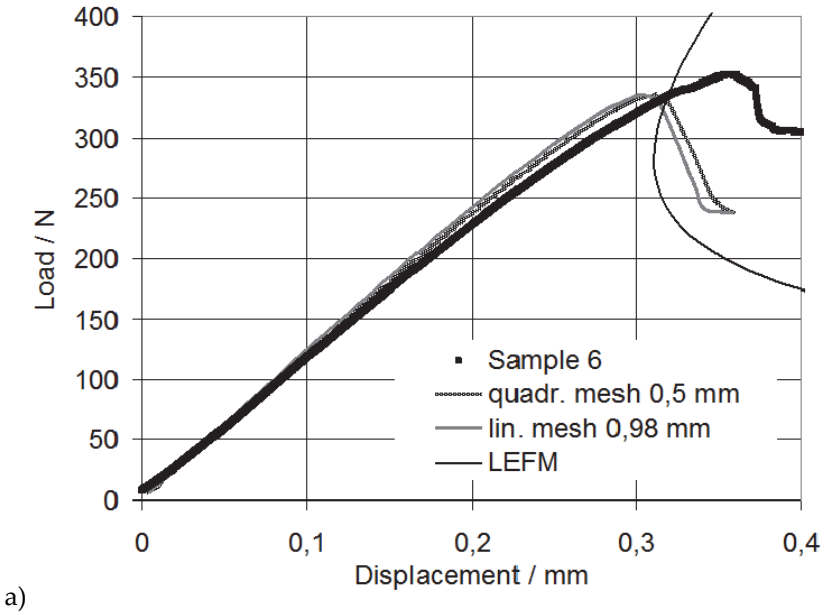

a)

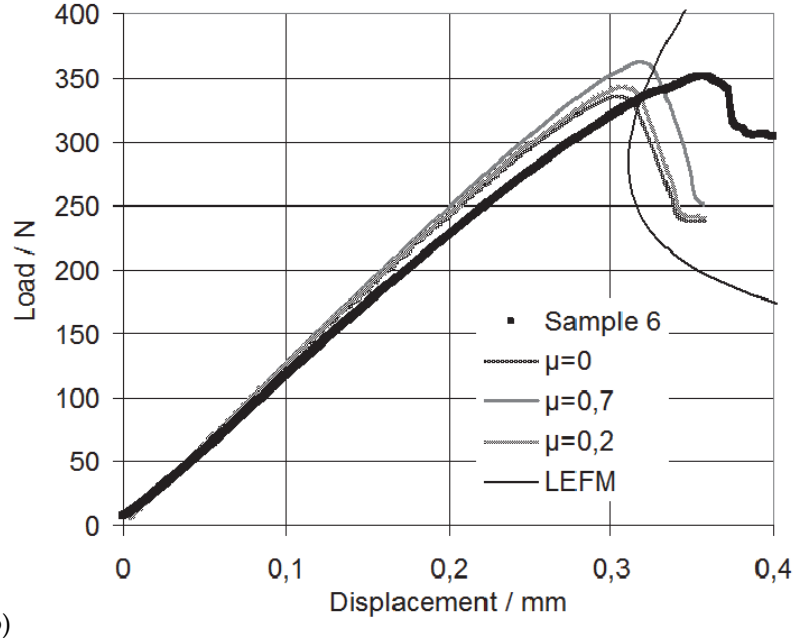

b)

Figure 52: FEA-parameter studies for ENF-test of sample 6 with a=12.7 mm: element formulation and size (a), coefficient of friction (b). The crack propagation curves from LEFM were calculated for E = 43.4 GPa and G_{IIc} = 0.32 N/mm.

Figure 53 a and b are presenting the normalized load-deflection curves from FEA and experiment for representative samples from plate PH1991_ND and PH1879_D. The sample numbers and initial crack lengths are indicated in the diagrams. The samples from plate Ph1879_D were taken from non-delaminated areas in order to compare the behaviour with samples from standard material PH1991_ND. The FEAs were performed with the average G_{Ic} values of plate PH1991_ND and PH1879_D. That is

0.31 N/mm and respectively 0.35 N/mm, compare chapter 6.1.4.2. The stiffness and critical load points from FEA and experiment are in rather good agreement. The critical load points for crack initiation were defined in chapter 6.1.4.2 as the first clear kinking of the experimental load-deflection curves. Those load points were found to correlate with the crack propagation curve from LEFM and with the maximum loads from FEA also. The FEA shows a clear load drop after reaching maximum load for samples with shorter initial crack length (samples 3, 6 and 10). In contrast, the experimental curves show a plateau or even an increase in load after crack initiation. The load-deflection curves from FEA show a plateau only for long initial crack lengths (sample 4 and 13). The plateau in the load-deflection curves is caused by the interlaminar crack getting closer to the central load introduction. The interlaminar crack is compressed due the central load pin and further crack propagation is hindered.

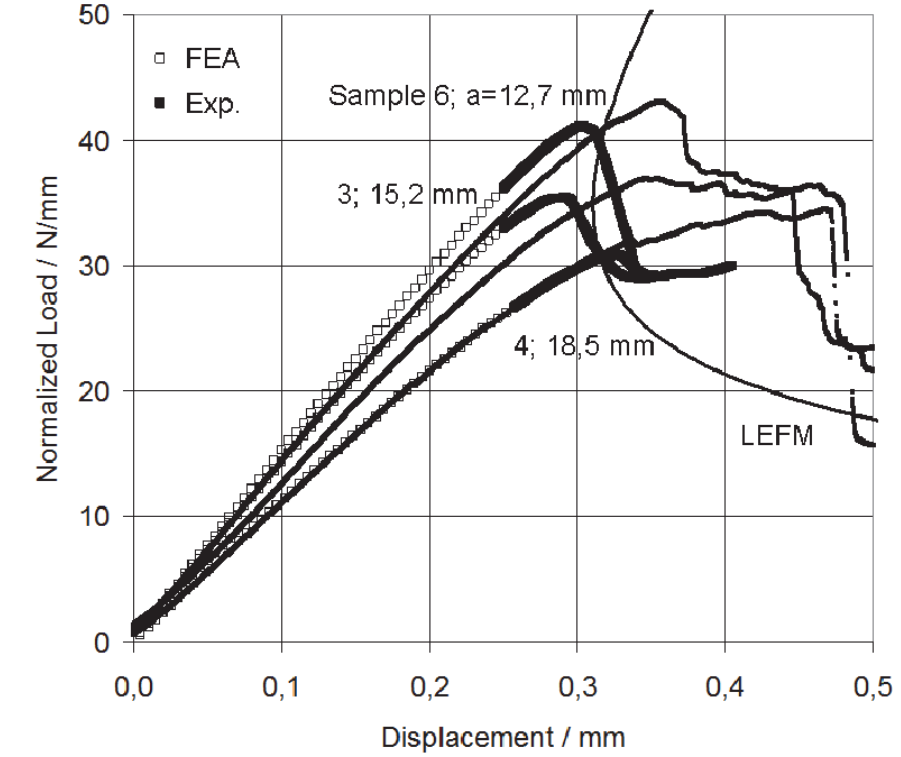

a)

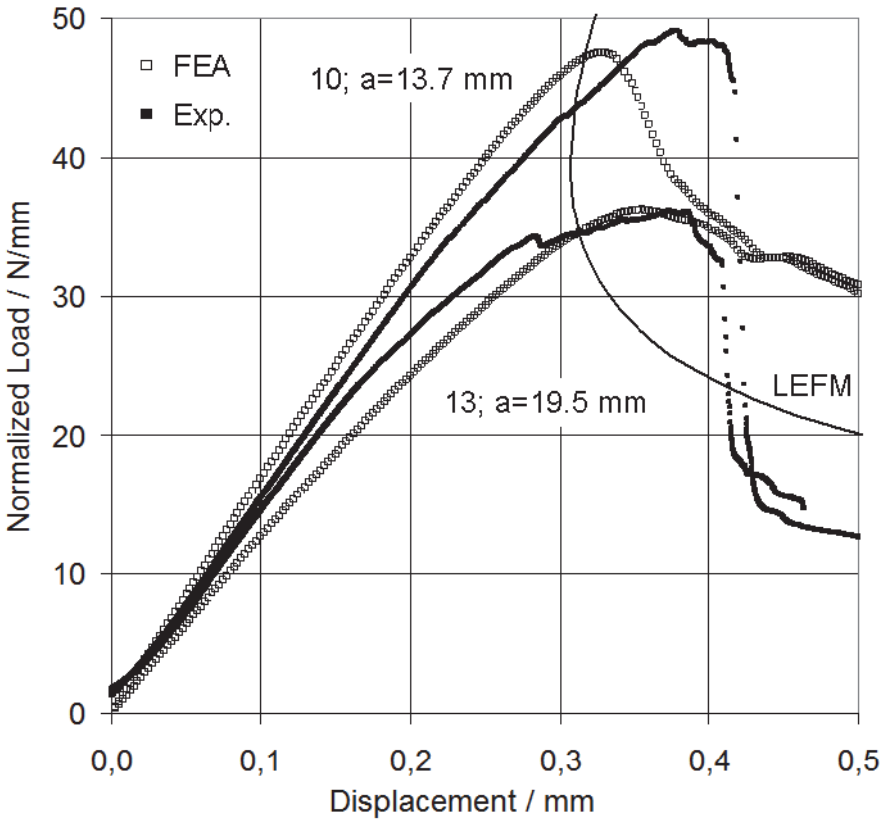

b)

Figure 53: Crack propagation curve from LEFM and load-displacement curves from FEA and experiment; samples from plate PH1991_ND (G_{IIc} = 0.31 N/mm) (a) and PH1879_D (G_{IIC} = 0.35 N/mm) (b).

In the next step the modelling approach was used to describe the load-deflection behaviour of an ENF sample with crack offset. After sawing, sample 2 from plate PH1991_ND showed a distinct crack offset of 0.9 mm from the midplane, see Figure 58 c. Therefore, sample 2 was not used to evaluate the G_{IIc} but it was used to validate the FE-approach. Figure 54 shows a comparison of the FE-results with and without crack offset and the experimental load-displacement curve. The FEA yields a comparable stiffness and maximum load value, taking the crack offset into account.

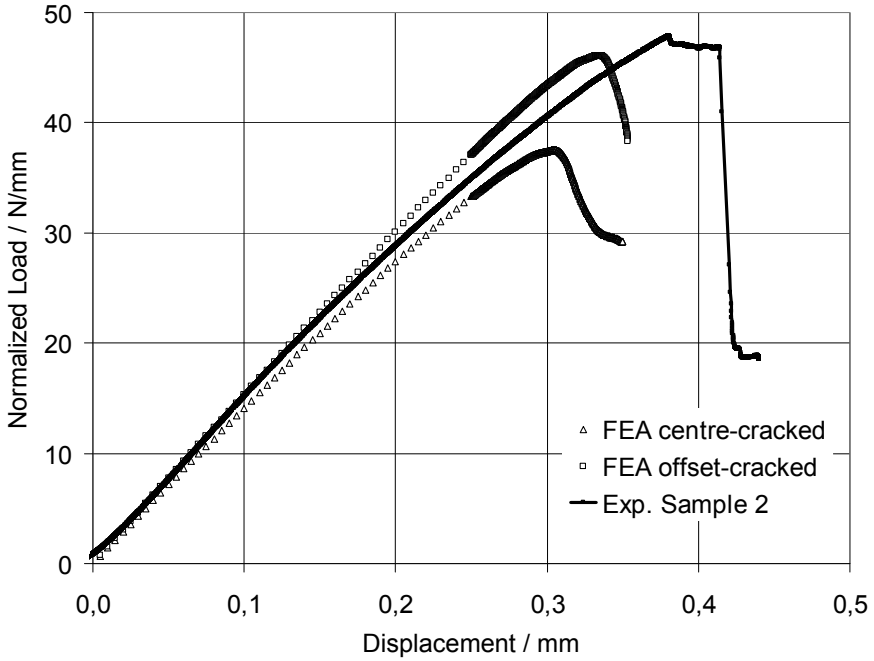

Figure 54: Load-displacement curves from experiment and FEA for an ENF-sample with 0.9 mm crack-offset from midplane, a = 14.2 mm, d = 4.92 mm.

Further, the FE-models were extended to analyse additionally bending failure of ENF samples. The bending failure was modelled as it was described for long beam bending samples of siliconized C/C-SiC in chapter 6.2.1. FEAs of non-precracked bending samples with L/d = 10 were performed to adjust the failure parameters for desiliconized C/C-SiC material. Figure 55 shows the FE-results in comparison to a representative experimental load-deflection curve. The FE-set-up is equivalent to chapter 6.2.1. The maximum stress value was selected accordingly to the tensile strength of the desiliconized material which is 92.2 MPa +/- 15 MPa, see Figure 15 b. The translaminar G_{Ic} was set to 3.5 N/mm, which is two times the WOF of desiliconized C/C-SiC [53]. The partial bilinear analysis in Figure 55 shows good agreement with the experimental curve. A linear elastic analysis was performed additionally with a maximum stress value of 105 MPa. The increase of 13 MPa was chosen in correlation to Figure 48 b in chapter 6.3.3, demonstrating that the non-linear analysis causes a stress reduction of about 13 MPa compared to the linear elastic analysis at a true stress level of 92 MPa. So it was assumed that an increase of maximum stress by 13 MPa for the linear analysis would compensate for the non-

linear effects. Indeed, Figure 55 shows that the maximum load of the linear elastic analysis agrees with the non-linear analysis. The overall behaviour of the linear elastic and bilinear FEA is comparable. The resulting theoretical bending strength of the bilinear analysis is 156.3 MPa. The linear elastic analysis lies slightly higher with 158.3 MPa. The average 3-point bending strength of desiliconized C/C-SiC was measured to be 140.3 MPa for a L/d-ratio of 10. The 4-point bending strength was determined to be 163.5 MPa, see Figure 15 b. Considering the variations in experimental bending strength, the bilinear as well as the linear elastic FEA predict the overall bending strength with satisfying accuracy. In the following, only linear elastic analyses of the ENF test were performed. Interlaminar and translaminar bending failure were included. Debonding starts at the validated maximum tensile stress value of 105 MPa with a translaminar G_{Ic} of 3.5 N/mm. The linear elastic analysis in combination with interlaminar cohesive zone modelling was preferred because of more stable solutions in contrast to a combination of bilinear in-plane and interlaminar cohesive zone analysis. Due to the only slight non-linear behaviour in 0/90° direction the linear elastic modelling with increased σ_{max} is a good approximation for that orientation. The results from linear elastic FEA and LEFM can be compared directly.

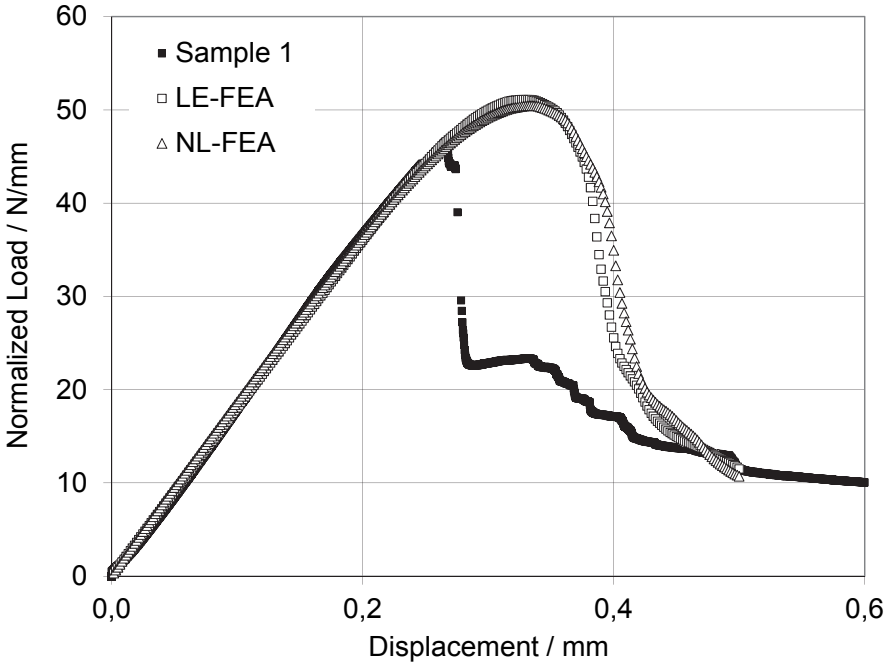

Figure 55: Load-deflection curves from desiliconized C/C-SiC, plate PH1991_ND, with L/d = 10: experimental, linear elastic and partial bilinear FE-results.

Figure 56 a shows the load-displacement curve for sample 6 with cohesive zone modelling for interlaminar shear and bending failure. First, Cohesive Zone Elements for bending failure were introduced at the locations of highest normal stresses only. Those are: the lower side in the middle of the sample (25 mm) and the lower side and midplane at the delamination front (12.7 mm), see red areas from normal stress

distribution of image 3 in Figure 56 d. The FE-model was used for multiple crack lengths by simply adapting the region of frictionless contact. The FEA is predicting full interlaminar shear failure to the middle of the sample, followed by bending failure at the same location (25 mm). The experimental results for sample 6 showed, however, that bending failure occurred at the lower side at the initial crack length of 12.7 mm; see Figure 32 in chapter 6.1.4.2. Therefore additional vertical Cohesive Zone Elements were activated to allow bending failure at differing locations (12.7, 14.2 or 18.5 mm). Since the normal stress distribution is changing with shear crack propagation, the elemental mean stress, see Figure 56 b, was investigated on the tensile side of the ENF sample at the locations of vertical cohesive zones (12.7, 14.2, 18.5 and 25 mm).

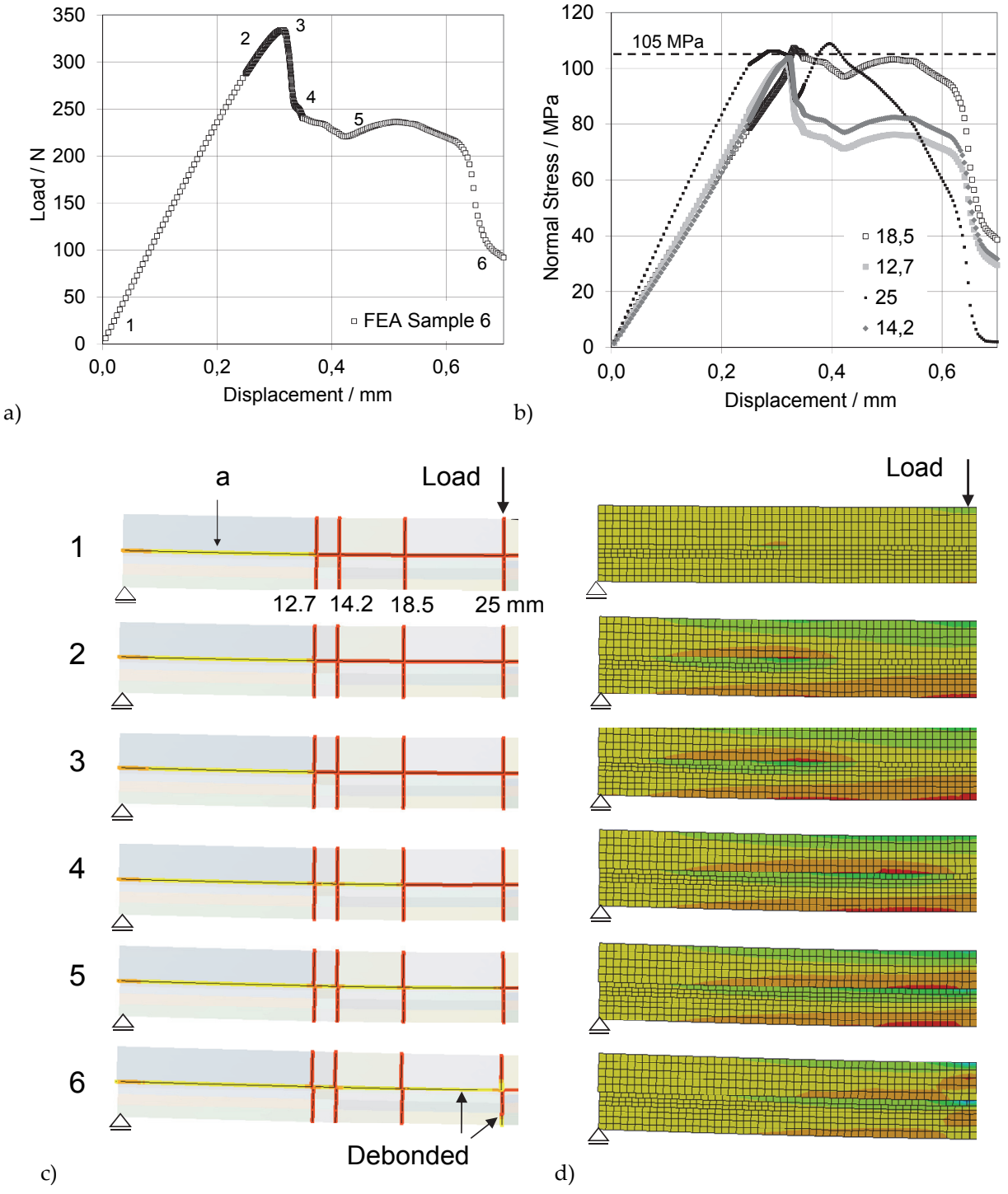

Figure 56: Load-displacement curve for sample 6 from FEA with shear and bending failure model (a), normal stresses at selected locations (12.7-25 mm) on lower side (b), cohesive zone model of pre-cracked section (c) and longitudinal stress distribution (d); interlaminar shear failure and subsequent tensile failure at the centre (25 mm) is observed.

Figure 56 b shows that the highest normal stresses appear initially at the middle of the sample. Shear crack propagation starts at a displacement of about 0.3 mm (Figure 56

a). At this point of displacement, the normal stress at the middle of the beam has already reached the maximum stress criterion of 105 MPa. Due to the shear crack propagation the load drops and therewith the normal stresses decrease at 12.7, 14.2 and 25 mm. At about 3.5 mm of displacement the shear crack has reached an extension of about 18.5 mm (image 4, Figure 56 c and d) and the load deflection curve shows a plateau (Figure 56 a). The normal stress at the location of 18.5 mm exceeds the maximum stress criterion due to the shear crack reaching 18.5 mm. However, the stress at 18.5 mm decreases again due to further shear crack propagation. In that way the normal stress at 25 mm starts to increase until the shear crack reaches the centre of the sample (image 5, Figure 56 c and d). With the shear crack reaching the middle of the sample the normal stress criterion is exceeded and ultimate bending failure starts at the centre (25 mm) on the lower side of the sample. Simultaneously bending failure is observed growing upwards from the interlaminar crack (image 6, Figure 56 c and d).

In chapter 7.3.2 the FE-models for bending samples with manufacturing defects are going to be equipped with horizontal CZEs and vertical CZEs, too. The exemplary FEA of sample 6 showed that the regions of highest initial normal stresses are at the middle of the beam and at the delamination front, see Figure 56 d, image 3. Only at those locations vertical CZEs are going to be implemented in order to predict a possible first bending failure in chapter 7.3.2.

The main differences between the experimental and numerical results for ENF-sample 6 are: the experimental investigations showed that directly after shear crack propagation bending failure occurred. The shear crack was not reaching the centre of the sample. Bending failure occurred roughly at the initial crack length, see Figure 32 in chapter 6.1.4.2.

In the FEA, the shear crack is reaching the centre of the sample first and then bending failure occurs in the middle of the sample. It is not yet clear why bending failure occurred roughly at the initial crack length in experiment. Nevertheless FEA showed that the differences in normal stresses at the lower beam side are rather small. One explanation for the deviating failure location in experiment is the sawed pre-crack. Although, aluminum plates were inserted it cannot be excluded that the compression of the pre-cracked region is leading to additional bending of the lower cantilever beam. In that way bending stresses would be increased at the initial crack length. A second explanation is the increase of G_{IIc} with crack propagation. Figure 33 in chapter 6.1.4.2. has been demonstrating that the initiation G_{IIc} increases with increasing initial crack length. The determination of G_{IIc} with propagating crack length was not possible. An increase of G_{IIc} during crack propagation would prevent the crack to propagate below the central load point, as observed in Figure 32, and therefore bending failure would be promoted closer to the initial crack front.

In spite of the differences in crack propagation, Figure 57 demonstrates that the FEA with shear and bending failure zones is closely reproducing the stiffness and initiation load points for the exemplary experimental ENF curves of sample 4 and 6. Because of the differences in crack propagation the FEA is showing more pronounced load drops due to shear failure. Nevertheless the underlying behaviour and critical load points from FEA and experiment are equivalent: first shear failure occurs followed by bending failure starting on the lower side of the sample. This behaviour was shown for sample 6 in Figure 32 and Figure 56 c. The failure progression of sample 4 was similar.

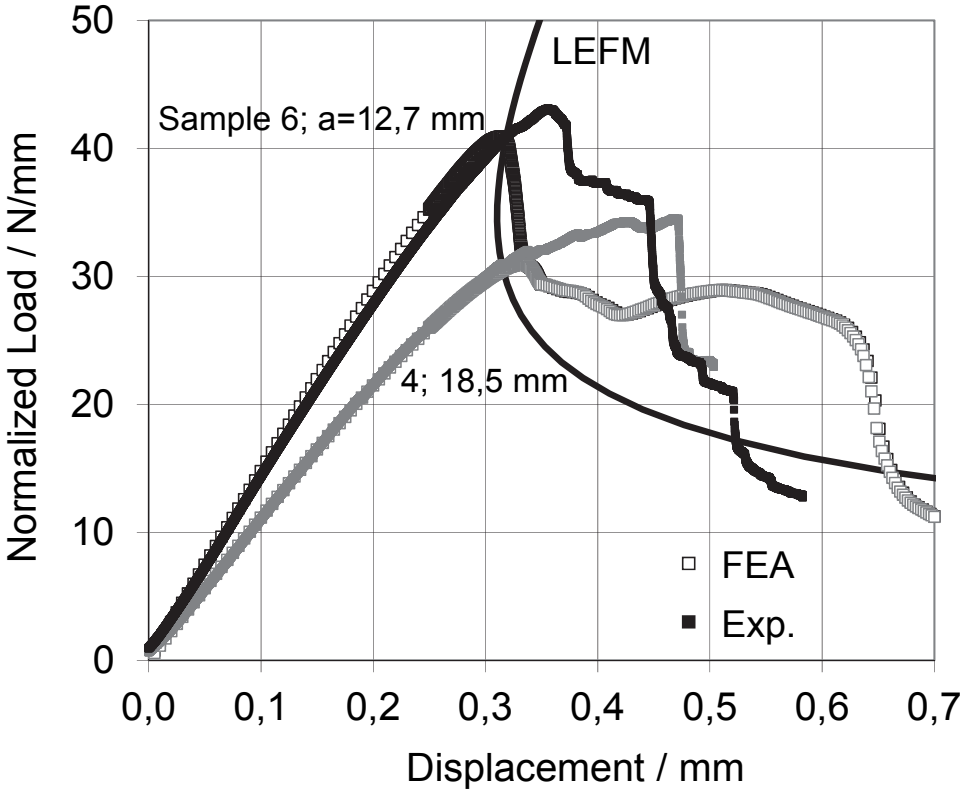

Figure 57: Normalized load–deflection curves from experiment, FEA with shear and bending failure model and crack propagation curve from LEFM.

Finally, the combined shear and bending failure models were used for sample 2 with a crack-offset of 0.9 mm. The experimental bending strength for sample 2, following beam theory, is 149 MPa. That means in spite of the pre-crack, the average bending strength of the desiliconized standard material was reached (140.3 MPa for L/d = 10; 163.5 MPa for 4-point bending, see Figure 15 b). The bending strength of the linear elastic FE-model without pre-crack was 158.3 MPa, see Figure 55. Although, sample 2 is quite close to the strength of the standard bending sample the shear failure load is well reproduced by FEA, compare Figure 58 a. The main differences are again: FEA predicts full delamination to the centre of the sample with a strong first load drop. In contrast, the experimental curve shows a load plateau because of slight interlaminar crack propagation followed by a steep load drop due to bending failure on the lower

side of the sample. The bending failure on the lower side is also predicted by FEA but again in the middle of the sample and not at the pre-crack, like in experiment (see images 1-3, Figure 58 b). The comparison of FE- and experimental results for sample 2 shows that even for a short crack length with offset from the midplane the stiffness and maximum load point are predicted by the combined shear and bending failure models with less than 10% of deviation.

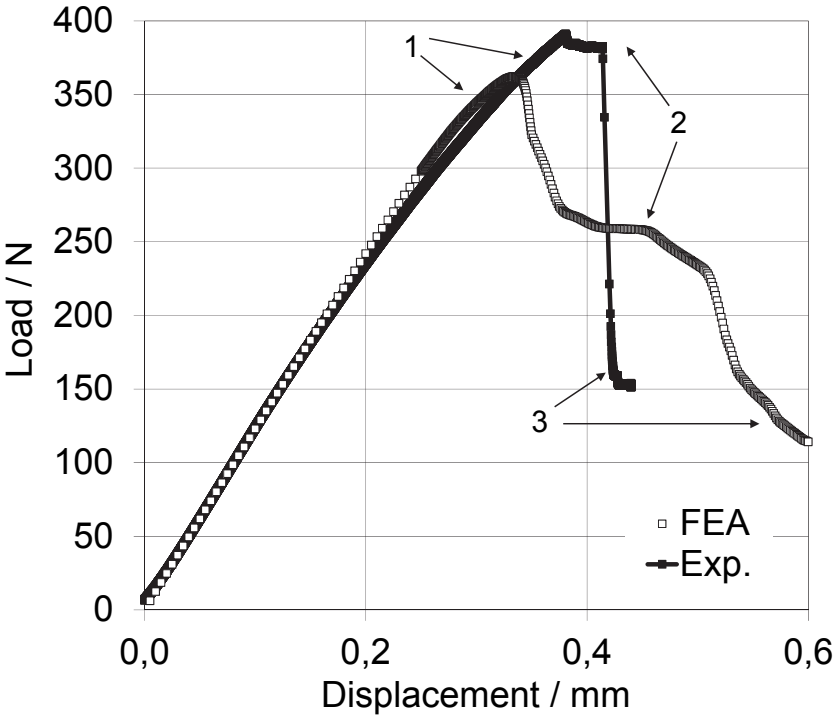

a)

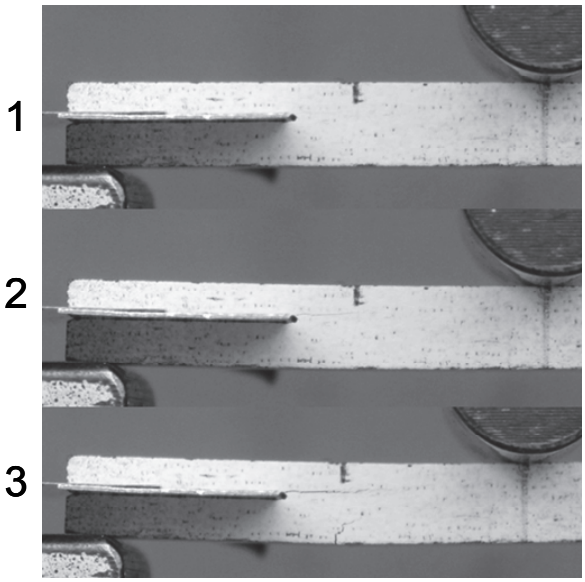

b)

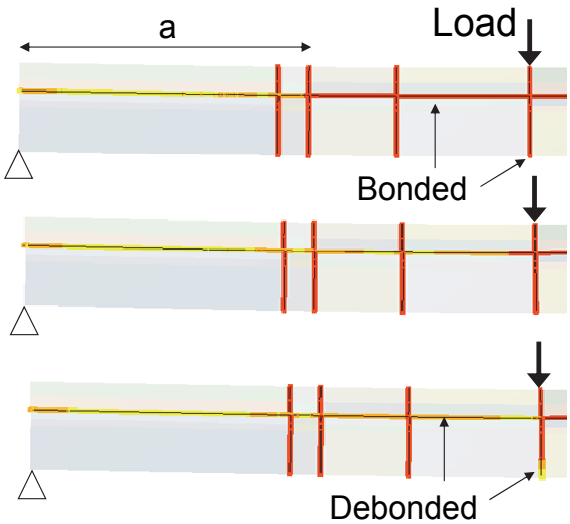

c)

Figure 58: Load-displacement curves from experiment and combined shear/bending failure FE-model for sample 2 with crack-offset (a), images from bending test (b) and cohesive zone model (c) for load points 1-3.

7. Mechanical behaviour of C/C-SiC with manufacturing defects

7.1 C/C-SiC with free Silicon

The present chapter is comparing the mechanical properties from standard C/C-SiC material, plate PH1991_ND (chapter 6.1.1), with results from plate PH1879_D with large areas of free silicon. The plates were tested in siliconized state.

7.1.1 *Results from NDT – sample taking*

Figure 59 is showing the ultrasonic test result of plate PH1879_D in C/C state and the locations and geometries of investigated bending samples in C/C-SiC state. The C/C state is shown because the delamination in C/C state indicates most clearly the areas of free silicon in C/C-SiC state. Because of the ultrasound results of plate PH1879_D in the different processing states (Figure 11 in chapter 5.2), it can be assumed that the delaminated regions in C/C state are completely filled with free silicon after siliconization. Mainly short-beam bending tests with L/d-ratio of 5 were performed. Additionally, the samples s8, s10 and s24 were tested with L/d=2.5. The very short L/d-ratio was introduced to investigate the behaviour at increased interlaminar shear stresses. Six samples were tested with L/d=15 as indicated in Figure 59. Those samples were used to evaluate the in-plane behaviour with reduced effects due to interlaminar shear deformation. The samples from plate PH1879_D were taken from locations where standard material and also from regions where free silicon was expected. Therefore it was also expected that variations of the mechanical properties are observed from the left to right side of the plate.

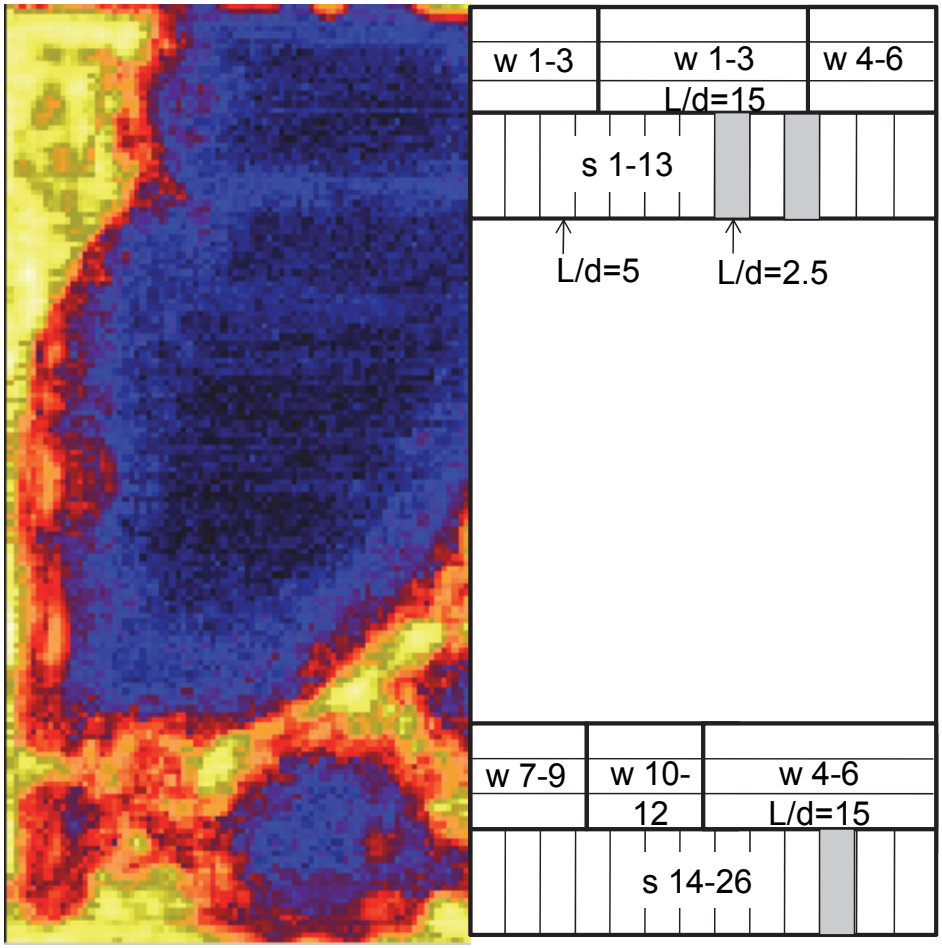

Figure 59: US-result from PH1879_D in C/C state and samples taken in C/C-SiC state.

Figure 60 compares the open porosity and density of standard material with the samples s1-26 taken from plate PH1879_D. The open porosity of plate PH1879_D shows strong scattering. In average, however, it is corresponding to plate PH1991_ND, which also shows a large standard deviation due to the uncertainties caused by the Archimedes porosity measurement. The density of the samples s1-13 and s14-26 from plate PH1879_D is increasing from the left to the right border. This result agrees with the US-result: on the left side ultrasound indicates standard material; the right part shows strong delaminations in C/C state, i.e. free silicon in siliconized state.

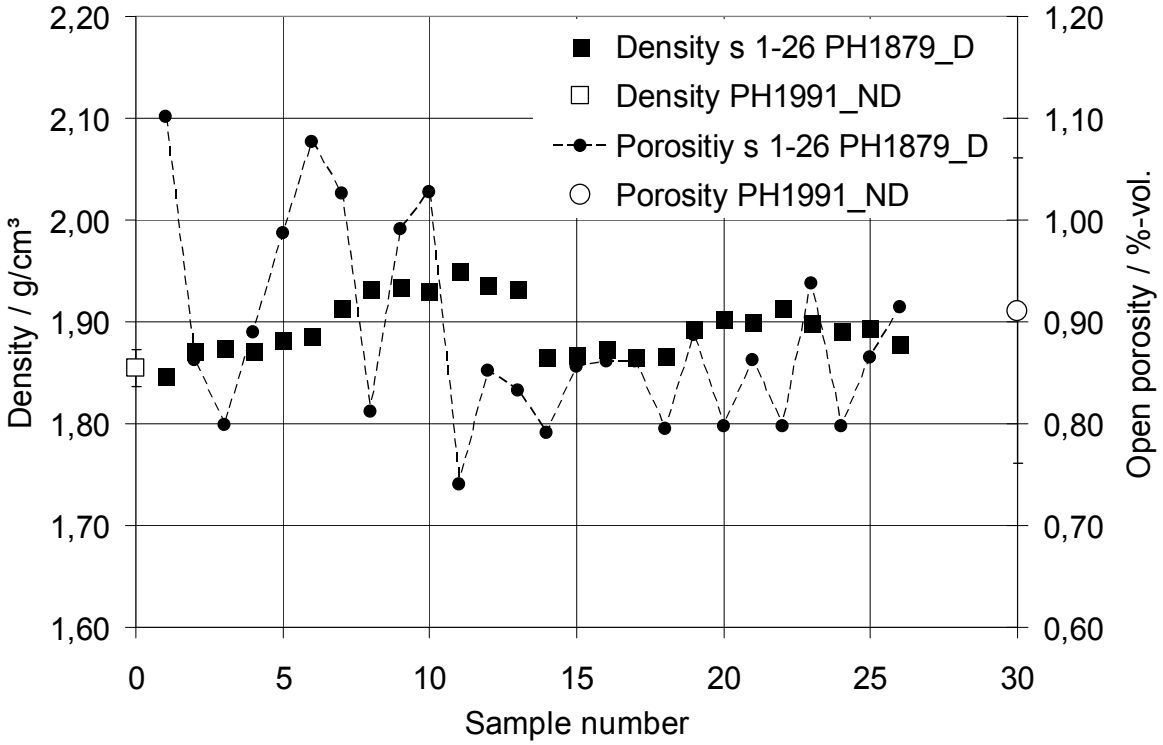

Figure 60: Density and open porosity from standard plate PH1991_ND and plate PH1879_D with free silicon.

7.1.2 *Results from bending test*

Figure 61 and Figure 62 are showing the short-beam bending strength (L/d=5) and the density of samples s1-13 and s14-26. That is from the left to the right border of the half-plate PH1879_D. The bending strength is slightly decreasing with increasing density for the samples s1-13. In contrast, the samples s14-26 show rather an increase of strength with density. Overall there is no clear tendency correlating bending strength with density. The side views of samples s1-13 and s14-26 in Figure 61 b and Figure 62 b confirm that the increase of density from the left to the right side of plate PH1879_D is caused by regions of free silicon. The side views show multiple thin bright layers of free silicon. The samples from the upper left side (s1-4) e.g. show less free silicon. This was also predicted by US in Figure 59.

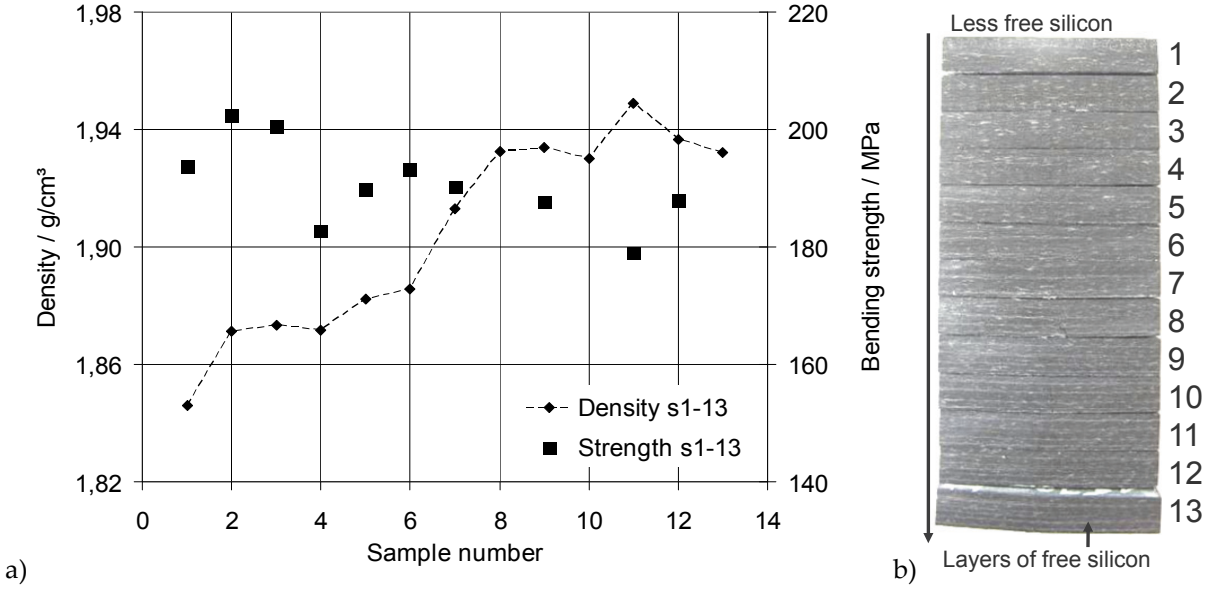

Figure 61: Bending strength and density (a), side view (b) for samples s1-13.

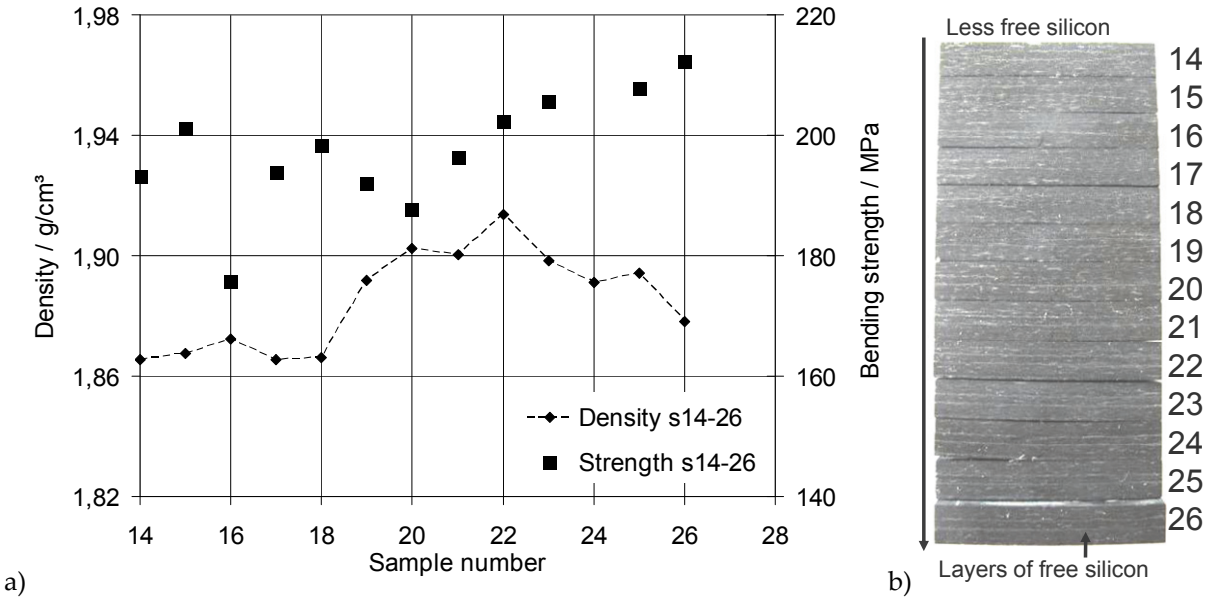

Figure 62: Bending strength and density (a), side view (b) for samples s14-26.

Figure 63 shows the comparison of the averaged mechanical properties of plate PH1991_ND and PH1879_D. The following samples of plate PH1879_D were equipped with strain gauges: w1-12 (L/d = 5) and w1-6 (L/d = 15). Those samples were used for the evaluation of elastic properties in Figure 63 b and failure strains in Figure 63 c. The comparison of bending strengths at varying L/d-ratios in Figure 63 a shows average values from horizontal as well as from vertical sample-sets. In general, plate PH1879_D shows similar mechanical behaviour as plate PH1991_ND. The bending strength of plate PH1879_D is also decreasing with decreasing L/d-ratio. Nevertheless, the bending strength of PH1879_D is about 25 MPa lower at all L/d-ratios. The

standard deviation of bending strength and failure strain is increased for plate PH1879_D, which indicates a stronger scattering of results. The Young's moduli of plate PH1879_D are again slightly lower than plate PH1991_ND. The interlaminar shear modulus, however, matches to plate PH1991_ND. The determination of shear modulus followed chapter 6.1.1. The failure strains of plate PH1879_D are even a little higher than from plate PH1991_ND (Figure 63 c).

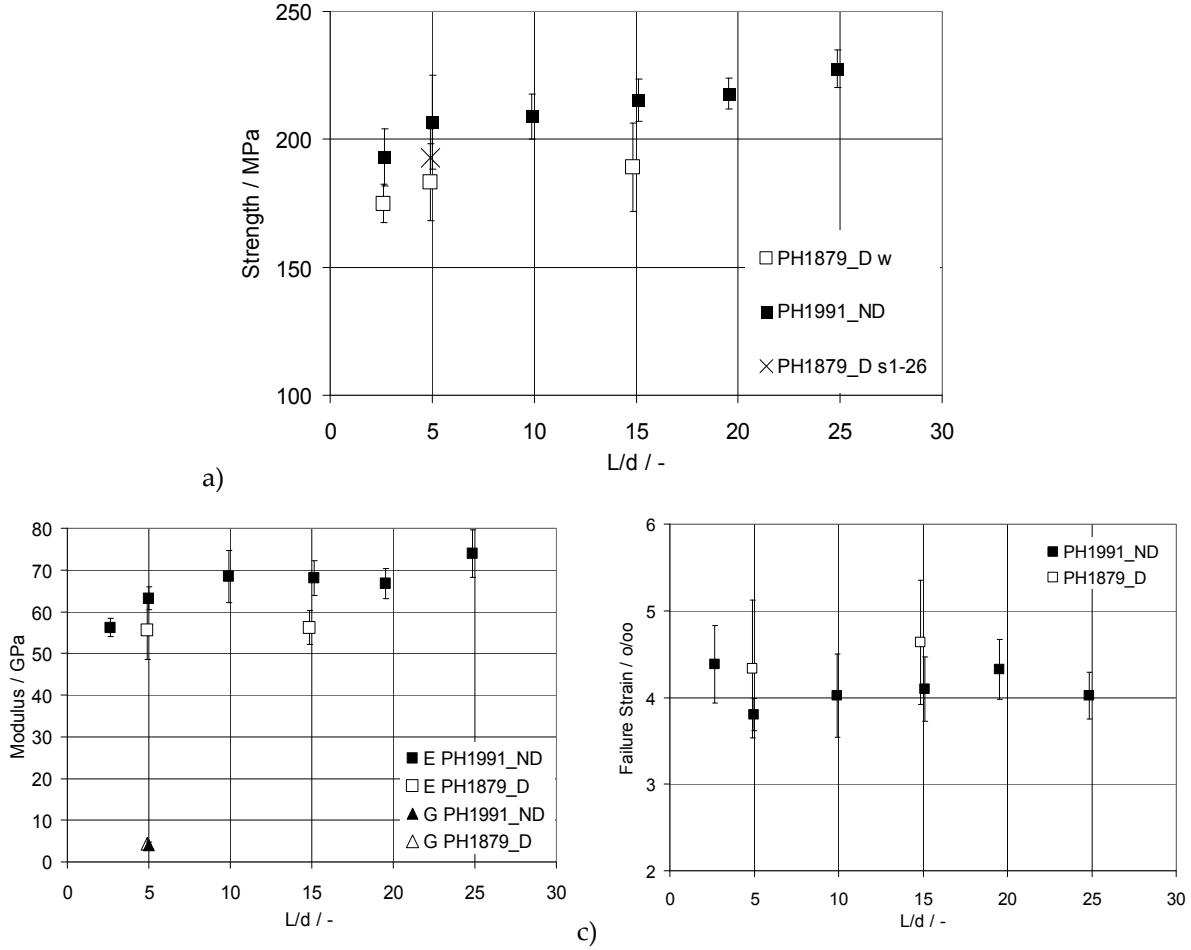

Figure 63: Comparison of mechanical properties from plate PH1879_D and PH1991_ND, bending strength (a); results from strain gauge measurements on w1-12 (L/d = 5) and w1-6 (L/d = 15): moduli (b) and failure strains (c).

Overall, plate PH1879_D shows slightly decreased in-plane strength and stiffness. The interlaminar properties, however, did not show an alteration due to the layers of free silicon. Even for L/d = 2.5 none of the samples showed interlaminar failure. The interlaminar shear modulus also corresponds to plate PH1991_ND. Therefore it can be stated that free silicon did not affect the interlaminar properties.

Figure 61 and Figure 62 a did not indicate a clear correlation of density, bending strength and location within plate PH1879_D. Figure 64 is comparing now the short-beam bending strength with the density of the samples independently of the location

taken from plate PH1879_D. The diagram shows that the short-beam bending strength is slightly decreasing with increasing density, e.g. due to the amount of free silicon.

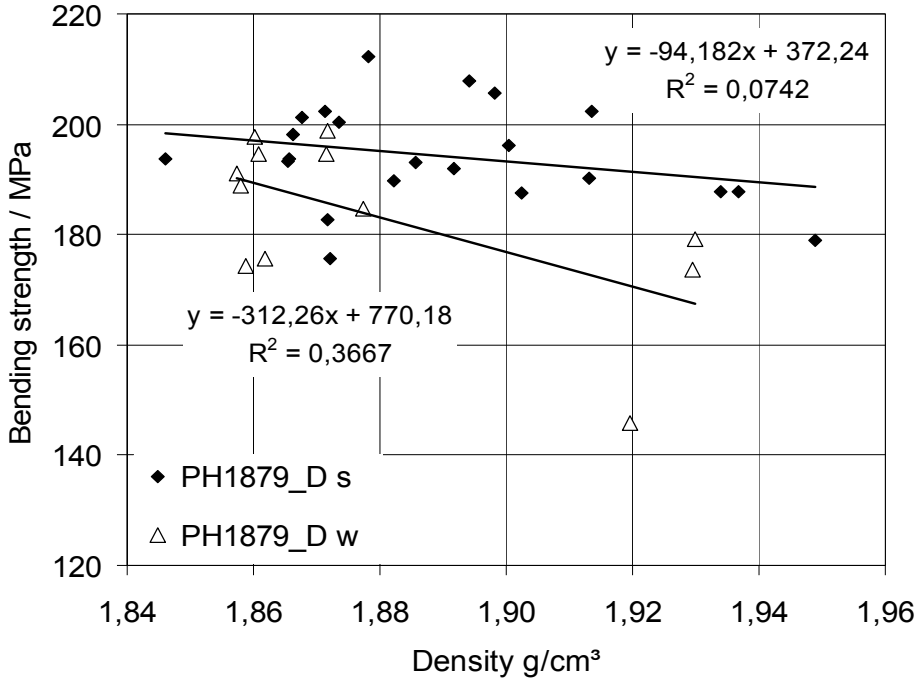

Figure 64: Short-beam bending strength, L/d = 5, from vertical (s) and horizontal (w) samples from plate PH1879_D plotted over the density.

However, the difference of about 25 MPa, ca. 12 %, between the average short-beam bending strength (L/d=5) of plate PH1991_ND and plate PH1879_D, see Figure 63 a, is rather small. The difference is even smaller for the vertical samples s1-26 of plate PH1879_D. Those slight differences in strength might also be caused by grinding of the sample surfaces. It cannot be stated that the layers of free silicon lead to a strong embrittlement of the surrounding material. The failure strains of plate PH1879_D, see Figure 63 c, are even higher than for plate PH1991_ND. Nevertheless, it has been shown that free silicon has a slight impact on the density and bending strength, see Figure 61, Figure 62 and Figure 64, and on the scattering of the results, see Figure 63 a-c.

7.2 FE-modelling based on CT-data for C/C-SiC with delaminations

Samples from a siliconized reject-plate with delaminations, Reject cut-off_D (see also Table 3 in chapter 5.1), were tested in 3-point bending. In the following, two modelling approaches are evaluated to predict the mechanical behaviour of siliconized and desiliconized C/C-SiC with interlaminar defects. The approach, described in this

chapter, is using directly the 3D micro-CT results for the generation of FE-meshes. The second approach, chapter 7.3, is based on measuring the individual defect sizes and locations from 3D-CT data and designing equivalent 2D-FE-models. Because of the complexity of meshing and FE-model generation the first approach was performed without failure models. Only the stiffness and local stress concentrations were evaluated in this chapter. The second approach with 2D-failure models was used to predict stiffness and failure loads by Cohesive Zone Elements.

7.2.1 *Experimental Results*

7.2.1.1 Results from NDT

The investigated reject C/C-SiC plate showed broad delaminations after siliconization which were confirmed by ultrasonic inspection in transmission mode, seeFigure 65. 3-point bending samples of 35 x 10 x 5 mm³ were cut out of the plate, named Reject cut-off_D. Four samples with minor pores were cut out in horizontal direction for preliminary investigations. They showed a bending strength of 176 ± 9 MPa. For the numerical and experimental investigations presented below the samples in vertical orientation were used.

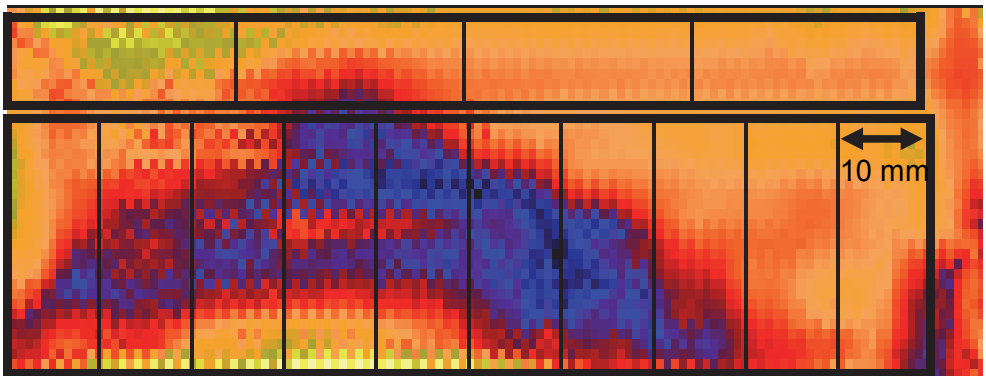

Figure 65: Ultrasonic result and samples taken from C/C-SiC reject plate, Reject cut-off_D.

Since the delaminations were also extended close to the top of the plate some of the samples showed defects on the grinded surfaces. Those were rejected and only 6 samples without surface defects were investigated. At first, a CT-scan was examined to determine the extent of delamination in the respective samples, see Figure 66. The samples were scanned with a voxel size of about 38 µm. The results from CT-analysis were also used for the generation of FE-models as will be shown in chapter 7.2.2. Samples 1 to 3 show some minor pores. In contrast sample 4 shows one larger delamination and samples 5 and 6 even multiple delaminations in different layers.

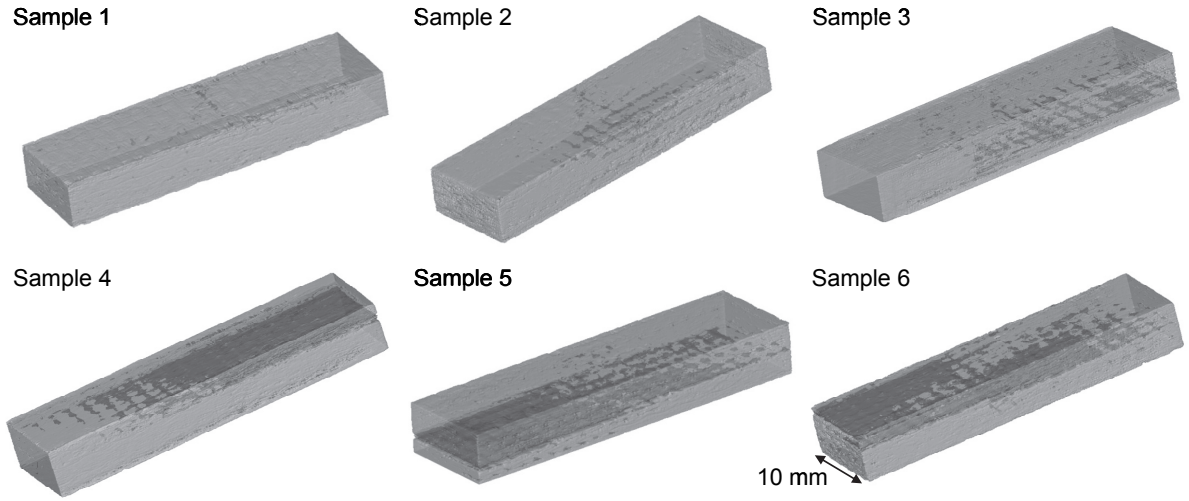

Figure 66: 3D-visualisation of samples 1 to 6 from CT-data with interlaminar defects (dark regions).

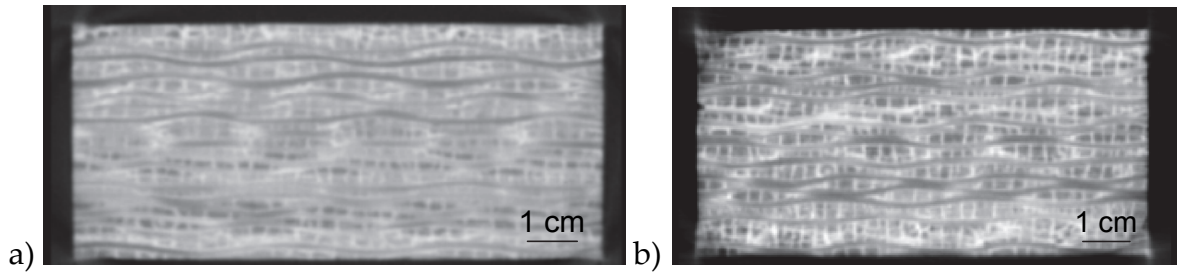

Figure 67: CT cross sections from sample 1 (a) and 3 (b).

Additionally, the density and open porosity of the selected samples were investigated, see Table 9. Corresponding to the CT-results, the samples 4-6 show increased open porosities. It was not expected that measuring the open porosity by Archimedes method is an exact method to determine quantitatively the amount of delamination. The uncertainties, due to water loss from larger pores, are too high. Nevertheless it gives a qualitative estimation.

Figure 67 a and b show microstructures of sample 1 and 3. The homogenous bright colour of sample 1 indicates a strong conversion of C-fibres to SiC, leading to embrittlement and a reduced failure load. Overall, the density of samples 1-6 was rather high compared to the standard plate PH1991_ND, see Figure 60 and Table 9. A higher density might indicate layers of free silicon, as explained in chapter 7.1. In this case, however, the higher density indicates the increased SiC content, which is rather homogenously distributed as shown in Figure 67 a.

Table 9: Geometries, densities and open porosities of samples 1-6 from Reject cut-off_D.

Sample	Length / mm	Width / mm	Height / mm	Open porosity / %	Density / g/cm³
1	35.16	10.02	5.00	1.72	2.03
2	35.17	10.03	5.00	1.81	2.00
3	35.25	10.01	5.01	1.97	1.99
4	35.13	10.00	5.02	2.14	1.98
5	35.23	10.02	5.00	3.20	1.99
6	35.23	9.97	5.00	2.51	2.00

7.2.1.2 Results from short-beam bending

Finally, the samples 1-6 were tested in short-beam bending set-up with L/d = 5. Figure 68 is summarizing the load-deflection curves. It has to be noted here that the curves were not offset-corrected because it was not possible to differentiate between loading effects due to the supports or due to the material and its defects. The variation in failure load cannot be explained by the CT-results and by the varying amount of defects in Figure 66. The samples 1, 2 and 3 e.g. showed similar amounts of small pores. Nevertheless failure occurred at strongly varying loads of 250, 440 and 975 N.

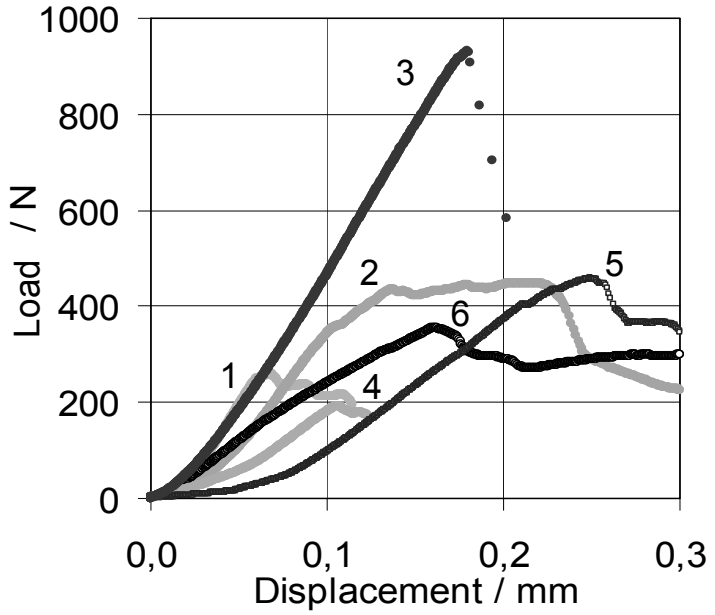

Figure 68: Load-deflection curves from short-beam bending test of Reject cut-off_D.

The variations cannot be explained by the amount of defects but by the embrittlement due to microstructural effects as shown in Figure 67 a and b for sample 1 and 3. The maximum strength of samples 1-6 was reached for sample 3 with 146 MPa. Sample 3 showed only small amounts of defects in Figure 66 and the microstructure in Figure 67 b indicates a relatively low SiC content, i.e. a large amount of intact fibres.

Because of the variations in SiC content it is not going to be possible to predict the experimental failure loads by macroscopic FE-simulations. The stiffness of samples 1-6, however, depends mainly on the extent of delamination, see Figure 66, and is going to be compared with FE-results in the following chapter.

7.2.2 *FE-models from 3D-CT data – real structure modelling*

Starting from the CT-data of the six C/C-SiC samples, see Figure 66, real structure FE-models were generated, using the software Mimics 12.3 from Materialise Co.[54]. The extraction of sample and defect surfaces was performed by grey scale segmentation. After segmentation the sample surface, including the defect surfaces, was meshed with triangle elements. Subsequently the surface-mesh was remeshed to reduce the number of elements and to improve element quality and shape. The minimal defect size considered in the FE-models is about 40 μm, which corresponds to the voxel size. The delaminations had a characteristical height of about 70-100 μm.

One significant parameter during remeshing is the allowable geometrical error. The geometrical error determines the accuracy of the surface mesh related to the enclosed material volume and its defects. The allowable geometrical error was varied for sample 5 from 0.02 to 0.1 mm to determine the influence of geometrical error on the model's stiffness. After remeshing a quadratic tetrahedron mesh, based on the surface mesh, was created. This mesh (Figure 69 a) was then imported in ANSYS, where boundary and contact conditions were defined, see Figure 69 b. The displacement was defined on top of the sample in negative z-direction. On the lower side 'compression only supports', as it is called by the ANSYS documentation [44], were defined. 'Compression only support' means that the selected nodes can move in all other directions but not in negative z-direction. The contact was defined as penalty with a coefficient of friction of 0.6. A typical coefficient of friction for C/C-SiC surface pairs is about 0.6-0.7 [5]. The load-displacement curves were evaluated from the reaction forces on the 'compression only supports' and the displacement on top of the sample. Table 10 shows the orthotropic material data, taken from a DLR database, used for linear elastic modelling of the C/C-SiC material. The investigated material was produced from plain weave by RTM-technique, as explained in chapter 5. The properties are similiar to autoclave material, see elastic input data in Table 7. The interlaminar shear modulus G_{xz} was fitted to the experimental load-displacement

curve of sample 1 in Figure 68. Usually an interlaminar modulus G_{xz} of 1.75 GPa is assumed for the RTM material [14]. The best fit was reached here for G_{xz} = 1 GPa.

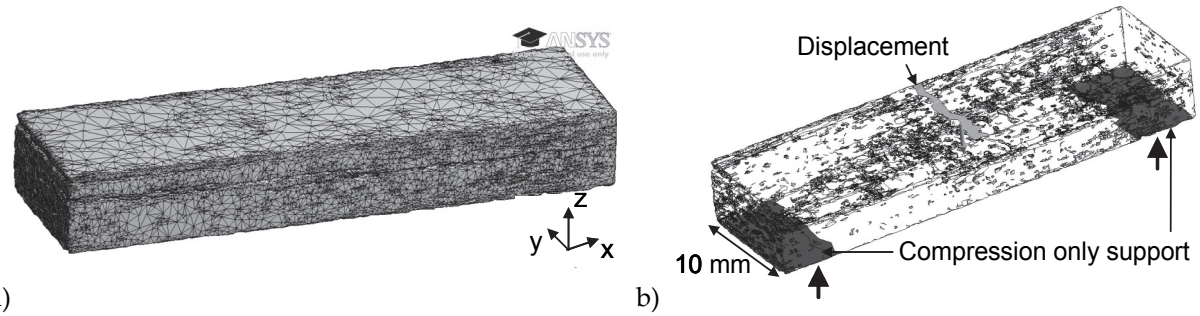

a) b)

Figure 69: FE-mesh (a) and boundary conditions (b) for sample 5.

Table 10: Properties for linear elastic real structure FE-model.

Index	Modulus / GPa	ν
xx	60	-
yy	60	-
zz	25	-
xy	8.9	0.01
yz	8.9	0.1
xz	1 (8.9)[a]	0.1

[a]Theoretical value due to 0/90° symmetry

7.2.3 *FE- and experimental results*

FE-Meshes with allowable geometrical errors of 0.02, 0.04, 0.08 and 0.1 mm were generated to determine the influence of the geometrical error on the simulation results of sample number 5. Figure 70 shows front views of the FE-models of sample 5 for geometrical errors of 0.04, 0.08 and 0.1 mm. A reduction of geometrical details and loss of smaller pores is observed with increasing geometrical error. The number of necessary elements decreases with the reduction of geometrical details, too. Figure 71 a shows the linear decrease of element number with increasing allowable geometrical error.

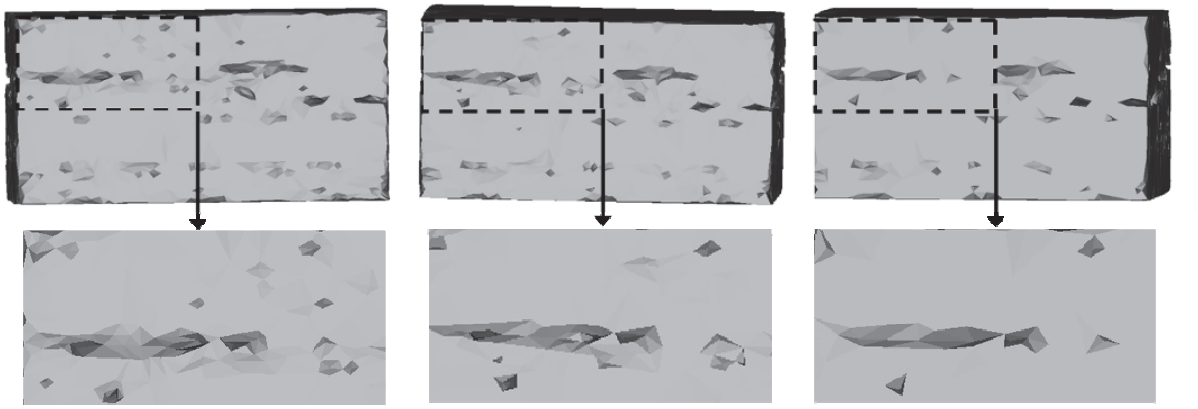

Figure 70: Front view of surface contour for sample 5 with geometrical errors of 0.04, 0.08 and 0.1 mm, from left to right.

In the next step, the effect of geometrical error on the simulation results was investigated. The force reaction of the different FE-meshes was evaluated at a constant displacement of 0.25 mm in z direction. Figure 71 b shows an increase in force reaction, i.e. stiffness, of sample 5 with increasing geometrical error. With increasing geometrical error smaller pores vanish for the FE-modelling, as shown in Figure 70, and the stiffness increases. Finally, a geometrical error of 0.04 mm was selected for the mesh generation of samples 1 to 6. The geometrical error of 0.04 and was found to be a compromise of geometrical accuracy and number of elements.

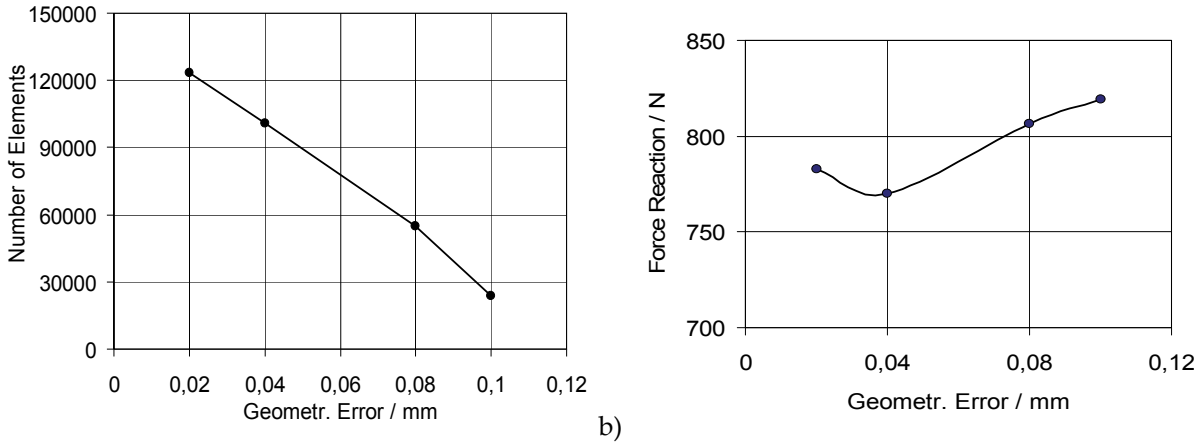

Figure 71: Number of elements (a) and force reaction at 0.25 mm displacement (b) in dependency of geometrical error.

Figure 72 shows the load-displacement curves from FEA for the samples 1 to 6. The relative stiffness of the samples, compared to the experimental load-deflection curves in Figure 68, is well described by the real structure models. The highest stiffness is shown by samples 1-3. The samples 1, 2 and 3 showed minor pores, compare Figure 66. Therefore, the stiffness is comparable to the result of an ideal FEA. Samples 4, 5 and 6 showed different distributions of pores and delaminations, that is why the behaviour is strongly varying. The qualitative behaviour is again predicted by the

FEA. Sample 6 e.g. shows a degressive experimental load-deflection curve in Figure 68. This behaviour is also predicted by the real structure model, but not in the same extent, see Figure 72. In contrast, sample 5 shows a progressive load-deflection curve which is also observable in the corresponding FE-result. In general the FE-simulations show the same trend as the experimental curves but non-linear effects are more distinct in experiment. As described above, failure was not modelled in this case. The FE-simulations were performed up to the failure loads, as determined in experiment, compare Figure 68.

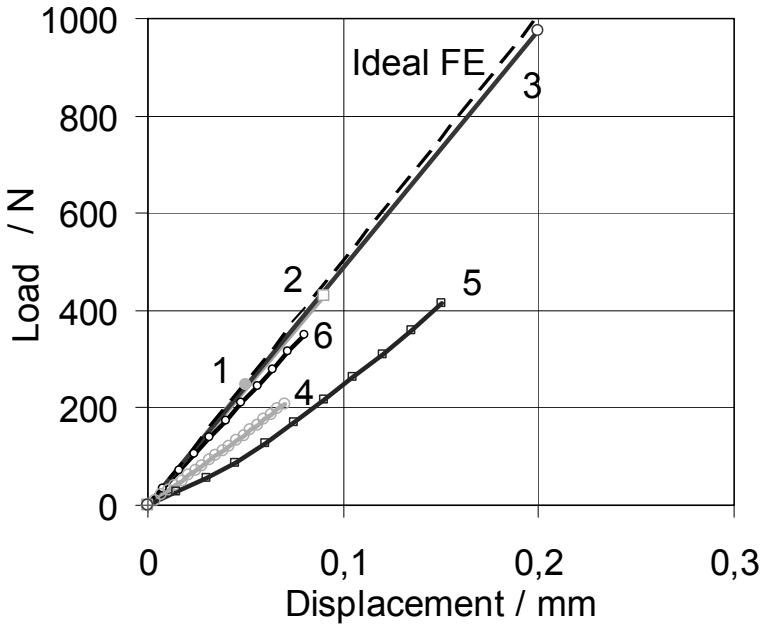

Figure 72: Load-deflection curves of FEA for samples 1-6 from Reject cut-off_D.

Further, the normal and interlaminar shear stresses of samples 1-6 were evaluated from the FE-results at the respective experimental failure loads. Low shear stresses were determined for the samples 1, 2 and 3, with only small amounts of pores and no delaminated areas, at the respective failure loads. As expected, from the FE-results and from short-beam bending of standard material bending failure occurred at the lower side of the samples. In contrast, high shear stresses were evaluated close to the delaminations of samples 4 and 6, where also shear failure was observed during experiment, see Figure 73 a and c. The shear stress concentrations caused local failure at the delaminations, see Figure 73 a and c. The ultimate failure however occurred for all samples due to bending failure at the lower side. The FE simulations of sample 5 showed high tensile stresses close to the delaminations where also tensile cracking occurred during experiment, compare Figure 73 b. All stress distributions shown in Figure 73 were calculated at the respective experimental failure loads.

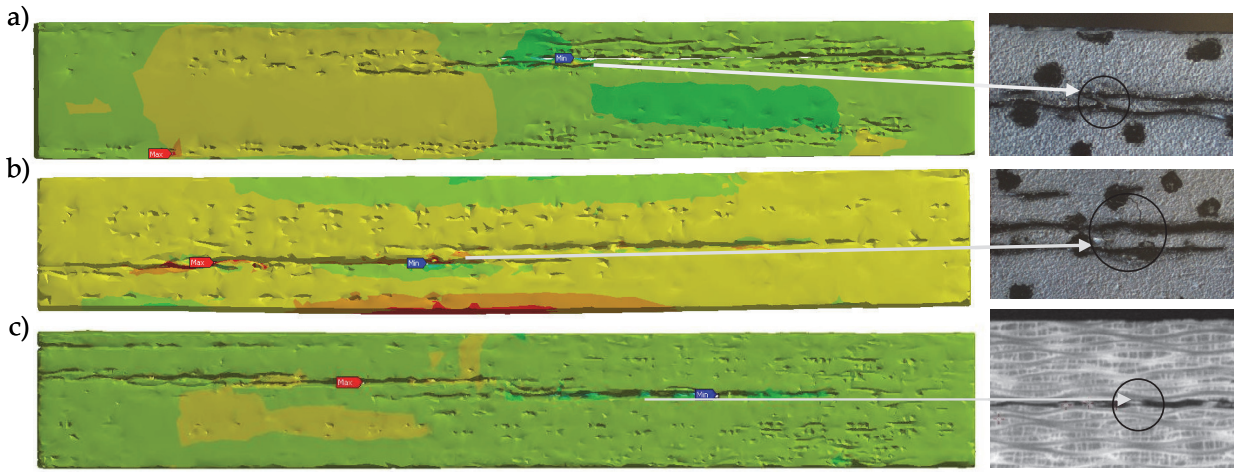

Figure 73: Interlaminar shear stress distribution of sample 4 (a), normal stress distribution of sample 5 (b) and interlaminar shear stresses from FEA for sample 6 (c), min. and max. stress locations are indicated; corresponding failure modes from experiment are shown (black/white dot pattern due to optical strain measurements).

Overall, the real structure modelling showed that the general load-deflection behaviour of delaminated C/C-SiC material can be described by FEA based on 3D-CT data. The critical stress locations could also be predicted by FEA. Nevertheless, the real structure models would have to be extended by the failure models from chapter 6.2. in order to predict failure loads. The investigated reject plate, however, showed extremely strong variations in microstructure, see Figure 67, which were influencing the effective strength even more than the interlaminar defects did. The strong conversion of the C-fibre bundles is indicating additional manufacturing deviations during carbon fibre fabric pre-treatment. In the next chapter, it is going to be shown that the failure loads can be predicted for delaminated samples, by the damage models from chapter 6.2, if the microstructure is consistent.

7.3 Fracture mechanical modelling of desiliconized C/C-SiC with delaminations

This chapter is demonstrating in which way the effect of delaminations on the stiffness and strength of desiliconized C/C-SiC-samples can be modelled by FEM. Samples from plate PH1879_D were taken for the evaluation of the modelling approach.

7.3.1 *Experimental Results*

7.3.1.1 Results from NDT – sample taking

Figure 74 shows the US-result from Plate PH1879_D in desiliconized state and the samples taken for the respective mechanical testing. For short-beam bending, SBB, and ENF-testing samples were selected from regions without interlaminar defects, which are the orange and yellow coloured areas. Those samples were used to determine the standard properties of the plate without manufacturing defects. The quality of samples was checked by visual inspection and by micro-CT after abrasive cutting. The quality of the samples correlated with the results from US-testing. The samples 1, 9, 18, 19, 20, 21 and 22 were intentionally taken from regions with varying amounts of defects. The samples were taken from the border area of the delaminations. Within the delaminated areas, that are the blue and red regions in Figure 74, the samples were completely delaminated and for that reason unfeasible to validate the modelling of crack propagation.

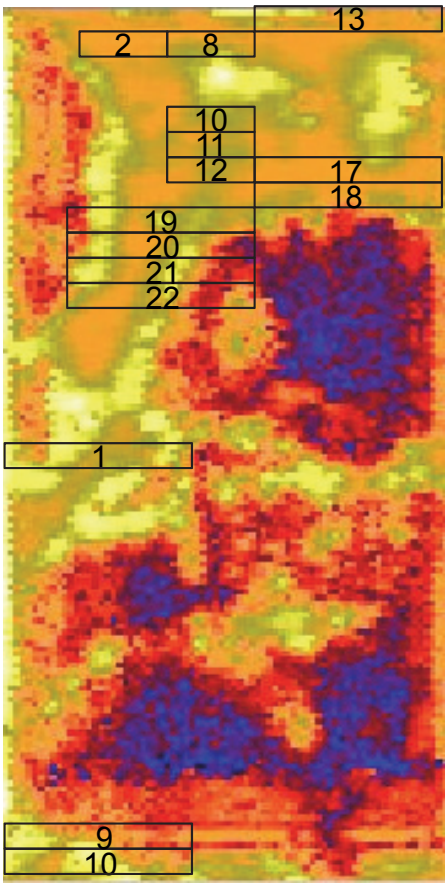

	Sample Number
SBB (L/d = 5)	2, 8, 10, 11, 12
ENF (L/d = 10)	10, 13, 17
Model-Evaluation (L/d = 10)	1, 9, 18, 19, 20, 21, 22

Figure 74: US-result from Plate PH1879_D in desiliconized state and investigated samples with respective mechanical tests.

7.3.1.2 Results from bending test

First of all, short-beam bending tests were performed to characterize the material without manufacturing defects. The short-beam bending test was selected because of the rather small sample size. In that way it was possible to select some standard samples without interlaminar defects within plate PH1879_D. Only three samples (10, 13, 17) could be prepared without interlaminar defects for L/d = 10. Those were used for ENF-testing as presented in chapter 6.1.4.2. All other cut samples for the L/d-ratio of 10 showed delaminations. The average short-beam bending strength was determined to be 163.7 +/- 12.6 MPa. In comparison to the siliconized state with an average of 186 MPa in the same direction, compare chapter 7.1.2, this is again a clear loss in strength due to desiliconization. This effect was also shown for the standard plate PH1991_ND, see Figure 15 in chapter 6.1.1.

Finally, the samples with interlaminar defects were tested in 3-point bending with an L/d-ratio of 10. Figure 75 a shows the samples 18-22 before and after failure. The sample surfaces were painted white before testing in order to facilitate crack observation. All samples failed due to tensile cracking, starting on the lower side of the samples or at the delamination fronts. Figure 75 b shows a sample of plate PH1991_ND without interlaminar defects after first bending failure for comparison.

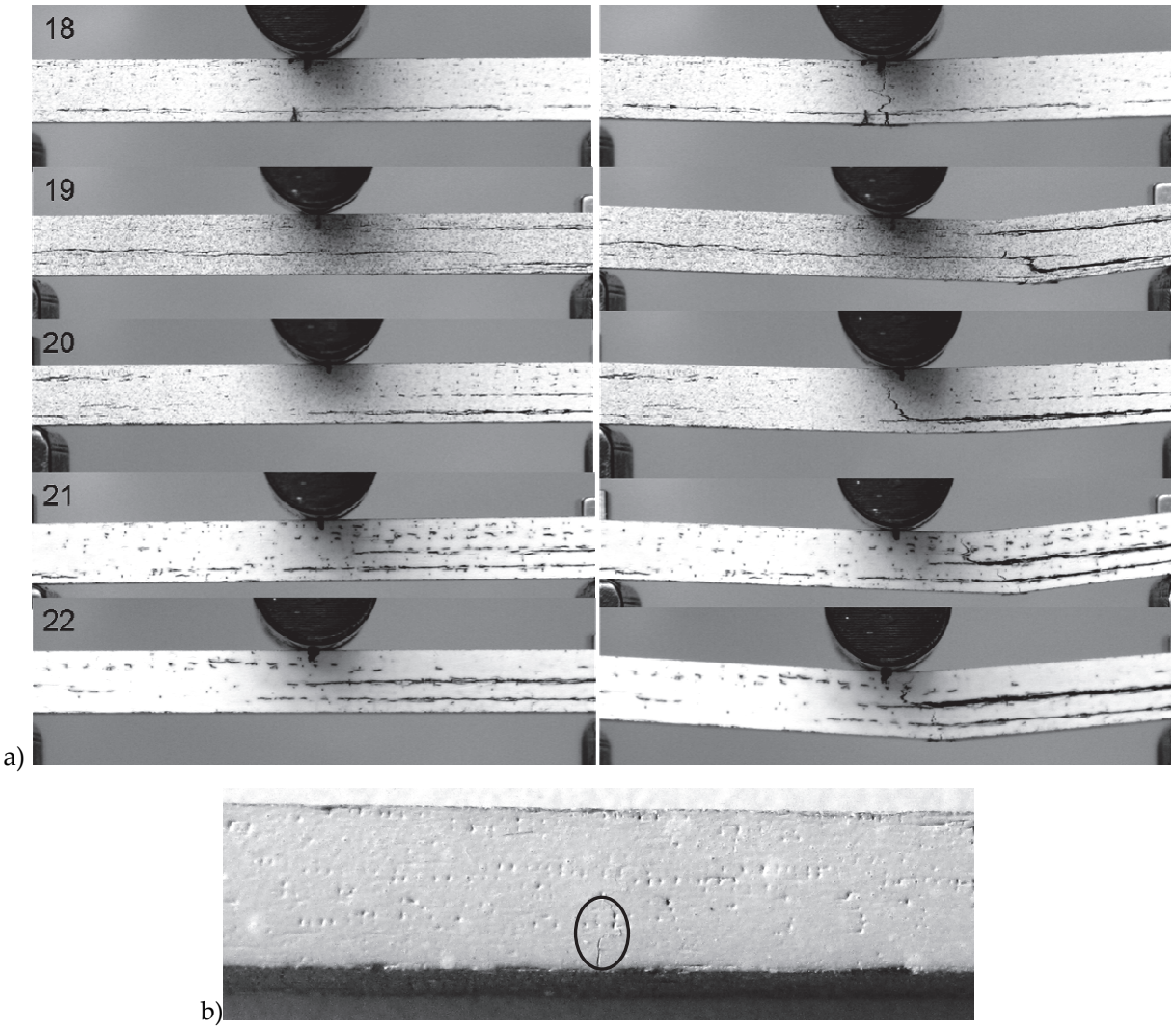

Figure 75: Samples 18-22 from PH1879_D before and after failure (a), sample from PH1991_ND without interlaminar defects after failure (b).

Figure 76 shows the load-displacement curves for the samples 18-22 as well as one representative curve from plate PH1991_ND. The curve from plate PH1991_ND shows slightly higher stiffness and failure load compared to sample 18 with minor delaminations from plate PH1879_D. It was already demonstrated for the siliconized state that plate PH1879 shows reduced strength and stiffness in comparison with plate PH1991_ND, see chapter 7.1.2. Therefore it cannot be stated that the slight decrease in strength and stiffness of sample 18 in comparison with plate PH1991_ND is caused by the delamination shown in image 1, Figure 75 a.

The strength of sample 18 is even on the same level as the average strength of short-beam bending samples without delaminations from plate PH1879_D. Figure 14 in chapter 6.1.1 demonstrated that the short-beam bending strength is similar to the bending strength of L/d = 10 for plate PH1991_ND. That means, although sample 18 showed some local delaminations, the bending strength was not affected.

In contrast to standard bending failure the load-displacement curve of sample 18 in Figure 76 shows a second maximum after ultimate load which indicates crack deflection. The crack deflection was caused by the delamination shown in image 1, Figure 75 a. In that case the delamination did not reduce the strength of the sample but did even improve the overall fracture toughness. The other samples in Figure 75 and Figure 76, however, demonstrate the decrease of strength and stiffness due to the extent of delamination clearly.

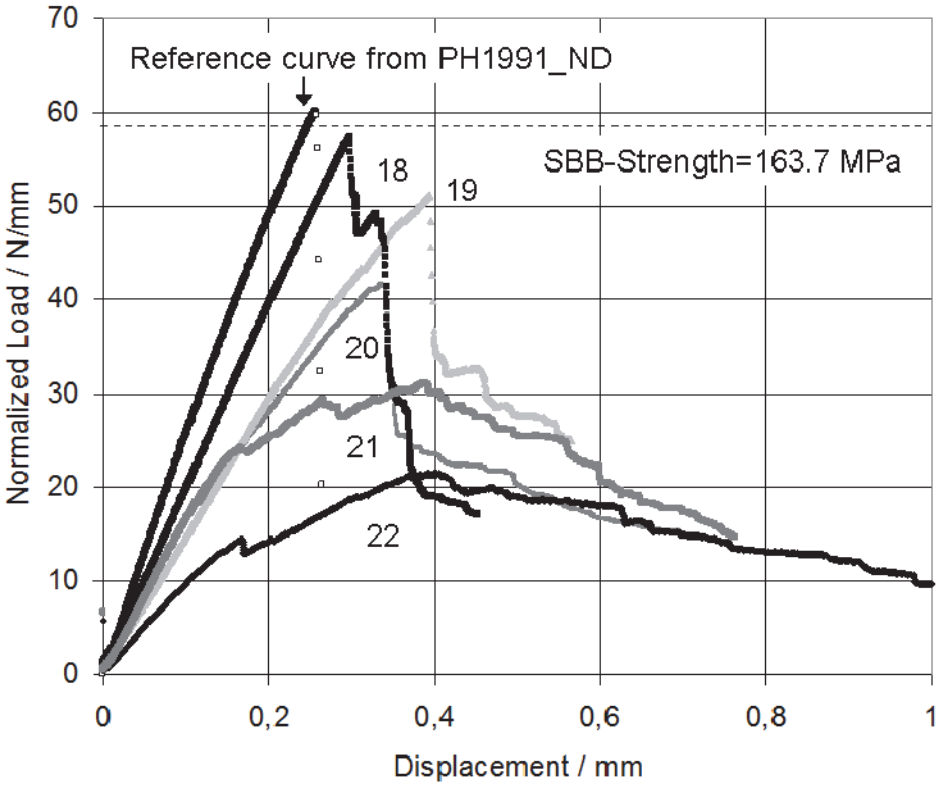

Figure 76: Normalized load-displacement curves from samples 18-22 of plate PH1879_D in desiliconized state and for comparison average short-beam bending strength from PH1879_D and a load-deflection curve from PH1991_ND without delaminations.

Since all samples 18-22 showed bending failure, two more samples, 1 and 9 from plate PH1879_D, were selected containing delaminations concentrated around the midplane. For those samples interlaminar shear failure was expected. In that way the bending as well as shear failure models should be evaluated.

Figure 77 confirms the expected failure modes of sample 1 and 9. Both samples showed first shear failure followed by final bending failure. The small circles in Figure 77 indicate the shear failure locations; the larger ones show the bending cracks.

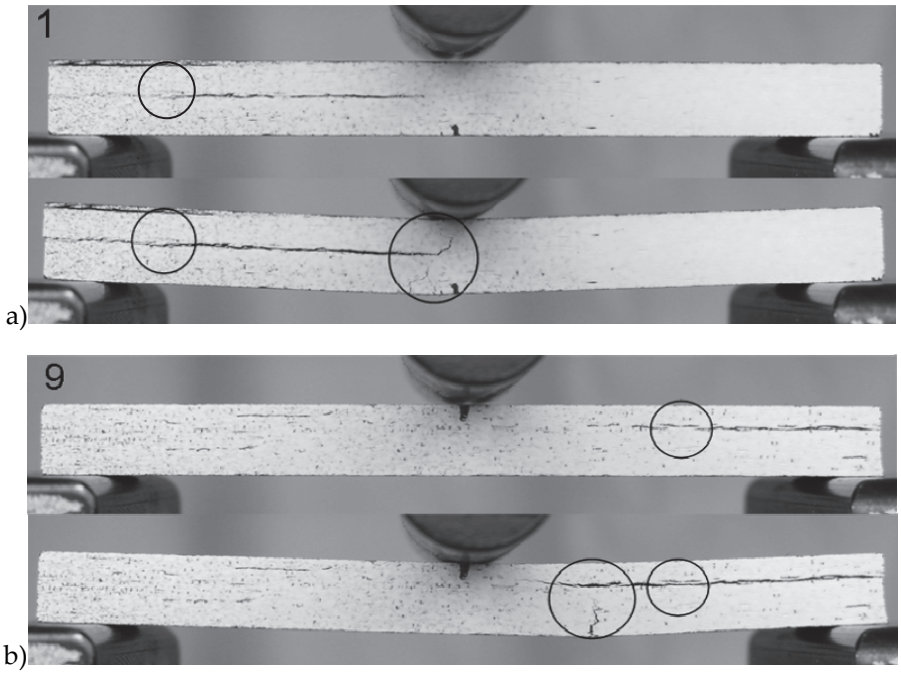

Figure 77: Samples 1 (a) and 9 (b) from desiliconized plate PH1879_D before and after failure; circles indicate failure locations.

Sample 1 shows the first (width-normalized) load maximum at about 28 N/mm in Figure 78. Shear failure occurred at this load point. The shear failure was connecting the two delaminations in adjacent layers, see smaller circle in Figure 77 a. At the second load maximum bending failure occured simultaneously at the lower side and from the delamination front growing upwards. At the lower side even two cracks are observed; the left one starts first and is unified then with the middle crack.

Sample 9 shows a first kink in the normalized load-deflection curve at 38 N/mm, see Figure 78. Roughly at this load point crack propagation was observed at the interrupted delaminated area, see little circle in Figure 77 b. Due to the crack propagation one delaminated area was formed. At the maximum normalized load of 48 N/mm, shear crack propagation at the delamination front and tensile failure at the lower side of the sample were observed simultaneously.

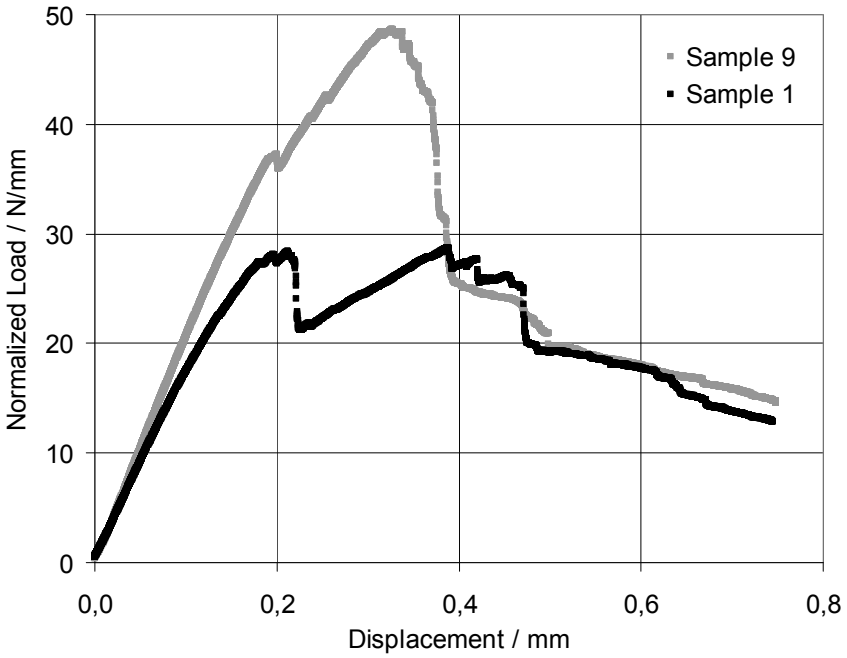

Figure 78: Normalized load-displacement curves for samples 1 and 9 from plate PH1879_D in desiliconized state.

7.3.2 *Simplified 2D-FE-models based on 3D-CT data*

Starting from 3D micro-CT data, with a voxel size of 36 µm, 2D-FE-models of bending samples with interlaminar defects were generated. First the delaminated volume had to be segmented following grey scale with the help of profile lines, see Figure 79 a, using the software Mimics [54]. The main problem with segmenting air from C/C-SiC is contrast. The x-ray absorptions of carbon and air are far below SiC. That is why carbon and air are quite similar in grey scale for C/C-SiC-data sets. That makes it difficult to find the right grey scale limit for segmentation. In Figure 79 a, the limit which was chosen for air is a grey scale of 1276. The profile lines show that this grey scale limit is reasonable because it includes the porous regions on the right side but also excludes the intact microstructure on the left side. The green colour is indicating air, i.e. delaminated areas. Figure 79 a shows that the delamination cannot be segmented as one joint area. The resolution and contrast is too low to segment narrow or touching delaminated areas. After segmentation, the delamination length was measured. Figure 79 b shows the top-view of one delaminated region in sample 20. Three measurements of the green, i.e. delaminated, area were performed for each delamination front. An average initial delamination length of 27.16 mm was determined for the presented area. Pores and small delaminations which did not show extensions over more than half of the sample width were neglected, e.g. lower left of Figure 79 a.

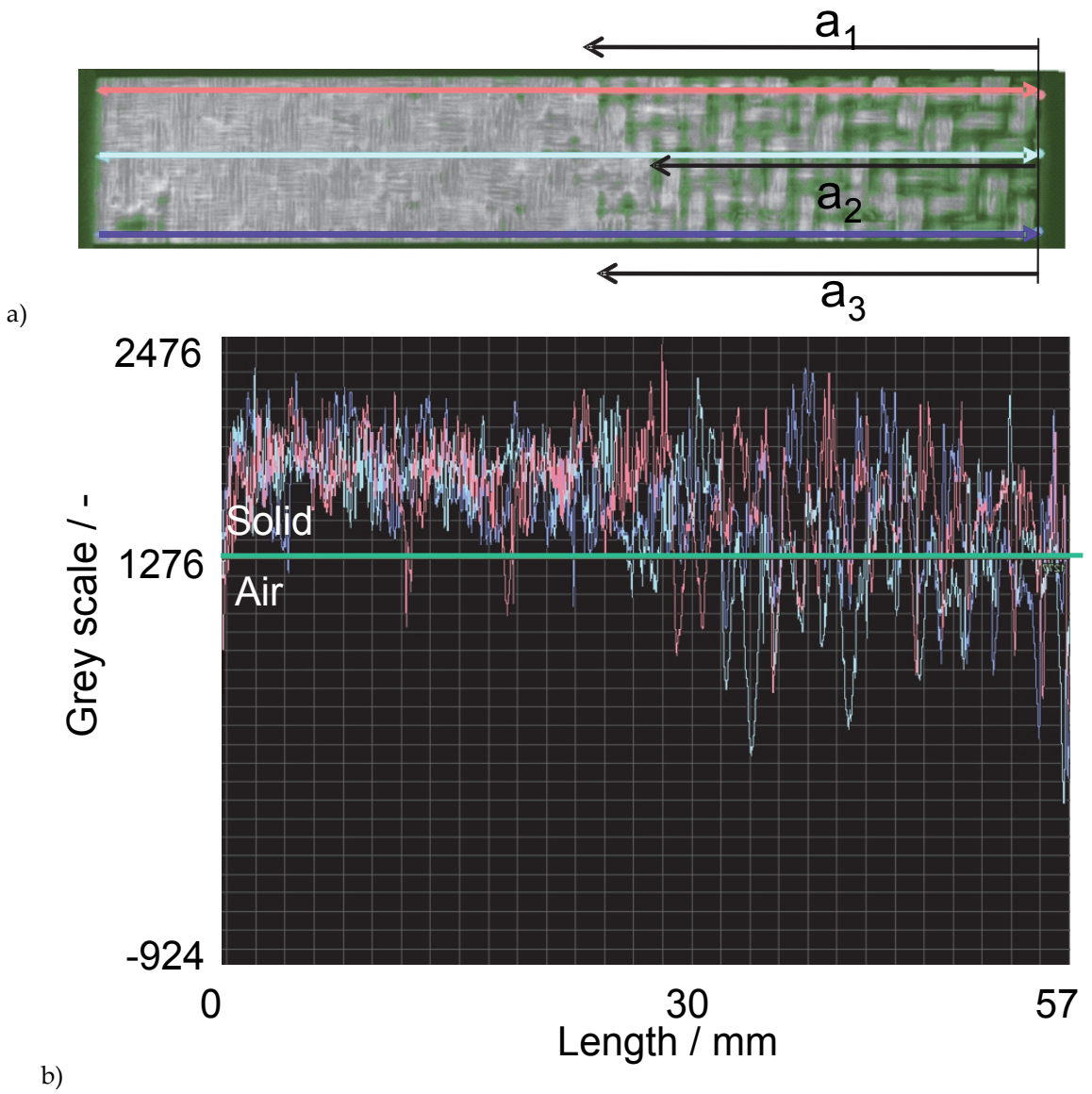

Figure 79: Top-view on delaminated layer of sample 20 with profile lines and measurements of average delamination length (a); the green areas are indicating air. The grey scale values from the 3 profile lines and the threshold value for segmentation, 1276, are shown in (b).

Finally, the through-thickness position of each delaminated layer was measured. The average length and position of delaminations were used for the design of the 2D-FE-models shown in Figure 83 a. The elastic material data and cohesive zone parameters were adopted from the ENF simulations of plate PH1879_D in chapter 6.3.5. The coefficient of friction was set to 0.7. In contrast to the ENF tests with aluminum inserts the C/C-SiC is directly in contact for the investigated delaminations in plate PH1879_D. Therefore the coefficient of friction was increased.

7.3.3 *FE- and experimental results*

First, it had to be proofed that the bending failure model, introduced in chapters 6.2.1 and 6.2.2.2, is also predicting the short-beam bending behaviour of samples without defects from plate PH1879_D. The standard short-beam bending strength from plate PH1879_D was determined with 163.7 +/- 12.6 MPa. A linear elastic and partial bilinear FEA of the short-beam bending test was performed. The maximum stress value for the bilinear analysis was set to 92 MPa, the tensile strength of desiliconized C/C-SiC. For the linear elastic analysis the maximum stress value was increased to 105 MPa to compensate for non-linear effects, as described in chapters 6.2.2.2. and 6.3.3, Figure 48. Figure 80 demonstrates that the bilinear and linear elastic analysis give similar results. The theoretical short-beam bending strength from FEA is 165 and 162 MPa respectively.

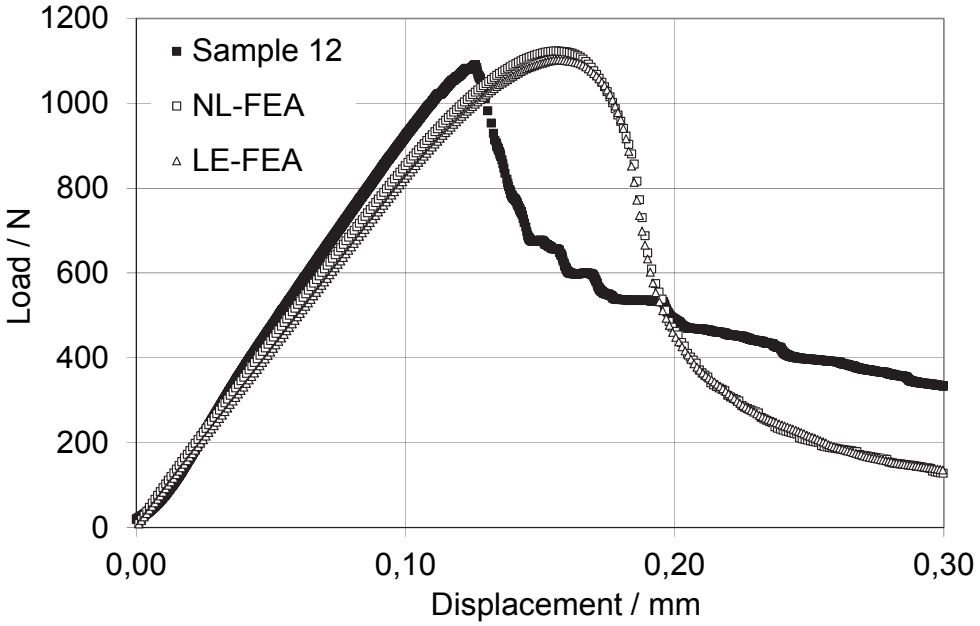

Figure 80: Load-displacement curve of short-beam bending test (L/d = 5) for sample 12 of plate PH1879_D with results from linear elastic and partial bilinear FEA.

The generation of 2D-FE-models from 3D CT-data, described in chapter 7.3.2, is based on the assumption that a diagonal delamination front may be imaged by the equivalent average delamination length in a 2D-model. A numerical study was performed to proof that: three different delamination lengths were simulated in 2D: 14, 18 and 22 mm. Figure 82 shows that the stiffness, first failure load and load drop decrease with initial delamination length, as expected from chapter 6.3.5. No more load drop is observed for a = 22 mm because only a slight crack propagation of 3 mm to the central load line is possible. Additionally, a 3D-model with a diagonal delamination front of 45°-orientation, see Figure 81, was simulated. The delamination front starts from an initial crack length of 14 mm and ends at a maximum length of 22

mm. The crack front was designed with perpendicular lines at the ends to avoid convergence problems. The FE-results in Figure 82 show that the stiffness and critical load for crack initiation of the 3D-model correspond to the 2D-model with the average crack length of 18 mm. It is assumed that the indicated correlation may be transferred, in some extent, to higher angles than 45°.

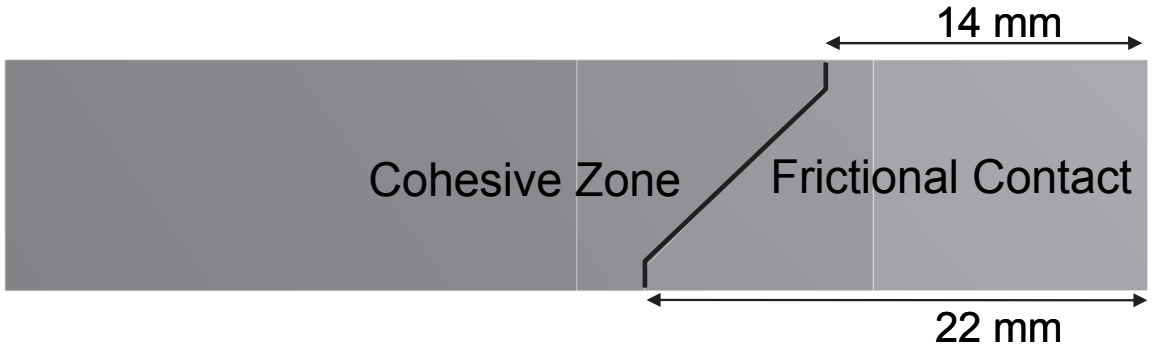

Figure 81: Top-view on a fictitious diagonal delamination front of a 3D-FE-model.

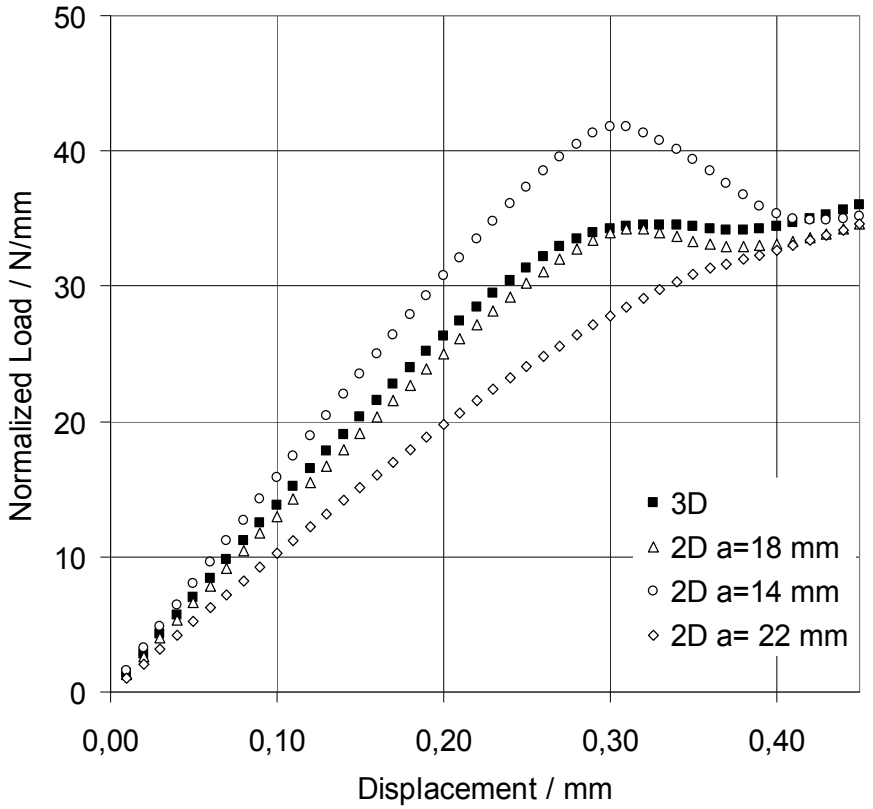

Figure 82: Comparison of 2D-FE-results with results from a 3D-FEA of a bending sample with diagonal delamination front (a = 14-22 mm), see Figure 81.

Consequently, the FEAs of samples 18-22 were carried out in 2D with average delamination lengths. The cohesive zone regions in Figure 83 a were defined as deduced from 3D-CT-data, see chapter 7.3.2. Frictional contact zones and horizontal

cohesive zones were introduced in the layers where delaminations were found. Vertical cohesive zones for bending failure were introduced at the delamination fronts and in the middle of the samples. Those are the regions of highest bending stresses, as demonstrated in chapter 6.3.5. In order to get an efficient design of the cohesive zone models, sample 21 was adapted from sample 20. That is why sample 21 shows some additional cohesive zones which were adopted from sample 20, see Figure 83 a.

Figure 83 b shows the qualitative longitudinal stress distributions for samples 18-22 after failure. The circles indicate failure zones. The failure locations are in good agreement with the failure zones from experiment, see Figure 75. All samples, in FEA as well as in experiment, failed due to tensile cracking.

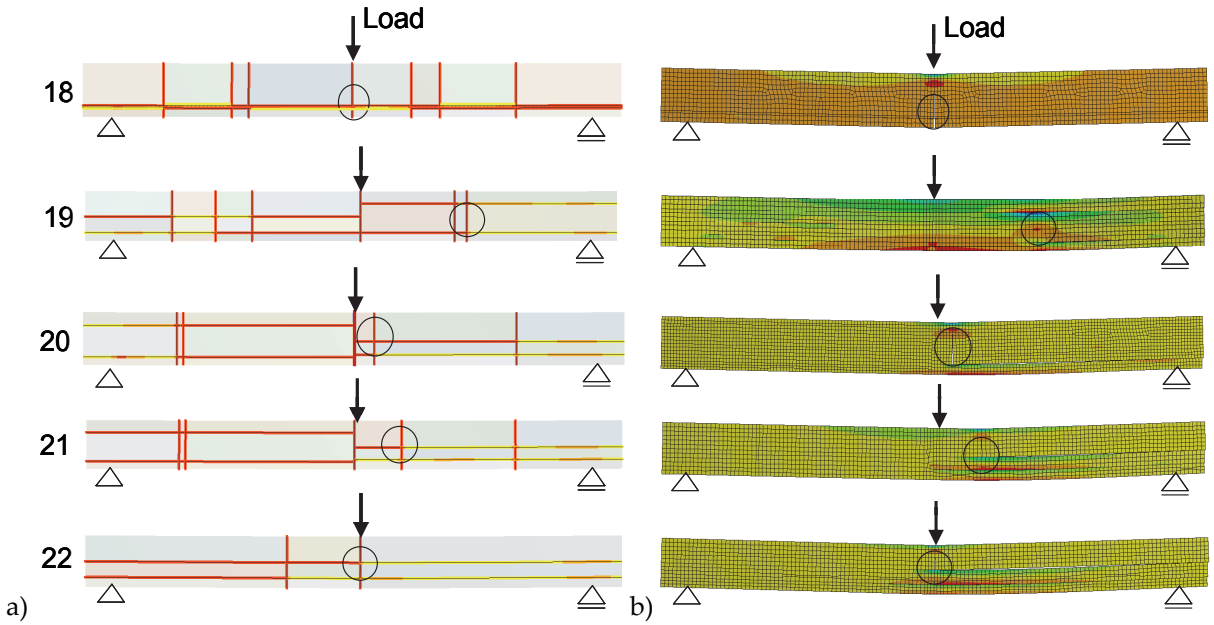

Figure 83: 2D-cohesive zone models for samples 18-22 before failure: yellow lines are frictional contacts, red lines are still bonded contacts (a) and longitudinal stress distribution after failure (b); failure locations are indicated by circles.

Figure 84 is showing the load-displacement behaviour from FEA and experiment for samples 18-22. The numerical and experimental results are in good agreement.

As mentioned in the experimental results of chapter 7.3.1, sample 18 showed crack deflection due to a central delamination on the lower side of the sample. The numerical load-deflection curve shows the same effect: there is an additional kinking of the load-deflection curve beyond the maximum load point which indicates that the delamination is hindering translaminar crack propagation.

The stiffness of sample 18 is comparable to the FE-result for a standard bending sample without defects. The bending strength from the FEA of sample 18 is even slightly higher than the strength of the standard bending beam. The FEA shows that

the delamination does even increase the effective bending strength in the case of sample 18.

The maximum load points for all samples are closely predicted by FEA. The experimental and numerical stiffness is according for the samples 18, 19 and 20.

However, the stiffness is underestimated by FEA for samples 21 and 22. The first failure of samples 21 and 22 is not indicated by the FE-models which can be explained by looking at the images of sample 21 and 22 in Figure 75 a. Sample 21, in particular, is showing interruptions of the delaminated areas. Those were not included in the FE-models because micro-CT analysis showed only very local bridging of the delamination close to the sample surface, as imaged in Figure 75 a.

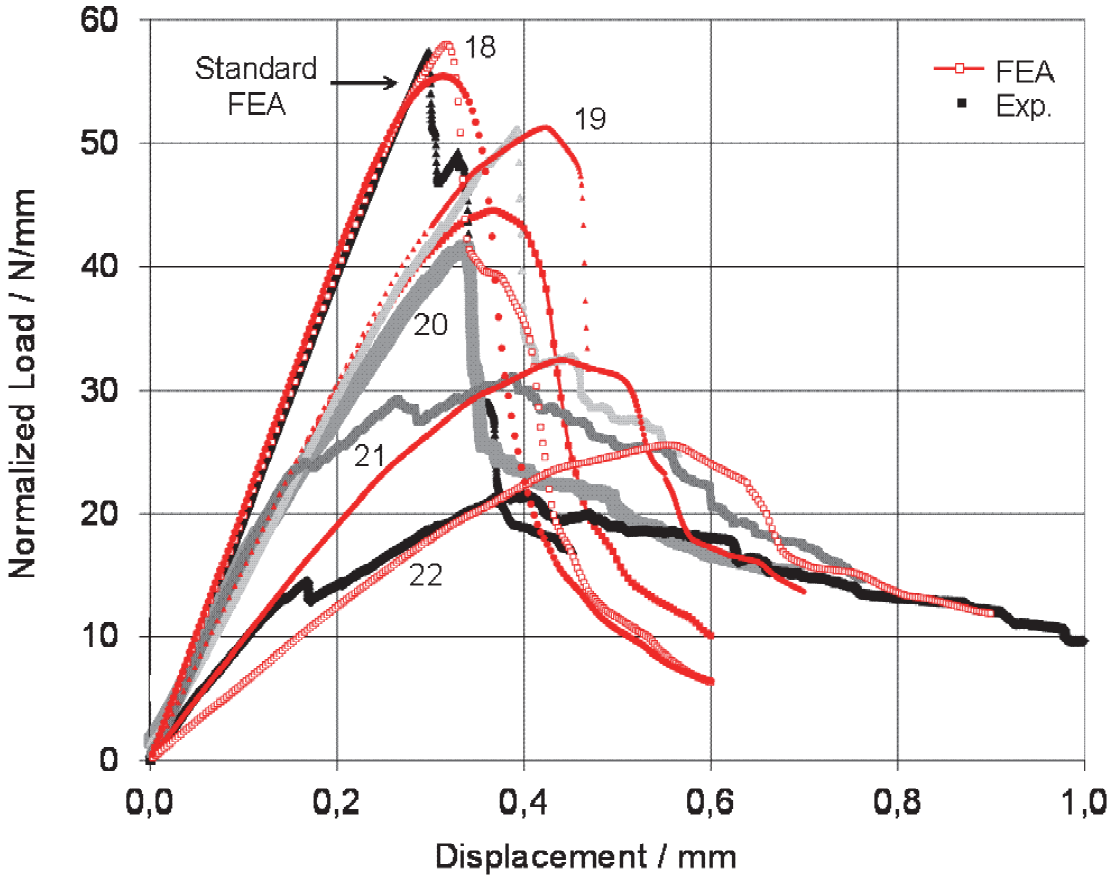

Figure 84: Width-normalized load-displacement curves from experiment and FEA for samples 18-22 from plate PH1879_D in desiliconized state; the FE-result from a bending sample without defects is also shown.

The effect of interrupted delaminations was investigated in more detail for samples 1 and 9 because the local bonding of delaminated faces also had strong influence on the predicted maximum load. The parameter i was introduced in the FE-models to describe the distance between the delaminated areas, i.e. the length of the interruptions, compare Figure 85 a.

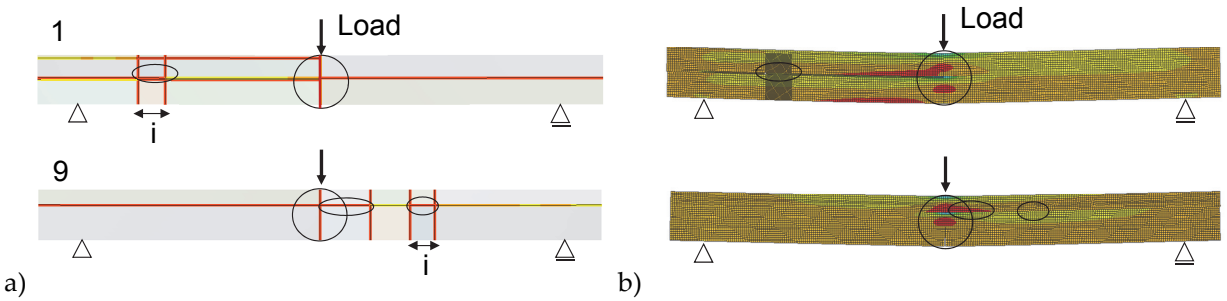

Figure 85: Cohesive zone model for Sample 1 and 9 before failure (a), normal stress distribution after failure (b). i is the distance between delaminated areas. The black circles are indicating failure of Cohesive Zone Elements.

Figure 86 shows slices from micro-CT-data of sample 1 in two different, adjacent layers. The distance in z-direction is about 0.17 mm. The average i in xy-plane was measured to be 2.8 mm by evaluating the micro-CT data.

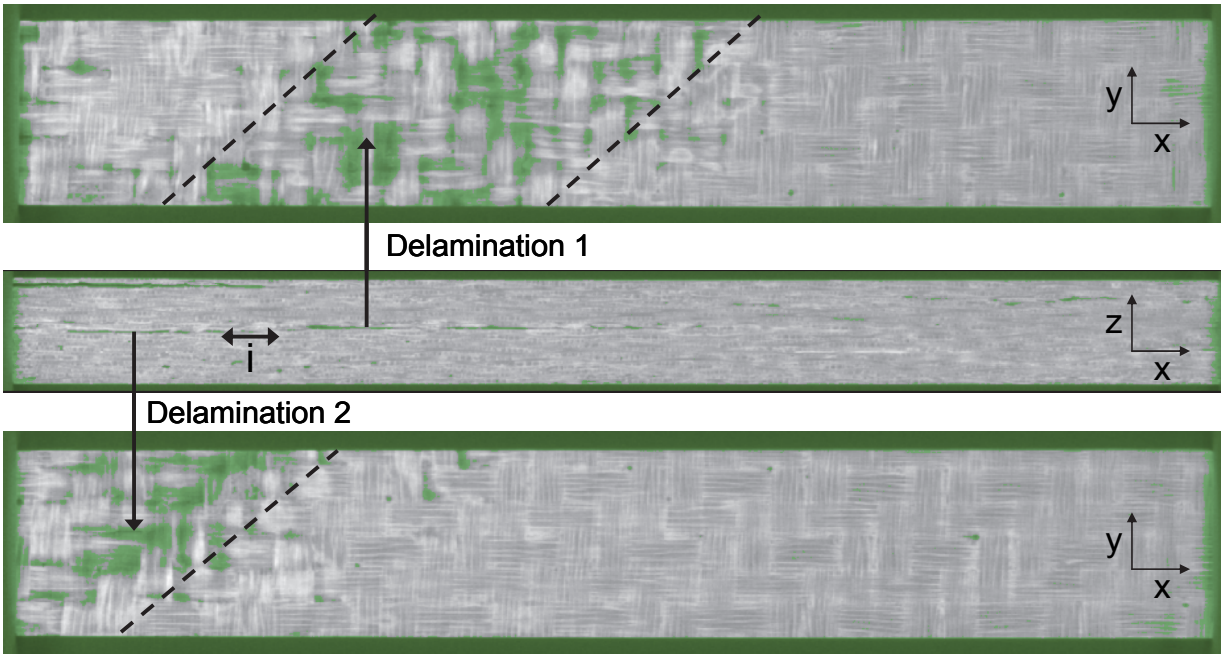

Figure 86: Cross-sections from micro-CT for sample 1 of plate PH1879_D. The green colour is indicating air, i.e. delaminated areas.

The FEA with i = 2.8 mm overestimates the first failure load, see Figure 88 a. That is why the parameter i was varied from i = 2.8, i = 1.5 to i = 0 mm in Figure 88 a. The FE-results from i = 1.5 mm fits well to the experimental result. The model with 0 mm of delamination distance, that is only a vertical separation, underestimates the first failure load. For all cases, the subsequent bending failure from FEA is similar to the second experimental load maximum. The failure modes and locations indicated in Figure 85 correspond to the cracks from bending experiment shown in Figure 77 a. Figure 88 a shows quite well in which way bridging of delaminated areas can

influence the first failure load. By variation of further parameters it was confirmed that the parameter i has the main effect on the first load maximum. The G_{IIC} value was varied between 0.31 and 0.35 N/mm. In addition the two delaminations were modelled without vertical separation. But those variations, in contrast to the parameter i, did not have a distinct effect on the load-displacement behaviour. Finally the same approach was used to model sample 9. The CT-cross section in Figure 87 shows a bonded area with width i in between of delaminated areas, also indicated by the side view in Figure 77 b.

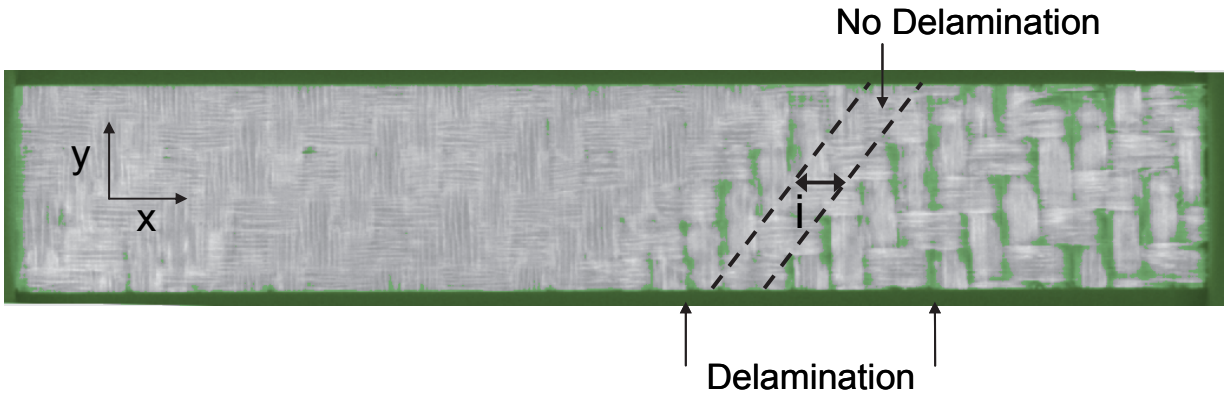

Figure 87: Cross-section from micro-CT data through delaminated layer of sample 9 from plate PH1879_D. The green colour is indicating air.

The sample 9 was modelled once with i = 2.5 mm, as measured from CT-data, and once without interrruption, i.e. i=0. The FE-result corresponds to the experimental stiffness and shear failure load if the interruption of delamination, i = 2.5 mm, is taken into account, see Figure 88 b. The bending failure load, however, is underestimated by FEA.

Overall, the experimental behaviour is well reproduced by FEA. Nevertheless, looking at the failure locations and crack propagation of sample 9, the same differences between FEA and experiment are found as described for ENF-testing in chapter 6.3.5. First, the interlaminar crack does not reach the middle of the sample in experiment. Instead the crack starts growing upwards before, compare Figure 77 b.

By contrast, the FEA predicts interlaminar failure up to the central load introduction followed by tensile failure at the crack front and at the centre of the lower beam side, see Figure 85 b. In experiment, the bending failure occurred roughly at the initial delamination front on the lower side of the sample, see Figure 77 b.

This circumstance shows that the reason for deviating bending failure locations from ENF-testing and ENF-FEA is not the abrasively cut crack, as discussed in chapter 6.3.5, but the increase of G_{IIc} with crack length preventing further crack propagation below the central load point. Thus the bending stress close to the initial crack front is increased. The width of delamination in plate PH1879_D was typically about 80 µm.

Bending moments due to the compression of delaminated areas may be considered as negligible.

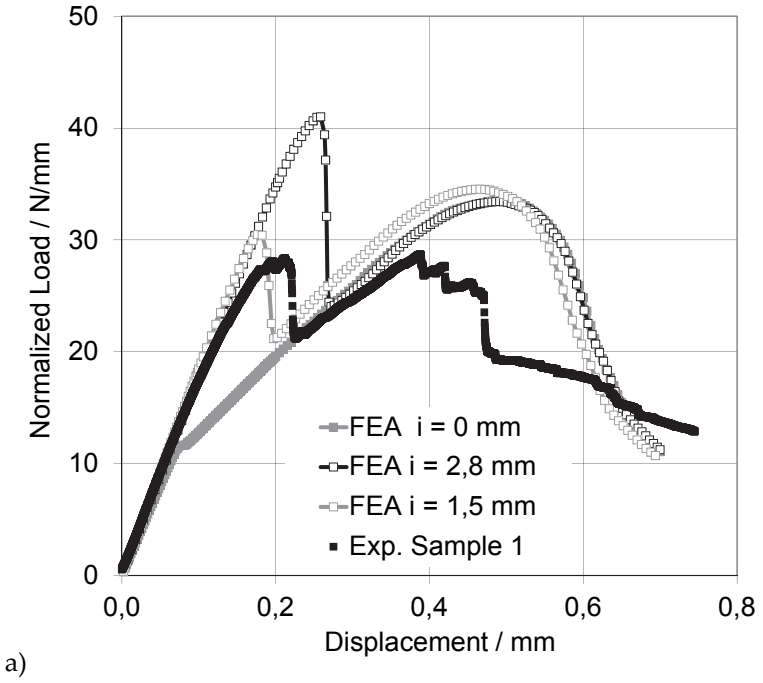

a)

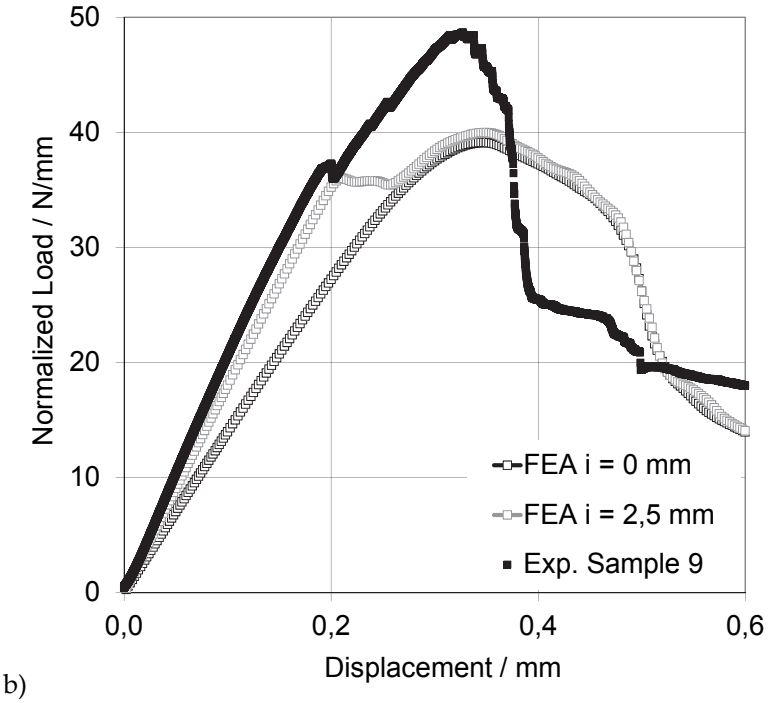

b)

Figure 88: Normalized load-deflection curves from experiment and FEA in dependency of parameter i for samples 1 (a) and 9 (b) from plate PH1879_D.

Figure 89 compares the stiffness and maximum load points from experiment and FEA for the seven investigated samples of plate PH1879_D. The stiffness is quite well reproduced by FE-modelling, except for sample 21 with local delamination bridges, as

mentioned above, where the FEA is underestimating the stiffness. The maximum load values from FEA are in good agreement with the experimental values for the samples 18-22. The samples 1 and 9 show some discrepancies. The results plotted here refer to the parameters i = 2.8 mm for sample 1 and i = 2.5 mm for sample 9. The parameter i, representing the interruption length of delaminated faces, was determined in those cases directly from micro-CT-data. Considering the varying extents of delamination in the investigated plate and samples, the presented approach proofed high flexibility and reliability to predict the mechanical behaviour of C/C-SiC with interlaminar defects.

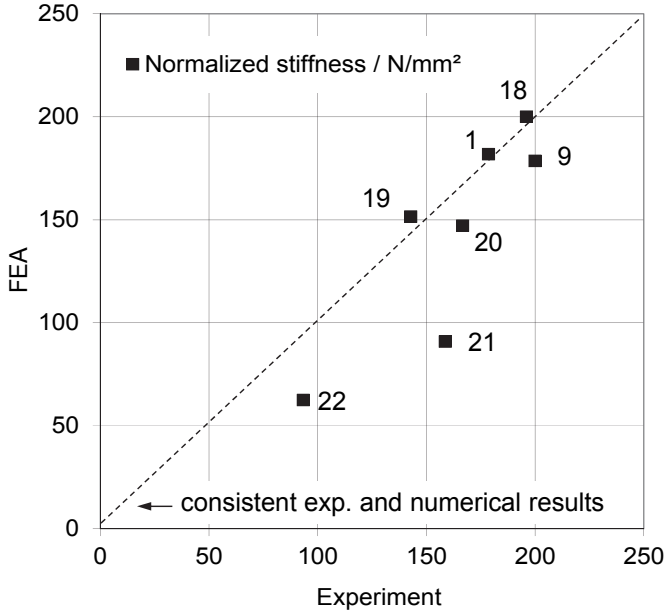

a)

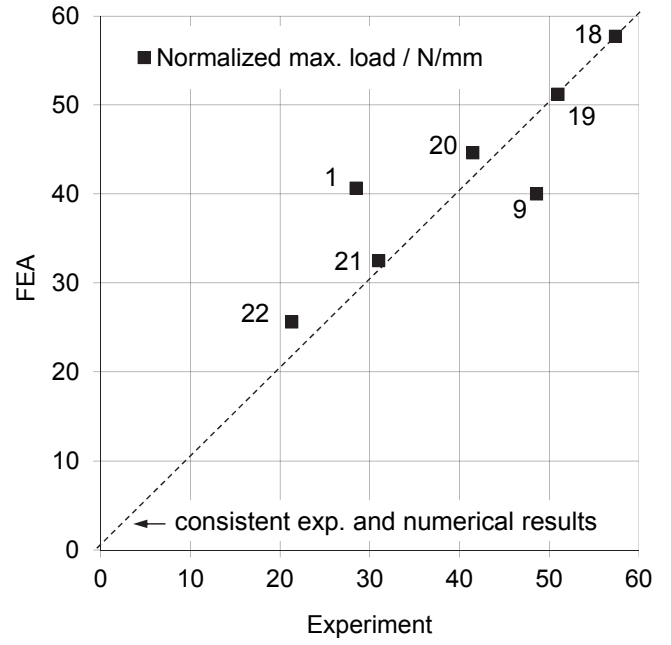

b)

Figure 89: Comparison of experimental and numerical stiffness (a) and maximum loads (b); the sample numbers are indicated.

8. Discussion

8.1 Interlaminar manufacturing defects in C/C-SiC material

It was demonstrated that the pyrolysis is the critical processing step leading to delaminations in chapter 5.2. Additionally it was shown that the CFRP quality has a crucial influence on the subsequent C/C state. Further, it was demonstrated that standard and delaminated plates may be readily distinguished by ultrasonic testing in C/C state. However, it is not yet clear which raw material waste criteria or autocalve parameters have to be chosen to definitely prevent the formation of delaminations in the subsequent pyrolysis step.

Since the delaminations were filled with free silicon during siliconization, the impact of free silicon on the mechanical behaviour was investigated in siliconized state. The desiliconized state was then used to investigate the impact of delaminations on the mechanical behaviour. The free silicon was shown to have no impact on the interlaminar properties and only a slight impact on the in-plane bending properties at room temperature. The behaviour at elevated temperatures has to be investigated separately.

In general a computational model is needed, describing the relations between raw materials (fibres and polymer matrix) and their behaviour during the three LSI processing steps. In that way a deeper understanding of fibre-matrix interactions during processing could be gained and critical raw materials and processing parameters for specific component designs may be defined in order to prevent delamination.

8.2 Modelling of tensile and bending behaviour

It was shown that the tensile failure of C/C-SiC in varying orientations can be described by the Hill and Tsai-Wu failure criterions in chapter 6.2.1. Both criterions were fitted for the C/C-SiC-properties of standard siliconized material. Since the Hill and Tsai-Wu criterions are both quadratic failure criterions and the Hill criterion can be considered as a special case of Tsai-Wu criterion it is not surprising that both criterions agree well with each other. In the same way Fink [14] used the Tsai-Wu criterion to describe the failure of C/C-SiC in his work. The Tsai-Wu criterion has the

advantage, in contrast to the standard Hill criterion, that differing strength under tensile and compression load can be included. That is why the Tsai-Wu criterion is highly recommended for the design of structural parts made of C/C-SiC. Nevertheless, additional experimental data from combined load cases under tensile, compression and shear loads is needed to improve and validate the Tsai-Wu parameters determined in chapter 6.2.1, Table 5.

The non-linear behaviour of C/C-SiC under tensile load was modelled by the generalized Hill yield criterion from Shih and Lee [46] with the bilinear hardening rule by Valliappan et al. [47][43]. In spite of the simple bilinear hardening approach, implemented in ANSYS, good agreements of experimental and numerical results were achieved under tensile load.

The differences in stress-strain behaviour under tensile and compression load were considered for modelling the bending behaviour by dividing the bending beam into two half bodies. Due to the consistency equation of the used yield and hardening models by Shih and Lee [46] and Valliappan et al. [47][43], it was not possible to describe the highly differing tensile and compression behaviour within one material model. Nevertheless, the characteristic behaviour of C/C-SiC could be modelled by separated linear elastic and bilinear material definitions used for the divided bending beam.

The experimental and numerical results showed that the nearly linear elastic compression behaviour leads to a support of the non-linear tensile side of the bending beam. This effect leads to an upwards shift of the neutral axis and a decrease in stress on the tensile side. In that way, already an increase of the theoretical bending strength relative to the tensile strength can be explained. The decrease of effective tensile stress depends on the differences in tensile and compression stress-strain behaviour. The effective stress at tensile failure stress is reduced by about 50 MPa in 45° orientation and by about 20 MPa in 0/90° direction, as shown in chapters 6.3.2 and 6.3.3.

So far, the explanation for the bending-tensile strength ratio is similar to the work of Hild et al. [19] who considered the non-linear tensile behaviour for different Nicalon-fibre reinforced CMCs.

In order to explain the remaining difference between tensile and bending strength a macroscopical fracture mechanical approach was introduced, in contrast to Hild et al [19] and Marshall and Evans [16] who proposed micromechanical modelling of fibre and interface properties.

Since SENB failure of C/C-SiC occurred by one single planar crack, the WOF and critical energy release rate could be determined successfully. By contrast Marshall and Evans [16] observed shear failure during SENB testing of unidirectional SiC-fibre glass-ceramic composites. Although SENB testing of C/C-SiC was successful for various fibre orientations, a contradiction to Griffith theory [50] was noticed. In contrast to Griffith: $G_c = K_{Ic}^2/E$, constant WOF and K_{Ic} values were measured for C/C-

SiC in 0/90° and +/-45° orientation, although the Young's moduli in 0/90° and +/-45° direction are different. As mentioned in chapter 6.1.3, the +/-45° and 0/90° load-displacement curves showed similar stiffness. It is assumed, that due to the low L/d-ratio of about 5 the higher in-plane shear modulus of the +/-45° orientation induced a significant increase of the measured stiffness and thus influenced the effective K_{Ic} value. Weisenberger [53] proofed this assumption by evaluating SENB tests on desiliconized C/C-SiC with L/d-ratios of 10. The K_{Ic} value for +/-45° was accordingly lower than for 0/90°. The WOF was constant for both orientations. L/d-ratios of 10 are recommended for SENB analysis of further CMCs.

Fink [14] did also suggest a fracture mechanical approach in order to explain the bending strength of C/C-SiC. However, Fink used a smeared fracture mechanical approach with arbitrary energy release rates. The present work is using a cohesive zone approach representing the macroscopic crack path and experimentally confirmed energy release rates.

A close prediction of the bending strength in varying load orientations was reached.

Finally it can be summarized that the bending-tensile strength ratio of C/C-SiC is influenced first by the differing tensile and compression stress-strain behaviour, as already shown in literature for other CMC materials [17]-[20] and finally by the WOF being necessary to create a macroscopic crack leading to failure under bending load.

The meaning of fracture toughness for the mechanical behaviour of CMCs was already outlined by Kuntz [23] and Fink [14]. The present work demonstrated a straight-forward fracture mechanical approach, using the commercial code ANSYS, which allows the fracture toughness to be considered in the computation of CMC components and structures.

In contrast to typical WMCs, like C/C or CFRP, C/C-SiC is showing a rather brittle failure under bending load. The bending failure is not a 'first-ply-failure' as expected for typical WMCs but a brittle failure through roughly one third of the laminate thickness. This observation is important for the characterization of C/C-SiC. As mentioned in chapter 3.2, the stress-strain behaviour of C/C-SiC is rather close to WMC-materials because the 0/90° behaviour is almost linear elastic in contrast to the highly non-linear 45° orientation. In contrast to typical WMCs, however, the tensile strength in 0/90° and 45° orientation is similar for C/C-SiC. Therefore it can be assumed that the tensile strength in all loading directions is mainly limited due to the brittle SiC-matrix, causing a low fibre utilisation level of 0.17 in 0/90° orientation, see Figure 90.

In chapter 3.2.1, it was already explained that due to its microstructure and mechanical behaviour C/C-SiC is neither a typical WMC nor a WIC material. Therefore another classification for brittle-matrix fibre reinforced materials is introduced in Figure 90. It is distinguished between fibre and matrix dominated materials. The bending-tensile strength ratio is plotted over the fibre utilisation level,

i.e. the experimental composite tensile strength divided by the fibre tensile strength times the fibre volume fraction in loading direction. It is assumed here, that the fibre strength is not significantly degrading during processing. The results in Figure 90 refer to 0/90° fabric-reinforced composites loaded in 0/90° direction. Only WHIPOX is produced by cross-over filament winding. Due to its cross-over points it is comparable to fabric materials.

The matrix dominated composites are characterized by:

- Macroscopic failure initiation due to matrix cracking
- The fibres are not effectively protected by coatings or a weak-enough matrix
- The brittle matrix is reducing the fibre utilisation level
- Fibre utilisation level is low under tensile and bending load
- Brittle failure with strong load drop under bending load
- High ratio of bending to tensile strength

The matrix dominated composites are more sensitive to volume loading than to local loading because local failure is hindered due to the macroscopic fracture toughness of the composite. If the fracture toughness is reached brittle failure by a strong load drop is observed, as shown for C/C-SiC under bending load. Under homogenous loading conditions, like in tensile testing, multiple matrix cracks lead to failure at low fibre utilisation levels, since the fibres are not sufficiently protected against the high-energy matrix cracks. A fracture mechanical failure modelling, as presented here, is recommended for C/C-SiC and corresponding matrix dominated composites.

In contrast to the matrix dominated composites, the fibre dominated composites are characterized by:

- Macroscopic failure initiation due to first-ply fibre failure
- Tensile strength in fibre direction is insensitive to matrix failure, due to a sufficiently weak matrix or interface
- High fibre utilisation level, > 0.3, due to an effective interface or weak matrix
- The weak matrix or interface enables non-brittle ply-by-ply failure
- Low bending-tensile strength ratio

The fibre dominated materials are truly taking advantage of the fibre reinforcement due to the sufficiently weak matrix or interface. In correlation to the He and Hutchinson plot [10][11] in Figure 2 it may be stated that the CMC materials, characterized here as matrix dominated, do not fulfill the microstructural

requirements as described by He and Hutchinson [11] needed for non-brittle composite failure.
The CVI materials in Figure 90 show a rather high fibre utilisation level indicating that the fibre coating is protecting the fibres from cracks within the dense and stiff matrix.
The CVI materials were classified by Koch et al. [10] as WIC, showing a strong non-linear behaviour under tensile load, even in 0/90° direction. Camus [57] compared the tensile and compression behaviour of a CVI SiC/SiC material. The compression behaviour was almost linear elastic in contrast to the strong non-linear behaviour as shown in Figure 3. It may be assumed that the ratio of bending to tensile strength of about 1.5, shown for the CVI materials in Figure 90, is mainly caused due to the differing stress-strain behaviour under tensile and compression load and not due to the macroscopic fracture resistance of the composite.
A fracture mechanical approach is not necessary for the fibre dominated composites but the anisotropic non-linear behaviour has to be described by constitutive models.
The material data in Figure 90 was taken from Moeller [58], Clauß [59], Klatt et al. [60] and an internal DLR material data base.

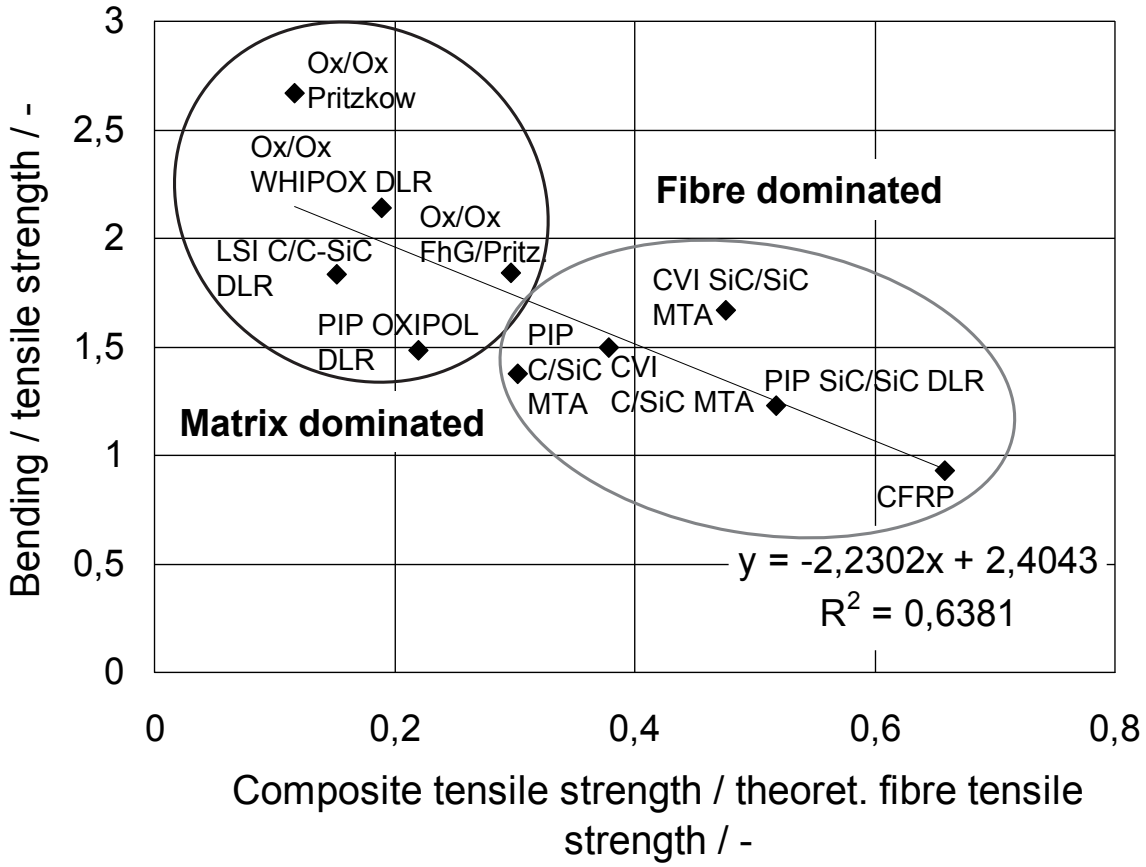

Figure 90: Bending-tensile strength ratio in dependency of fibre utilisation level for various 0/90° reinforced materials.

In the present work, the tensile behaviour of C/C-SiC was described by macroscopic constitutive equations and failure criterions as typically used for fibre dominated materials like CFRPs.

By contrast, the modelling of failure due to local stresses under bending load required fracture mechanical methods for the C/C-SiC material. Therefore cohesive zone modelling was introduced to model the bending failure of the matrix dominated composite.

8.3 Interlaminar fracture mechanics

Although there was some scattering in the experimental results, the critical energy release rates in mode I and II could be determined by adapting the testing standards from ASTM and AITM [33][34][35] for C/C-SiC. The comparison of experimental and FE-results showed that the initiation of crack propagation could be modelled by using the respective average experimental energy release rates in mode I and II.

In contrast to the work by Krombholz and Goldstein [24] the initial crack length could be determined directly due to painting of the sample surfaces. A fitting of FE results was not necessary.

The comparison of experimental load-deflection data with analytical crack propagation curves from Allix et al. [37] and Szekrenyes [36] showed that the interlaminar crack initiation for C/C-SiC under mode I and II load may be described in the same way as it was introduced for CFRPs.

The used cohesive zone approach was based on the linear softening model introduced by Alfano and Crisfield [32] and showed good agreement with the experimental and analytical load points for crack initiation.

The ENF test for the determination of G_{IIc} was performed similar to the work from Kuntz [23]. Therefore, the results of both works can be compared directly. The average G_{IIc} of desiliconized C/C-SiC of 0.32 N/mm is even higher than the G_{IIc} of different fibre reinforced glasses, 0.049-0.229 N/mm, as determined by Kuntz [23]. The determination of propagation crack length during the ENF test was not possible. Therefore, R-curves could not be determined for mode II loading.

The propagation crack length could be estimated for mode I DCB-testing and therefore R-curves were evaluated in that case. Figure 26 in chapter 6.1.4.1 indicates that the G_{Ic} increases linearly with the propagated crack length. It is assumed that the increase of G_{Ic} is caused by microstructural effects like fibre-bridging or increased crack branching.

Because of the increase in G_{Ic} the load-deflection behaviour after crack initiation could not be completely reproduced by the cohesive zone models. However, the load point of crack initiation was well predicted for different initial crack length with an average G_{Ic} of 0.16 N/mm and an experimental interlaminar tensile strength of 5 MPa. A typical

value for mode I fracture toughness of CFRPs, for comparison, is 0.45 N/mm for an unidirectional carbon-epoxy T300 composite as measured by Laksimi et al.[56].

The same propagation effects from mode I investigations were also observed for mode II. The load for crack initiation was again predicted by cohesive zone modelling for various initial crack lengths. The subsequent load drop due to crack propagation was much stronger in FEA compared to the experimental load-deflection curves. Although R-curves could not be determined from ENF-testing it is assumed that G_{IIc} is also increasing with crack propagation due to similar microstructural effects. The load-deflection curves from ENF-testing showed, similar to the DCB-curves, a load plateau after crack initiation.

The increase of G_{Ic} and G_{IIc} with propagation crack length may be included by additional post-processing of the FE-simulations to get more accurate descriptions of the subsequent failure mechanisms. Nevertheless, the first failure load for varying delamination lengths could be predicted by the average G_{Ic} and G_{IIc} initiation values, which were determined experimentally in chapter 6.1.4.

The final bending failure of ENF-samples was modelled by vertical Cohesive Zone Elements accounting for the softening model by Alfano and Crisfield [32] as used for the pure bending samples. A significant difference between the experimental and numerical results was the bending failure location: the ENF-samples showed bending failure roughly at the initial crack length. The FEA predicted failure at the middle of the sample. One main reason was found for this observation: the FE-model predicted interlaminar crack propagation up to the middle of the sample. In experiment, the interlaminar crack stopped some mm in front of the central load introduction, probably because of the increase in G_{IIc}. The early stop of interlaminar crack propagation is leading to an increase of bending stress at the lower side of the sample close to the initial crack front. In the future work, interlaminar crack propagation and subsequent bending failure might be modelled more accurately if the increase of G_{IIc} with propagation crack length is included.

Further, the interlaminar failure models have to be extended for combined mode I+II loadings. In that way the modelling of C/C-SiC structures with interlaminar defects under complex loading conditions will be enabled.

8.4 Modelling of C/C-SiC with delaminations

Two approaches were presented to model the mechanical behaviour of C/C-SiC with delaminations. The first approach is directly based on 3D-micro-CT results. The generation of 3D-FE-meshes is starting directly from grey scale data, see chapter 7.2.2.

The second approach is using abstracted geometrical information from CT-data for the design of equivalent 2D-models, see chapter 7.3.2. The advantage of approach one is rather clear: due to the direct link of CT-data and FE-meshing, it was possible to image geometrical details of defects with high accuracy. In that way critical stress concentrations could be detected similar to the work from Abdul-Aziz et al. for CVI SiC/SiC [29][31]. The detailed prediction of failure load and crack propagation was not possible.

In contrast, approach two had the decisive advantage that due to the simplified geometries complex material models, like the cohesive zone approach, could be computed within acceptable time and effort.

The results of approach two showed that both the exact mapping of defect geometries and the adequate material models are necessary to predict the mechanical behaviour of C/C-SiC with manufacturing defects by FEM.

It was demonstrated that the fracture mechanical models, which were validated on artificial pre-cracks, could be successfully transferred on true manufacturing defects.

Approach two predicted the stiffness, failure loads and crack propagation of 3-point bending samples with varying extents of manufacturing defects with good accuracy. The maximum load of C/C-SiC with delaminations was predicted within an average relative accuracy, $(F_{FEA}-F_{exp})/F_{FEA}$, of 5 %. The average relative accuracy of computed stiffness was 12.6 %. Anyhow, there were individual samples of plate PH1879_D (samples 1 and 21) where the FE-results deviated for over 30 %. The strong deviations of numerical and experimental results were mainly caused by local SiC-bridges which were interrupting delaminated areas. Those local SiC-regions have to be resolved even better in micro-CT and FE-modelling to get more reliable computations. The SiC-regions showed a strong impact on the initial stiffness and first failure load.

On the other hand, a ‘worst case’-approach for structural assessment could be to neglect the SiC-bridges completely and to model the delaminations as uninterrupted areas. Still, the size and location of the delamination itself have to be resolved in detail.

Thus, attention has still to be paid on the resolution and contrast of micro-CT-analyses. If the exact geometry and location of defects in C/C-SiC-components is resolved by NDT, it will be possible to compute the mechanical behaviour of C/C-SiC structures by the same approach, as presented here for bending samples.

9. Summary and conclusions

The present work has demonstrated that the mechanical behaviour of C/C-SiC with interlaminar defects may be described with the help of macroscopic constitutive equations.

First, the bending-tensile strength ratio of standard C/C-SiC without manufacturing defects was explained by considering the non-linear tensile behaviour, the tensile strength in the respective directions and the Work of Fracture within the FE-models. The crack initiation and propagation due to tensile failure was modelled by introducing Cohesive Zone Elements, which were taking the Work of Fracture of C/C-SiC, determined in Single Edge Notched Bending test, into account. The SENB tests did also show that the in-plane fracture toughness of C/C-SiC is independent of the crack orientation relative to the fibre reinforcement. This result reduced the necessary amount of parameters for the in-plane fracture mechanical analysis of C/C-SiC significantly.

Further, the interlaminar failure of C/C-SiC with artificial pre-cracks was described by a fracture mechanical approach, too. The FEA, using CZEs, described the stiffness and crack initiation under mode I and II loading in accordance to the experimental results for varying initial interlaminar crack lengths.

In general, it was demonstrated that experimental and computational methods, which were introduced for the interlaminar failure of fibre reinforced polymers, may be adapted to describe the interlaminar failure initiation of C/C-SiC.

The translaminar failure of C/C-SiC, however, required fracture mechanical models in contrast to CFRPs, which are usually described by stress or strain failure criterions.

Finally, the behaviour of C/C-SiC with real manufacturing defects, i.e. delaminations, was modelled by geometrically reduced 2D-FE-models with CZEs.

It was shown that the mechanical behaviour with true manufacturing defects can be predicted by FEM, if the exact defect geometries from micro-CT-data and the presented models for standard material and artificially pre-cracked material are used. That means: the surrounding material properties are not altered due to the formation of processing defects. That is why the manufacturing defects can be computed as ideal pre-cracks within standard material.

The presented work has identified a principle modus operandi going from non-destructive and fracture mechanical testing to the prediction of the mechanical behaviour of C/C-SiC with delaminations. Since the complete modelling approach presented here was using the commercial code ANSYS, it may easily be adapted for the computation of C/C-SiC structures.

In the future work, it has to be investigated if the bending-tensile strength ratio can be modelled for other CMC materials in the same way as presented here. It is assumed

that the presented approach is useful for other matrix dominated CMC materials, see Figure 90. The bending test is a favourable method to characterize the failure mechanisms and to decide which failure models may be applied: fracture mechanical modelling is recommended for matrix dominated CMCs like C/C-SiC, showing a distinct load drop at bending failure load. If the material is showing single ply failure and a stepwise decrease in load, like fibre-dominated CFRPs, fracture mechanical modelling is not appropriate.

Furthermore, the translaminar fracture mechanical modelling has to be evaluated for the design of C/C-SiC components, since it will allow a much better recovery of the material than by ordinary strength criteria. The design of a standard bending beam with linear elastic properties and a standard CFRP strength failure criterion would lead to an underestimation of the load carrying capacity by a factor of 1.7. This corresponds to the bending-tensile strength ratio in 0/90° direction. Using the non-linear modelling and the fracture mechanical failure criterion, presented here, the ultimate load could be predicted with an deviation of less than 10%.

Additionally, the modelling of interlaminar failure has to be extended for mixed mode I and II load cases and varying fibre orientations in order to apply the presented approach for the design of C/C-SiC components with interlaminar manufacturing defects.

Up to now, it was demonstrated that the presented modelling approach is capable to distinguish between critical and non-critical interlaminar defects in C/C-SiC bending samples. In the future, the same approach can be applied for CMC structures in order to reduce rejection rates and oversizing of CMC components. In this way the application of CMC-components in new industrial fields might be enhanced.

Literature

[1] B. Heidenreich, Manufacturing of CMC by Liquid Silicon Infiltration (LSI), Wiley-VCH, Ed. Krenkel, Ceramic Composite Materials, (2002), ISBN 3-527-30529-7, pp. 48- 75.

[2] W. Krenkel, H. Hald, Liquid infiltrated C/SiC—an alternative material for hot space structures, Spacecraft Structures and Mechanical Testing, European Space Agency Publications Division, ESASP-289, 325 (1989).

[3] W. Krenkel, Development of a cost-efficient process for the manufacturing of CMC-structures, PhD-Thesis, Uni. Stuttgart, (2000).

[4] W. Krenkel, Fabig, J. Tailoring of microstructure in C/C-SiC composites, Proceedings of ICCM-10, (1995), pp. 601-609.

[5] W. Krenkel, F. Berndt, C/C-SiC composites for space applications and advanced friction systems, Materials Science and Engineering A, 412 (2005), pp. 177 – 181.

[6] W. Krenkel, W. Kriven, H. Lin, Microstructure tailoring of C/C-SiC composites, 27th Annual Cocoa Beach Conference on Advanced Ceramics and Composites: B: Ceramic Engineering and Science Proceedings, 24 (2003).

[7] M. Frieß, C. Zuber, S. Hofmann, M. Crippa, B. Heidenreich, CMC-Bauteile für Heißgasanwendungen: Von der Entwicklung des Prototypen bis hin zum Serienbauteil, (2008), Wiley-VCH. ISBN 978-3-527-32615-0.

[8] D. Koch, K. Tushtev, J. Horvath, R. Knoche, G. Grathwohl, Evaluation of mechanical properties and comprehensive modeling of CMC with stiff and weak matrices, Advances in Science and Technology, 45(2006), pp. 1435-1443.

[9] K. Tushtev, J. Horvath, D. Koch, G. Grathwohl, Deformation and failure modeling of fiber reinforced ceramics with porous matrix, Advanced Engineering Materials, 6 (2004), pp. 664-669.

[10] D. Koch, K.Tushtev, G. Grathwohl, Ceramic fiber composites: Experimental analysis and modeling of mechanical properties, Composites Science and Technology, 68 (2008), pp. 1165 – 1172. Figures 2 and 3 were reprinted with permission from Elsevier.

[11] N. He, J. Hutchinson, Crack deflection at an interface between dissimilar elastic materials, International Journal of Solids and Structures, 25 (1989), pp. 1053-1067.

[12] J. Lamon, A micromechanics-based approach to the mechanical behaviour of brittle –matrix composites Comp. Science and tech., 61 (2001), pp. 2259-2272.

[13] N. Weigel, D. Dinkler, B. Kröplin, Micromechanically based continuum damage mechanics material laws for fiber-reinforced ceramics, Computers and Structures, 79 (2001), pp. 2277-2286.

[14] A. Fink, Ein Grenzflächenmodell zur Beschreibung des mechanischen Verhaltens faserverstärkter Keramik, Ph.D. Thesis, Uni. Stuttgart, (1995).

[15] M. Prewo, A compliant, high failure strain, fibre-reinforced glass-matrix composite, J. Mat. Sci., 17 (1982), pp. 3549-3563.

[16] B. Marshall and A. G. Evans, Failure mechanisms in ceramic-fiber/ceramic-matrix composites, J. Am. Ceram. Soc., 68 (5) (1985), pp. 225-231.

[17] M. Prewo, Tension and flexural strength of silicon carbide fibre-reinforced glass ceramics, J. Mater. Sci., 21 (1986), pp. 3590-3600.

[18] M. Prewo, Carbon fibre reinforced glass matrix composite tension and flexure properties, J. Mater. Sci., 23 (1988), pp. 2745-2752.

[19] F. Hild, J.-M. Domergue, F. A. Leckie, A.G. Evans, Tensile and flexural ultimate strength of fibre reinforced ceramic-matrix composites, Int. J. Solids Structures, 31 (7) (1994), pp. 1035-1045.

[20] P. S. Steif, A.Trojnacki, Bend strength versus tensile strength of fiber-reinforced ceramics, J. Am. Cer. Soc., 77 (1) (1994), pp. 221-229

[21] V. Laws, M. A. Ali, The tensile stress/strain curve of brittle matrices reinforced with glass fibre, Proc. Fibre Reinforced Materials: Design and Engineering Applications, U.K., (1977), pp. 115-123.

[22] S. Hofmann, B. Öztürk, D. Koch, H. Voggenreiter, Experimental and numerical evaluation of bending and tensile behaviour of carbon-fibre reinforced SiC, Composites: Part A, 43 (2012), pp. 1877-1885 (Respective figures were reprinted with kind permission by Elsevier).

[23] M. Kuntz, Risswiderstand keramischer Faserverbundwerkstoffe, Ph.D. Thesis, Uni. Karlsruhe, Shaker Verlag (1996).

[24] A. Krombholz, A. Goldstein, Bestimmung der kritischen Energie-freisetzungsrate an C/SiC-Laminaten unter Mixed-Mode-Belastung, http://www.dgm.de/download/tg/706/706_83.pdf

[25] R. Rikards, Interlaminar fracture behaviour of laminated composites. Computers and Structures, 76 (2000), pp. 11-18.

[26] HA. Richard, K. Benitz, A loading device for the creation of mixed mode in fracture mechanics, Int. Journ. of Fracture, 22 (1983), pp. 55-58

[27] S. Schmidt, S. Beyer, H. Knabe, Advanced ceramic-matrix composite materials for current and future propulsion technology applications, Acta Astronautica, 55, (2004), pp. 409-420.

[28] S. Schmidt, Moderne Zerstörungsfreie Bauteilprüfung durch Neutronen- und Röntgenstrahlen an keramischen Faserverbundwerkstoffen im Bereich Raumfahrtantriebe, VDI-Expertenforum: moderne Schadensanalyse – mit Neutronenstrahlen, Mai 2008.

[29] T. Ullmann, R. Jemmali, S. Hofmann, T. Reimer, C. Zuber, K. Stubicar, H. Weihs, Hendrik, Computed Tomography for non-destructive inspection of hot structures and TPS Components. 6th European Workshop on Thermal Protection Systems and Hot Structures, April 2009, Stuttgart, Germany.

[30] A. Abdul-Aziz, L.J. Ghosn, G. Baaklini, R.Bhatt, A combined NDT/Finite Element technique to study the effects of matrix porosity on the behavior of Ceramic-Matrix Composites, Materials Evaluation, 61 (11) (2003), pp. 1217-1221.

[31] A. Abdul-Aziz, G.Y. Baaklini, R.T. Bhatt, Nondestructive testing of Ceramic-Matrix Composites coupled with Finite Element Analyses, Material Evaluation, 63 (2003), pp. 413-417.

[32] G. Alfano, M.A. Crisfield, Finite Element interface model for the delamination analysis of laminated composites: mechanical and computational issues, Int. J. of Num. Methods in Eng., 50 (7) (2001), pp. 1701-1736.

[33] ASTM Standard D 5528 – 94a.

[34] AITM, Airbus Standard 1.0005, Issue 2, 1994, 1-8.

[35] AITM, Airbus Standard 1.0006, Issue 2, 1994, 1-8.

[36] A. Szekrényes, Overview on the experimental investigations of the fracture toughness in composite materials, HEJ - Mechanical Engineering and Transport Section, (2002), http://heja.szif.hu/MET/MET-020507-A/.

[37] O. Allix, P. Ladeveze, A. Corigliano. Damage analysis of interlaminar fracture specimens, Composite Structures, 31 (1995), pp. 61-74.

[38] H. Tada, P.C. Paris, G. R. Irwin, The stress analysis of cracks handbook, 3rd Ed, ASME Press, 2000, pp. 58.

[39] J. Nakayama, Direct measurement of fracture energies of brittle heterogeneous materials, J. Am. Cer. Soc., 48 (11) (1994), pp. 221-229.

[40] Dubbel, Taschenbuch für den Maschinenbau, 15th Ed., W. Beitz, K.-H. Küttner, ISBN 3-540-12418-7.

[41] Ihlenburg, HAW Hamburg, Skript, IP2 Mechanik.

[42] S. W. Tsai, E. M. Wu, A general theory of strength for anisotropic materials, J. of Comp. Mat., 5 (1971), pp. 58-80.

[43] Hill, R.; The mathematical theory of plasticity, Oxford, Clarendon Press (1950).

[44] ANSYS Inc., Release 12.1. Documentation for ANSYS (2009).

[45] S. W. Tsai, Th. Massard, Composite Design, Think Composites, United air force materials laboratory (1985).

[46] C. F. Shih, D. Lee, Further developments in anisotropic plasticity, Journal of Engineering Materials and Technology, 100 (1978), pp. 294-301.

[47] S. Valliappan, P. Boonlauloh, I.K. Lee Non-linear analysis for anisotropic materials, International Journal for Numerical Methods in Engineering, 10 (3) (1976), pp. 597–606.

[48] S. Geinitz, Ermittlung des Schubmoduls von faserverstärkter Keramik, Institut für Flugzeugbau der Universität Stuttgart und am Institut für Bauweisen- und Konstruktionsforschung des DLR, Studienarbeit (2006).

[49] J. R. Rice, A path independent integral and the approximate analysis of strain concentration by notches and cracks, Journal of Applied Mechanics, 35 (1968), pp. 379-386.

[50] A. A. Griffith, The phenomena of rupture and flow in solids, Philosophical Transaction of the Royal Society, London, Series A, 221 (1921).

[51] D. Dugdale, Yielding of steel sheets containing slits, Journal of the mechanics and Physics of Solids, 8 (1960).

[52] G. I. Barenblatt, Mathematical theory of equilibrium cracks in brittle fracture, Advances in Applied Mechanics, Academic Press, 7 (1962).

[53] S. Weisenberger, Bruchmechanische Charakterisierung von C/C-SiC mit begleitender In-situ Computertomographie, Institut für Flugzeugbau der Universität Stuttgart und Institut für Bauweisen- und Konstruktionsforschung des DLR, Studienarbeit (2012).

[54] R. Wuseni, FEM-Analyse der Krafteinleitung der EXPERT-Nasenkappe, Institut für Flugzeugbau der Universität Stuttgart und Institut für Bauweisen- und Konstruktionsforschung des DLR, Studienarbeit (2010).

[55] Mimics 12.3, Reference Guide, Materialise Corp, (2009).

[56] A. Laksimi, M. L. Beneggah, G. Jing, M. Hecini, J. M. Roclandt, Mode I interlaminar fracture of symmetrical cross-ply composites, Comp. Science and Tech., 41 (1991), pp. 147-164.

[57] G. Camus, Modelling of the mechanical behavior and damage processes of fibrous ceramic-matrix composites: application to a 2-D SiC/SiC, Int J Solids Struct, 37 (2000), pp. 919–42.

[58] E. Moeller, Handbuch Konstruktionswerkstoffe, Carl Hanser Verlag, München, (2008), ISBN 978-3-446-40170-9.

[59] B. Clauß, Fibres for Ceramic-Matrix Composites, Wiley-VCH, Ed. Krenkel, Ceramic Matrix Composites, (2008), ISBN 978-3-527-31361-7, pp. 1- 19.

[60] E. Klatt, A. Frass, M. Frieß, D. Koch, H. Voggenreiter, Mechanical and microstructural characterisation of SiC- and SiBNC-fibre reinforced CMCs manufactured via PIP method before and after exposure to air, Journal of the European Ceramic Society, 32 (2012), pp. 3861–3874.